# Structural Studies of $h$-BN and Graphene Single-Layers on Transition-Metal Surfaces

---

Dissertation
zur
Erlangung der naturwissenschaftlichen Doktorwürde
(Dr. sc. nat.)
vorgelegt der
Mathematisch-naturwissenschaftlichen Fakultät
der
Universität Zürich
von

Domenico Martoccia
aus
Italien

Promotionskomitee
Prof. Dr. Bruce D. Patterson (Vorsitz)
Prof. Dr. Hugo Keller (Leitung der Dissertation)
Prof. Dr. Philip R. Willmott
Prof. Dr. Thomas Greber
Prof. Dr. Herbert Over

Zürich, 2010

The whole of science is nothing more
than a refinement of everyday thinking

*Albert Einstein (1879 – 1955)*

To my family

This document was prepared using LaTeX2$_\varepsilon$ using Philip R. Willmott's customized version of the document class file `book.cls`, named `coolhab.cls`, and a customized bibliography style created using the `custom-bib` package.

Printed in Switzerland

# Acknowledgements

Early on in this project, it became clear to me that a researcher cannot complete a Ph.D. in physics alone. Especially when working at a synchrotron, the collaboration with other groups and people is one of the key features for success. Although the list of individuals I wish to thank extends beyond the limits of this format, I would like to thank the following persons for their dedication, and support throughout my entire project.

First I thank Bruce Patterson, for having given me the opportunity to perform this Ph.D. in an institute, as excellent as PSI. A small part of his motivation for science and some of his great ideas are crystallized in this work, and formed the start of this project. I want to thank him not only for the constant scientific input during my work, but also for the way he explained to me complicated physical relationships in the simplest way.

My biggest thanks go to Philip Willmott, he has made this work a pleasure. He guided me in his friendly way through this work and always found time for answering my questions, which often led to interesting discussions. Also, he was always there, not only when we were on the way of publishing, but also when my motivation was passing through minima – he always found the right words for getting me out again. He assisted in all of my beamtimes and made even the longest night shifts interesting and humorous. I really want to thank him also for his friendship; beside being an excellent scientist he is a person of good nature.

I want to thank Thomas Greber and Thomas Brugger for their scientific input on the subject of nanomeshes. This work was only possible with their ideas of experiments, the way they pushed the collaboration between the Universität Zürich and PSI, as well as the great sample quality they provided and the carefully prepared beamtimes, I thank them also for their friendliness.

My thanks go also to Herbert Over and Hugo Keller. As part of the Promotionskomitee,

they supported me whenever their help was needed.

My deeply-felt thanks go also to Matts Björck and my co-students in the Surface Diffraction group, Roger Herger, Christian Schlepütz and Stephan Pauli. Many of the results presented in this work rely on the great expertize in python and Matts' program GenX, which he adapted specifically for this work. All of them I thank for their involvement during the beamtimes, for the lively and interesting discussions, and for their friendships.

I thank Oliver Bunk for his great help in simulations with *fit* and for having provided the basis for the understanding of diffraction patterns of nanomeshes. His calm and straightforward thinking skills impressed me.

Without the enormous assistance of all the technicians involved in this work, none of the science would have been possible. I would like to thank our in-house engineer Dominik Meister and technician Michael Lange for helping me in improving the experimental setup needed for this work. With their careful work and their technical skills they made the accurate measurements possible. I also thank Rolf Schelldorfer for the help in designing and constructing a transportable UHV-baby chamber, which was essential for the combination of complementary techniques, and Martin Köckner for his help in adapting it and make it suitable for the ESCA-lab at the Universiät Zürich.

I want to thank also Fabia Gozzo, Antonio Cervellino, Amela Groso and Marco Stampanoni, as present and past members of the Materials Science Beamline group. They always made the atmosphere within the group very pleasant.

For good data analysis, good data is needed, which was guaranteed here by combining synchrotron light with an excellent detector. I thank all the SLS machine people for providing a constant and high beam quality for all of my experiments, but the in-house detector group and DECTRIS for having provided the surface x-ray diffraction station with a detector as outstanding as the PILATUS 100k.

My very special thanks go to Catherine, the french woman I met on the train years ago. I thank her for the patience, for the encouraging words, and for her positive way of thinking, she has helped me to remain steadfast and to never bend to difficulty. There are no words for saying how grateful I am to her love, which she expresses for me every day.

Nothing of all this would have ever happened without my mother and my brother Michele. Without their encouraging words and love, without their patience and support, I would have never been able to pursue these studies. Although my Dad cannot physically share this moment with me anymore, I am sure that he is proud of what his endless love for me has led to. Thank you, Dad.

# Abstract

Nanotemplates have attracted considerable attention in recent years. They can be used to produce well-ordered surface arrays of single molecules and nanoparticles with nanometer-scale periodicity. In particular, self-organized nanotemplates are increasingly becoming the focus of investigations, due to their ease of fabrication. When hexagonal boron nitride ($h$-BN)- and graphene single-layers are grown on substrates with slightly different lattice parameters, such as Rh(111) or Ru(0001), they form commensurate superstructures. Due to the lattice mismatch and the resulting periodically varying strength of interaction with the substrate across the surface, the monolayers tend to corrugate, that is, their separation from the substrate varies across the surface in a regular way. The electronic properties of these $sp^2$-hybridized layers can be modified, depending on the substrates they are grown on and their lattice mismatch to them. In particular, graphene, which as a freestanding layer is a gapless semiconductor with a remarkably high electron mobility and a small spin-orbit-interaction, and hence an ideal material for spintronics and other technical applications, can have an energy band gap when grown on a substrate and become a semiconductor, which for technological applications is of high interest. This complex behaviour of the electronic properties is strongly correlated to the changes in the atomic structure of both the film and substrate. An exact knowledge of the atomic structure of these systems is essential to understand their electronic and physical properties.

The availability of intense 3$^{\mathrm{rd}}$ generation synchrotron sources has allowed experiments on elastic scattering and diffraction by surfaces to be realistic, despite the fact that the interaction of photons with matter is weak. Surface x-ray diffraction (SXRD) offers nowadays unique possibilities to study the structure of thin films and interfaces with picometer resolution.

When dealing with x-ray diffraction data, one is confronted with the phase problem – the

phase is lost, due to the fact that one does not measure the complex structure factors (which have an amplitude *and* phase), but the intensities, which are the absolute squares of the structure factors. To overcome this problem SXRD relies on traditional model refinement. Model refinement requires a starting model which is sufficiently close to the real structure and an appropriate parametrization of the system. Therefore complementary methods are of enormous importance. They are not only a big help for the parametrization, but also give additional physical information, which can be essential for successfully finding the solution of a surface structure.

This thesis describes structural studies using SXRD of the $sp^2$-hybridized layers $h$-BN and graphene, grown on rhodium and ruthenium. Analysis of such superstructures using SXRD is only possible by a parametrization scheme developed as part of this thesis, in conjunction with complementary methods such as scanning tunneling microscopy (STM), low-energy electron-diffraction (LEED) and ultraviolet photoelectron spectroscopy (UPS). Systematic structural studies on $h$-BN/Rh(111), $h$-BN/Ru(0001) and graphene/Ru(0001) are presented:

In $h$-BN/Rh(111) the structure is shown to be a commensurate corrugated 13-on-12 superstructure. Its commensurability up to high temperatures proves a strong bonding to the substrate. Furthermore, the topmost surface region of the substrate does not thermally expand when the temperature is raised from room temperature to about 200°C, another manifestation of strong bonding to the surface.

The $h$-BN/Ru(0001) system exhibits a commensurate 14-on-13 superstructure. This result was surprising as simple arguments based on the known thermal expansion coefficients of bulk $h$-BN and Ru would lead to expect a 13-on-12 structure. However, the particularly strong bonding of $h$-BN to Ru results in an increase in the tightly bound *hole* region of the superstructure, allowing it to assume a longer size than at first expected.

In the case of graphene/Ru(0001), a surprisingly large superstructure was found, $(25 \times 25)$ carbon atoms matching on $(23 \times 23)$ ruthenium atoms. Strong oscillations on the superstructure rods prove a corrugation of the substrate down to several monolayers. Using genetic algorithms, crystal truncation and superstructure rod intensities have been fitted after a parametrization of the problem with less than 30 parameters. A chiral surface, caused by the breaking of the surface symmetry has been observed, induced by the associated much lower elastic energy.

# Zusammenfassung

In den letzten Jahren haben *Nanotemplates* grosse Beachtung gefunden. Sie können zur Produktion einzelner, regelmässig angeordneten Molekülen und Nanopartikeln auf Oberflächen mit Nanometer-Skala Periodizität, verwendet werden. Vor allem selbstorganisierte *Nanotemplates* sind aufgrund ihrer einfachen Herstellung zunehmend in den Fokus der Untersuchungen gerückt. Wenn einzelne hexagonale Bornitrid ($h$-BN)- und Graphen-Schichten auf Übergangsmetallen mit leicht unterschiedlichen Gitterkonstanten, wie Rh(111) oder Ru(0001) gewachsen werden, bilden sie kommensurable Überstrukturen. Aufgrund der Gitterfehlanpassung und der daraus resultierenden, sich regelmässig ändernden Stärke der Wechselwirkung mit dem Substrat entlang der Oberfläche, neigen die Monolagen dazu, zu korrugieren, das heisst, ihr Abstand zum Substrat variiert in einer periodischen Art und Weise. Die elektronischen Eigenschaften dieser $sp^2$-hybridisierten Schichten können, abhängig vom Substrat auf dem sie gewachsen sind und deren Gitterfehlanpassungen modifiziert werden. Insbesondere Graphen, das als freistehende Schicht ein Halbleiter ohne Bandlücke ist, zeigt eine bemerkenswert hohe Mobilität der Elektronen und eine kleine Spin-Bahn-Kopplung. Es ist daher ein ideales Material für Spintronik und andere technische Anwendungen. Wenn es auf einem Substrat gewachsen ist, kann es eine Energie-Bandlücke aufweisen, und ein richtiger Halbleiter werden, was für elektronische Applikationen von grossem Interesse ist. Dieses komplexe Verhalten der elektronischen Eigenschaften korreliert stark mit den Änderungen in der atomaren Struktur der adsorbierten Monolage wie auch des Substrates. Deshalb ist eine genaue Kenntnis der atomaren Struktur dieser Systeme für das Verständnis ihrer elektronischen und physikalischen Eigenschaften entscheidend.

Die Verfügbarkeit von Synchrotronquellen der 3. Generation ermöglicht Versuche mit elastischer Streuung und Beugung an Oberflächen, obwohl die Wechselwirkung von Photonen mit Ma-

terie schwach ist. Oberflächenröntgenbeugung (SXRD) bietet heute einzigartige Möglichkeiten zur Untersuchung der Struktur von dünnen Schichten und Grenzflächen mit hoher räumlicher Auflösung.

Bei der Aufnahme von Röntgenbeugungsdaten ist man mit dem Phasenproblem konfrontiert – die Phase geht verloren, weil man nicht die komplexen Strukturfaktoren (die eine Amplitude *und* eine Phase besitzen), sondern aber die Intensitäten misst, sprich die Betragsquadrate der Strukturfaktoren. Um dieses Problem zu umgehen, setzt die Oberflächenröntgen- beugung auf die traditionelle Strukturverfeinerung der Modelle. Dies erfordert eine geeignete Parametrisierung des Systems und ein Startmodell, das nahe genug an der wahren Struktur ist. Daher sind komplementäre Methoden von enormer Bedeutung. Sie sind nicht nur eine grosse Hilfe bei der Modellierung, sondern geben auch zusätzliche physikalische Informationen, die für das erfolgreiche Lösen einer Oberflächenstruktur von wesentlicher Bedeutung sind.

Diese Arbeit beschreibt eine strukturelle Untersuchung der $sp^2$-hybridisierten Schichten $h$-BN und Graphen, gewachsen auf Rhodium und Ruthenium. Die Analyse solcher Strukturen mit SXRD ist nur dank einer Parametrisierung möglich, die in dieser Arbeit beschrieben ist, in Verbindung mit komplementären Methoden, wie der Rastertunnelmikroskopie (STM), der niederenergetischen Elektronenbeugung (LEED) und der Ultraviolett-Photoelektronenspektroskopie (UPS).

Strukturanalysen der Systeme $h$-BN/Rh(111), $h$-BN/Ru(0001) und Graphen/Ru(0001) werden vorgestellt: In $h$-BN/Rh(111) ist die gefundene Überstruktur eine 13-auf-12. Die Kommensurabilität bis zu hohen Temperaturen deutet auf eine starke Bindung an das Substrat hin. Dazu kommt, dass sich die oberste Schicht des Substrates thermisch nicht ausdehnt, wenn die Temperatur von Raumtemperatur auf ca. 200°C erhöht wird, ein weiteres Zeichen der starken Bindung zwischen der Monolage und dem Substrat.

Die $h$-BN/Ru(0001) Struktur weist eine wohlgeordnete 14-auf-13 Überstruktur auf. Dieses Ergebnis kam überraschend, da einfache Argumente, die auf den bekannten thermischen Ausdehnungskoeffizienten der Volumenfestkörper $h$-BN und Ruthenium basieren, zu einer 13-auf-12 Struktur führen würden. Die besonders starke Bindung von $h$-BN zu Ruthenium aber führt zu einer Vergrösserung der fest gebundenen *Loch*bereiche in der Überstruktur, so dass es zu einer grösseren Struktur führt, als zunächst erwartet.

Im Falle von Graphen/Ru(0001), wurde eine überraschend grosse Überstruktur gefunden, (25 × 25) Kohlenstoffatome passen auf (23 × 23) Rutheniumatome. Starke Oszillationen in den Überstrukturgitterstäben beweisen, dass das Substrat bis zu mehreren Monolagen tief korrugiert ist. Mit Hilfe eines auf genetischen Algorithmen basierenden Programmpakets wurde ein Modell mit weniger als 30 Parametern verfeinert, um die Intensitäten von Grundgitter- und Überstrukturgitterstäben möglichst gut wiederzugeben. Eine chirale Oberfläche, hervorgerufen durch einen Symmetriebruch wurde beobachtet. Letzterer wurde durch die damit verbundene viel niedrigere elastische Energie induziert.

# Contents

Acknowledgments iii

Abstract vii

Zusammenfassung ix

Contents xiii

List of Figures xvii

1 Introduction 1

2 Surface x-ray diffraction (SXRD) 7

- 2.1 Introduction 7
- 2.2 Theory 9
  - 2.2.1 Bulk diffraction 9
    - 2.2.1.1 Bragg's Law 9
    - 2.2.1.2 Lattice and reciprocal lattice 10
    - 2.2.1.3 The Laue condition 11
    - 2.2.1.4 The Ewald sphere construction 12
    - 2.2.1.5 The convolution theorem 13
    - 2.2.1.6 Diffraction from an ideal infinite crystal 14
    - 2.2.1.7 Structure factors 16
    - 2.2.1.8 Scattering from a crystal 16
    - 2.2.1.9 The lattice sum 17

2.2.1.10 Argand diagram . . . . . . . . . . . . . . . . . . . . . . . . . 17
2.2.1.11 Intensity and the phase problem . . . . . . . . . . . . . . . . . . 18
2.2.2 Diffraction from a surface . . . . . . . . . . . . . . . . . . . . . . . . . 19
2.2.2.1 Crystal truncation rods . . . . . . . . . . . . . . . . . . . . . . 19
2.2.2.2 Structure factor of a surface . . . . . . . . . . . . . . . . . . . . 19
2.2.2.3 Intensity . . . . . . . . . . . . . . . . . . . . . . . . . . . . . . 21
2.2.2.4 Debye-Waller factor and occupation . . . . . . . . . . . . . . . 21
2.2.2.5 Superstructure rods . . . . . . . . . . . . . . . . . . . . . . . . 22
2.3 Experimental Setup . . . . . . . . . . . . . . . . . . . . . . . . . . . . . . 22
2.3.1 The Materials Science beamline . . . . . . . . . . . . . . . . . . . . . . 22
2.3.2 The diffractometer . . . . . . . . . . . . . . . . . . . . . . . . . . . . 23
2.3.3 UHV-baby chamber . . . . . . . . . . . . . . . . . . . . . . . . . . . . 24
2.3.4 The PILATUS 100k detector . . . . . . . . . . . . . . . . . . . . . . . 26
2.4 Data recording, extraction and correction . . . . . . . . . . . . . . . . . . 27
2.4.1 Rocking scan . . . . . . . . . . . . . . . . . . . . . . . . . . . . . . . . 29
2.4.2 Stationary mode . . . . . . . . . . . . . . . . . . . . . . . . . . . . . . 29
2.4.2.1 Limitations of the stationary mode . . . . . . . . . . . . . . . . 29
2.4.3 *h*- or *k*- scan . . . . . . . . . . . . . . . . . . . . . . . . . . . . . . 30
2.4.4 Extraction and correction . . . . . . . . . . . . . . . . . . . . . . . . . 30
2.5 Fitting using Genetic Algorithms . . . . . . . . . . . . . . . . . . . . . . . 31
Bibliography . . . . . . . . . . . . . . . . . . . . . . . . . . . . . . . . . . . . 33

**3 Complementary methods** **37**
3.1 Introduction . . . . . . . . . . . . . . . . . . . . . . . . . . . . . . . . . . 37
3.2 Scanning tunneling microscopy (STM) . . . . . . . . . . . . . . . . . . . . 37
3.3 Low-energy electron-diffraction (LEED) . . . . . . . . . . . . . . . . . . . 39
3.4 Ultraviolet Photoelectron Spectroscopy (UPS) . . . . . . . . . . . . . . . . 40
Bibliography . . . . . . . . . . . . . . . . . . . . . . . . . . . . . . . . . . . . 41

**4 Nanomeshes** **43**
4.1 Introduction . . . . . . . . . . . . . . . . . . . . . . . . . . . . . . . . . . 43
4.2 hcp(0001)- and fcc(111)-surfaces . . . . . . . . . . . . . . . . . . . . . . . 44

4.3 $sp^2$-hybridization . . . 46
4.4 Moiré patterns . . . 46
4.5 Hexagonal Boron Nitride ($h$-BN) on transition metal surfaces . . . 47
4.6 Graphene on transition metal surfaces . . . 50
4.6.1 The Mermin-Wagner Theorem . . . 54
4.7 Nanomeshes investigated with LEED and SXRD . . . 54
Bibliography . . . 57

**5 Surface X-ray diffraction study of boron-nitride nanomesh in air 63**

**6 $h$-BN on Rh(111): Persistence of a 13-on-12 superstructure 69**

**7 $h$-BN on Ru(0001) nanomesh: A 14-on-13 superstructure 75**

**8 Graphene on Ru(0001): A 25×25 Supercell 81**

**9 Graphene on Ru(0001): A corrugated and chiral structure 87**

**10 Conclusions 101**

**Curriculum vitae 103**

**Publication List 105**

# List of Figures

2.1 (a) Braggs Law (b) Zoom region of Braggs Law . . . 10
2.2 The Laue conditions . . . 11
2.3 The Ewald Sphere . . . 13
2.4 (a) Convolution theorem: The crystal (b) Convolution theorem: The diffraction pattern of a crystal . . . 15
2.5 The Argand diagram . . . 18
2.6 (a) Convolution theorem: The crystal surface (b) Convolution theorem: The crystal truncation rods . . . 20
2.7 The MS-beamline . . . 23
2.8 The diffractometer . . . 25
2.9 The UHV-baby chamber . . . 26
2.10 (a) UHV-baby chamber mounted at the ESCA-lab (b) UHV-baby chamber mounted on the diffractometer . . . 27
2.11 Typical measurement setup . . . 28

3.1 Typical STM setup . . . 39

4.1 The Ru(0001)-surface . . . 45
4.2 The Rh(111)-surface . . . 45
4.3 The $sp^2$-hybridization . . . 47
4.4 (a) The $sp^2$-hybridized layer in real space (b) The $sp^2$-hybridized layer in reciprocal space . . . 48
4.5 Moiré pattern . . . 48
4.6 The stacking of $h$-BN crystals . . . 49

4.7 Density of states of the nanomesh *h*-BN/Rh(111) . . . . . . . . . . . . . . . . . . 50
4.8 The Bernal stacking of graphite . . . . . . . . . . . . . . . . . . . . . . . . . . . . 51
4.9 a) The dispersion relation of freestanding graphene b) The dispersion relation of graphene, when coupled to the substrate. . . . . . . . . . . . . . . . . . . . . . 53
4.10 Superstructure and intensity distribution in reciprocal space . . . . . . . . . . . 56

# Chapter 1

# Introduction

Parallel developments of nanomaterials and synchrotron radiation technology worldwide over the last decades have been particularly rapid. New advances in the theoretical background as well as in experimental methods are responsible for this development, which has had an impact on both, fundamental research and industrial and technological applications.

When the nanometer size range is approached, the physical properties of a material can change dramatically. The bulk properties of any material are merely the average of all the quantum forces affecting the atoms. As one scales down to ever smaller dimensions, this averaging breaks down. There are two main reasons for this: first is the increased surface-area-to-volume ratio, which means a large fraction of the atoms are at a surface, where rearrangements of electron orbitals will occur, which would otherwise be involved in boding in the bulk, thus affecting the electronic properties. Second are quantum finite size effects which occur as dimensions approach that of the Bloch waves in the material. These can begin to dominate the behaviour of matter at the nanoscale and are the reasons why nanotechnology and nanoscience are so intensely researched.

One of the most striking developments in nanoscale science analysis was realized by the invention of the scanning tunneling microscope (STM) in 1982 [1], followed by the invention of the atomic force microscope (AFM) [2]. The STM and AFM have provided revolutionary tools for the nanoscopic investigation of the morphology and structural modification of these surfaces down to atomic scales. These techniques probe the surface very locally with high resolution, but do provide little or no depth information. Low-energy electron-diffraction (LEED) is a technique, which does provide long range order information, and the strong interaction of electrons with matter imbues it with a high sensitivity to the topmost layer, but limits its the depth sensitivity to only a few monolayers. Very often the structural changes at a surface may in fact extend down to several monolayers, depending on the nature and strength of the bonds. Indeed, a surface from the perspective of a materials scientist is not merely the topmost atomic layer, but consists of all layers which deviate significantly in their structure from that of the bulk.

X-rays, in contrast to electrons, interact weakly with matter, and can therefore give depth information. But because the scattering intensity is very low, synchrotrons were the key feature in order to get surface x-ray diffraction (SXRD) becoming a powerful tool in the investigation of surface structures.

Synchrotrons provide sufficient flux and brilliance to obtain enough scattering intensity even from the very few scattering atoms associated with the surface region. The Swiss Light Source(SLS) is a $3^{\text{rd}}$ generation synchrotron source, located at the Paul Scherrer Institut (PSI). The work described in this thesis was mainly performed at the SXRD-station of the Materials Science beamline [3], which is equipped with a $(2 + 3)$ circle diffractometer and a 2-D single-photon-counting PILATUS 100k detector [4].

The $sp^2$-hybridized materials hexagonal boron nitride and graphene both form commensurate superstructures when grown on certain transition metal substrates [5, 6, 7, 8]. The size of the superstructure periodicity of the order of 3 nm makes these honeycomblike systems very interesting from a technological point of view, since they can serve as nanotemplates. In addition, freestanding graphene has attracted enormous attention since its discovery in 2004 [9], due to its remarkable electronic properties: it is a gapless semiconductor [10]. When grown on a substrate graphene can become metallic or a band gap can be opened [11], induced by the substrate. This behaviour, attributed to the structural rearrangement of the atoms on the surface is of particular importance in terms of electronic applications. Hence, structural information of these systems is of crucial importance.

This thesis presents an SXRD-study of the commensurate superstructures, $h$-BN/Rh(111), *h*-BN/Ru(0001) and graphene/Ru(0001). It is structured as follows.

In Chapter 2 a general introduction to SXRD and to the experimental setup as used for a large part of this thesis is presented. The data analysis and the algorithm used for the model refinement are described.

Chapter 3 is a very short overview of the complementary methods used for the precharacterization of the samples.

Chapter 4 gives an introduction to the physics of the $sp^2$-hybridized layers *h*-BN and graphene, including a description of their structural and electronic properties, and how they change when grown on a substrate. Some fundamental aspects of the investigation of these superstructures with SXRD are also given.

In Chapter 5 the stability of *h*-BN on Rh(111) nanomesh under ambient conditions has been demonstrated. Beside this, a confirmation of the 13-on-12 superstructure of this system is given.

Chapter 6 investigates further the *h*-BN on Rh(111) nanomesh. The 13-on-12 superstructure is proved to be commensurate. Further, the commensurability up to high temperatures and a non-linear expansion of the substrate's surface region up to 200°C demonstrates a strong bonding between substrate and film.

Chapter 7 elucidates the structure of the *h*-BN on Ru(0001) nanomesh. Although the in-plane lattice constant of ruthenium is larger than that one of rhodium, this structure forms a surprising 14-on-13 superstructure, instead of the initially expected 13-on-12 or 12-on-11. This is explained in terms of the especially high bonding strength of *h*-BN to ruthenium, which helps accommodate in-plane strain by increasing the area of the superstructure that is strongly bound and therefore has a lower chemical energy.

The focus turns to graphene on Ru(0001) in Chapter 8, where a large 25-on-23 superstructure is found. Further an initial structural study was performed which from the strong oscillations formed in the SXRD superstructure rod data demonstrates a significant corrugation of the substrate caused by strong bonding of graphene to Ru.

In Chapter 9 the graphene on Ru(0001) structure was further investigated with unsurpassed detail. After parametrization of the system, the crystal truncation rods, superstructure rods and in-plane data were fit using genetic algorithms. The structure is found to show a chiral surface.

The conclusions of the thesis are given in Chapter 10.

## Bibliography

[1] G. Binnig, H. Rohrer, C. Gerber, and E. Weibel: "Surface Studies by Scanning Tunneling Microscopy." *Phys. Rev. Lett.* **49**(1), 57–61 (1982), doi:10.1103/PhysRevLett.49.57.

[2] G. Binnig, C. F. Quate, and C. Gerber: "Atomic Force Microscope." *Phys. Rev. Lett.* **56**(9), 930–933 (1986), doi:10.1103/PhysRevLett.56.930.

[3] B. D. Patterson, R. Abela, H. Auderset, Q. Chen, F. Fauth, F. Gozzo, G. Ingold, H. Kuhne, M. Lange, D. Maden, D. Meister, P. Pattison, T. Schmidt, B. Schmitt, C. Schulze-Briese, M. Shi, M. Stampanoni, and P. R. Willmott: "The Materials Science Beamline at the Swiss Light Source: design and realization." *Nucl. Instrum. Meth. A* **540**(1), 42–67 (2005), doi:10.1016/j.nima.2004.11.018.

[4] B. Henrich, A. Bergamaschi, C. Brönnimann, R. Dinapoli, E. F. Eikenberry, I. Johnson, M. Kobas, P. Kraft, A. Mozzanica, and B. Schmitt: "PILATUS: A single photon counting pixel detector for X-ray applications." *Nucl. Instrum. Meth. A* **607**(1), 247–249 (2009), doi:10.1016/J.Nima.2009.03.200.

[5] D. Martoccia, P. R. Willmott, T. Brugger, M. Björck, S. Günther, C. M. Schlepütz, A. Cervellino, S. A. Pauli, B. D. Patterson, S. Marchini, J. Wintterlin, W. Moritz, and T. Greber: "Graphene on Ru(0001): A 25×25 Supercell." *Phys. Rev. Lett.* **101**(12), 126102 (2008), doi:10.1103/PhysRevLett.101.126102.

[6] D. Martoccia, M. Björck, C. M. Schlepütz, T. Brugger, S. A. Pauli, B. D. Patterson, T. Greber, and P. R. Willmott: "Graphene on Ru(0001): A corrugated and chiral structure." *New J. Phys.* **12**, 043028 (2010), doi:10.1088/1367-2630/12/4/043028.

[7] D. Martoccia, S. A. Pauli, T. Brugger, T. Greber, B. D. Patterson, and P. R. Willmott: "$h-$BN on Rh(111): Persistence of a commensurate 13-on-12 superstructure up to high temperatures." *Surf. Sci.* **604**(5-6), L9–L11 (2010), doi:10.1016/J.Susc.2009.12.016.

[8] D. Martoccia, M. Björck, C. M. Schlepütz, S. A. Pauli, T. Brugger, T. Greber, B. D. Patterson, and

P. R. Willmott: "*h*-BN/Ru(0001) nanomesh: A 14-on-13 superstructure with 3.5 nm periodicity." *Surf. Sci.* **604**(5-6), L16–L19 (2010), doi:10.1016/J.Susc.2010.01.003.

[9] K. S. Novoselov, A. K. Geim, S. V. Morozov, D. Jiang, Y. Zhang, S. V. Dubonos, I. V. Grigorieva, and A. A. Firsov: "Electric field effect in atomically thin carbon films." *Science* **306**(5296), 666–669 (2004), doi:10.1126/science.1102896.

[10] S. Reich, J. Maultzsch, C. Thomsen, and P. Ordejon: "Tight-binding description of graphene." *Phys. Rev. B* **66**(3), 035412 (2002), doi:10.1103/Physrevb.66.035412.

[11] S.-Y. Kwon, C. V. Cobanu, V. Petrova, V. B. Shenoy, J. Bareño, V. Gambin, I. Petrov, and S. Kodambaka: "Growth of Semiconducting Graphene on Palladium." *Nano Lett. (accepted)* (2009), doi:10.1021/nl902140j.

# Chapter 2

# Surface x-ray diffraction (SXRD)

## 2.1 Introduction

With the accidental discovery of x-rays in 1896 [1], when Röntgen found that these rays would pass through the tissue of humans leaving, bones and metals, a new area in science was opened for applications ranging from determining the internal architecture of cells and other biological structures, to solving the atomic structure of large protein structures and crystals.

In 1913 Friedrich and Knöpping laid the first foundations for crystal structure analysis and together with the theoretical calculations provided by Laue, their results were published in 1913 [2]. By using a crystal as a diffraction grating, von Laue proved that the x-rays were waves of light with very small wavelengths. He had recorded his results photographically, showing bright spots, where diffracted x-rays happened to be in phase with each other, but he also showed a large number of spots to be missing. Diffracted beams of x-rays were expected in these directions, but did not seem to occur. Von Laue suggested that the x-rays must contain only certain wavelengths to account for the missing diffracted beams. It was William Lawrence Bragg who suggested that x-rays must be made up of a continuous spectrum of all possible wavelengths, and if this was true then the missing directions of diffraction would not be due to the characteristics of the wavelength of the x-rays, but due to some property of the crystal being examined.

William Lawrence Bragg and his father William Henry Bragg published the first full structure determinations by analysis of Laue diagrams, where they determined the correct lattice upon which the structure of the crystal is built [3, 4, 5, 6]. Here they also stated the well-known Bragg's law. The x-rays would hit each plane of atoms in turn, scattering first off the surface layer, then the one below it, and so on. If the x-rays reflected off all the surfaces were in phase a very strong signal could be measured.

Throughout research institutions and industry, x-ray diffraction has become an indispensable method for materials investigation, characterization and quality control. Example areas of application include qualitative and quantitative phase analysis, crystallography, structural relaxation determination, micro-diffraction, investigation of nano-materials and the structural analysis of surfaces.

If a bulk crystal is cut, the surface atoms often "reconstruct", or shift from their bulk equilibrium positions. Therefore x-rays diffracted from the surface will may have their Bragg reflections at different angles than x-rays diffracted from the bulk. Unfortunately, the volume of the surface region is much smaller than that of the bulk crystal resulting in much weaker and broader diffraction spots, hence much more powerful x-ray sources are essential in order to look at surfaces. The most powerful sources of x-rays for research purposes are synchrotron storage rings. Synchrotrons generate tunable beams of electromagnetic radiation from the far infrared to the hard x-ray regime, with fluxes and brilliances many orders of magnitude greater than those produced by laboratory-based sources. It is thanks to synchrotrons that surface x-ray diffraction (SXRD) could develop into one of the most powerful methods today in solving surface structures.

In this chapter a short introduction to the theory of bulk diffraction will be given [7, 8], and starting from the basics of Bragg's law and the Laue conditions, the reciprocal lattice will be introduced. The diffraction intensities of an ideal crystal will be explained with the help of the convolution theorem. Then the theory of SXRD and the fundamental concept of the crystal truncation rods will be derived, again with the help of the convolution theorem. The experimental setups used throughout the whole of this thesis will round up this first chapter.

## 2.2 Theory

Initially the use of x-rays to probe surfaces was thought to be futile. This was based on the fact that x-rays have a low scattering cross-section and hence interact very weakly with matter resulting in a deep penetration into solids. This weak interaction is on the other hand a big advantage in the theoretical description of SXRD, compared to that for low-energy electron-diffraction (LEED). Since the cross-section for elastic scattering in the case of low-energy electrons is high, electrons can be diffracted elastically several times and still be measurable, this is known as the “multiple scattering effect” and is described by dynamical theory. In contrast, the interaction of photons with the electrons of an atom is weak and the probability of multiple scattering is close to zero, hence multiple scattering effects can be neglected in SXRD, that is, SXRD satisfies “the kinematical approximation”. This makes the interpretation of an SXRD pattern fairly straightforward [9, 10, 11].

### 2.2.1 Bulk diffraction

#### 2.2.1.1 Bragg’s Law

When an ideal crystal is illuminated with x-rays of a fixed wavelength, which is comparable to distances between atomic planes in a crystal, so-called Bragg-peaks are observed, whereby the x-rays interfere constructively. In order to do so, the difference of $2x$ in the travel path length of the diffracted x-rays (see Figure 2.1) must be equal to integer multiples of the wavelength. The general relationship between the wavelength of the incident x-rays, the incident angle and spacing between the crystal lattice planes is expressed by Bragg’s Law. With $d$, the spacing between two adjacent planes of atoms, $\lambda$ the wavelength, $\theta$ the angle of the incident beam to the surface, and $n$ an integer number, Bragg’s Law is expressed as

$$n\lambda = 2d\sin(\theta). \tag{2.1}$$

Solving Bragg’s Equation gives the d-spacing between the crystal lattice planes of atoms that produce the constructive interference. A given crystal has many different planes of atoms in its structure; therefore, the collection of reflections of all the planes can be used to uniquely identify the structure of an unknown crystal.

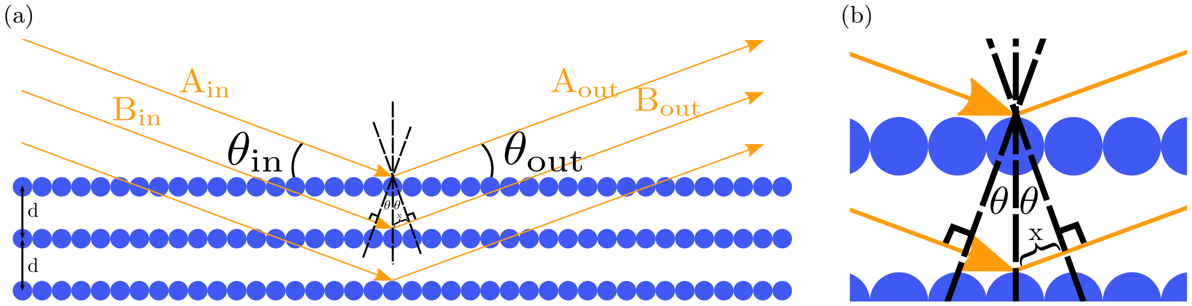

**Figure 2.1:** (a) Bragg's Law describes how an x-ray beam is reflected or diffracted in a crystal lattice. Bragg peaks are seen when the rays interfere constructively. (b) Zoom region: The difference in the path lengths between x-ray A and x-ray B is of $2x$. Bragg's law is fulfilled when the difference in the path length $2 \cdot x$ is equal to an integer multiple of the wavelength $\lambda$.

#### 2.2.1.2 Lattice and reciprocal lattice

Let **a**, **b**, **c** be the primitive vectors, hence linearly independent, of a crystal lattice. The so-called *Bravais lattice* is built up by all points **R** in real space which can be written as

$$\mathbf{R} = n_1\mathbf{a} + n_2\mathbf{b} + n_3\mathbf{c}, \qquad \text{with } n_1, n_2, n_3 \in \mathbb{Z}. \tag{2.2}$$

A *crystal* is a Bravais lattice in which associated with each lattice point is a basis which consists of physical structures such as atoms, ions and molecules.

The *reciprocal lattice* is spanned by the primitive vectors $\mathbf{a}^*$, $\mathbf{b}^*$, $\mathbf{c}^*$. One can show [12] that the reciprocal lattice is the Fourier transform of the real space lattice and that the two lattices are connected to each other via the following relations:

$$\mathbf{a}^* = 2\pi\frac{\mathbf{b}\times\mathbf{c}}{\mathbf{a}\cdot(\mathbf{b}\times\mathbf{c})} \tag{2.3}$$

$$\mathbf{b}^* = 2\pi\frac{\mathbf{c}\times\mathbf{a}}{\mathbf{a}\cdot(\mathbf{b}\times\mathbf{c})} \tag{2.4}$$

$$\mathbf{c}^* = 2\pi\frac{\mathbf{a}\times\mathbf{b}}{\mathbf{a}\cdot(\mathbf{b}\times\mathbf{c})}. \tag{2.5}$$

With these vectors any point of the reciprocal lattice can be described by

$$\mathbf{G} = h\mathbf{a}^* + k\mathbf{b}^* + l\mathbf{c}^* \qquad h, k, l \in \mathbb{Z} \tag{2.6}$$

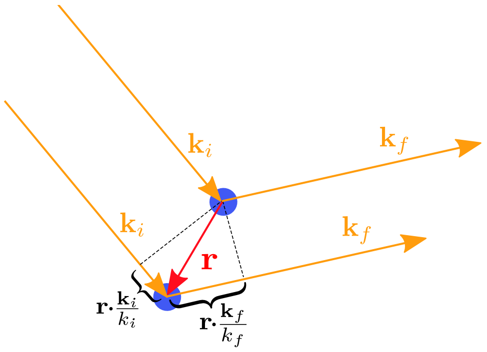

**Figure 2.2:** The Laue condition: Laue formulated an alternative theorem to Bragg's law for diffraction. This theorem is beneficial because it does not require the assumptions used by Bragg, that reflection is specular and involves parallel planes of atoms. It states that the difference between incoming and scattered wavevector must be equal to a reciprocal lattice vector.

and as a direct consequence of the definition of the reciprocal lattice vectors we state:

$$\mathbf{x}_i \cdot \mathbf{x}_j^* = \delta_{ij} \qquad \mathbf{x} \in \{\mathbf{a}, \mathbf{b}, \mathbf{c}\}. \tag{2.7}$$

#### 2.2.1.3 The Laue condition

In Figure 2.2 we see that the path length difference of the two rays diffracted from two single atoms can be expressed as

$$\Delta x = \frac{\mathbf{k}_i}{k_i} \cdot \mathbf{r} + (-\frac{\mathbf{k}_f}{k_f} \cdot \mathbf{r}), \tag{2.8}$$

where $\mathbf{r}$ is a vector connecting two lattice points in real space, $\mathbf{k}_i$ $(= 2\pi/\lambda)$ is the wavevector representing an incoming plane wave and $\mathbf{k}_f$ $(|k_f| = |k_i|)$ represents the outgoing plane wave. We will denote the difference of the two wavevectors as $\mathbf{q} = \Delta\mathbf{k} = \mathbf{k}_f - \mathbf{k}_i$. Knowing already from Bragg's law (see Section 2.2.1.1) that we only have constructive interference of two x-rays when the difference in the path length is a multiple of the wavelength, and making use of the fact that we want to detect only the elastically scattered photons, $|\mathbf{k}_i| = |\mathbf{k}_f|$, we get

$$\mathbf{r} \cdot \mathbf{q} = 2\pi \cdot n \tag{2.9}$$

Using Equation 2.7 we can directly derive the three Laue Equations:

$$\begin{aligned}\mathbf{a}\cdot\mathbf{q} &= 2\pi h \\ \mathbf{b}\cdot\mathbf{q} &= 2\pi k \\ \mathbf{c}\cdot\mathbf{q} &= 2\pi l.\end{aligned} \tag{2.10}$$

If $\mathbf{G}$ is the reciprocal lattice vector, we know from the mathematical construction of the reciprocal lattice (see Section 2.2.1.2) that $\mathbf{G}\cdot(\mathbf{a}+\mathbf{b}+\mathbf{c}) = 2\pi(h+k+l)$. The Laue equations specify $\mathbf{q}\cdot(\mathbf{a}+\mathbf{b}+\mathbf{c}) = 2\pi(h+k+l)$, hence we have

$$\mathbf{q} = \mathbf{G}. \tag{2.11}$$

In other words: the difference between incoming and scattered wavevector must be equal to a reciprocal lattice vector.

#### 2.2.1.4 The Ewald sphere construction

In 1913 Peter Ewald published details of a geometrical construction [13] interpreting the Laue conditions. When a beam hits a crystal and only elastic scattering is considered, the Ewald sphere shows which sets of planes are at their Bragg angle for diffraction to occur.

Let a crystal be depicted by its reciprocal lattice with its origin (000). We consider a plane wave with wavevector $\mathbf{k}_i$ and with wavelength $\lambda$ incident on the crystal. $\mathbf{k}_i$ starts at the center of the Ewald sphere and ends at the origin of the reciprocal lattice. The diffracted wavevector $\mathbf{k}_f$ has got the same length as the incident one, since we only consider elastic scattering. Hence all diffracted beams will sit on a sphere with length $|\mathbf{k}_i| = 2\pi/\lambda$. The difference between the wave-vectors of diffracted and incident wave is named the *scattering vector* $\mathbf{\Delta k} = \mathbf{k}_f - \mathbf{k}_i$. Since we know already that diffraction maxima can only occur when $\mathbf{\Delta k} = \mathbf{G}$ (Section 2.2.1.3), all the recordable reciprocal lattice points will be on the surface of the Ewald sphere, depicted in yellow in Figure 2.3.

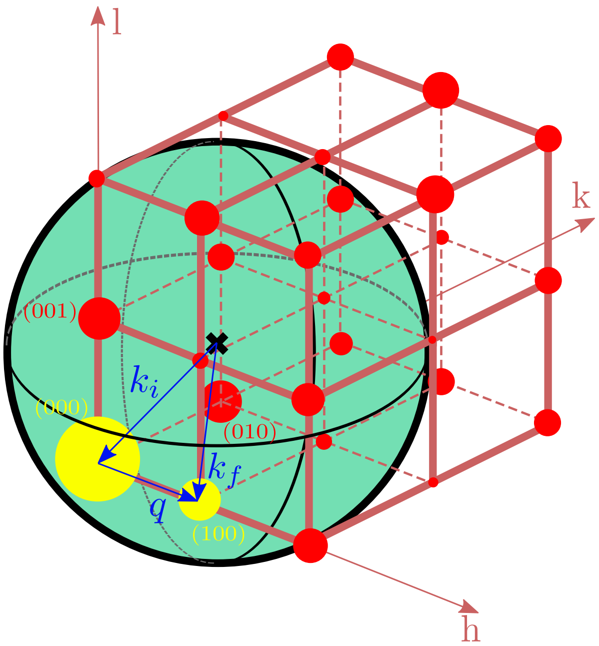

**Figure 2.3:** The Ewald Sphere represents all the points in reciprocal space where elastic scattering can occur. Its intercept with a diffraction pattern presents all the recordable reflections for a given wavelength $\lambda$ of the x-rays. The $(hkl) = (000)$ and $(100)$ reflections are highlighted in yellow, as an example of an observable diffraction pattern.

#### 2.2.1.5 The convolution theorem

The next step is to bring the basis into play. For that we will make use of the convolution theorem. Later on, some fundamental and important aspects of SXRD will be made clear also with the help of this theorem.

The *convolution* is a mathematical operation of two functions $f$ and $g$, producing a third function that is typically viewed as a modified version of one of the original functions by the second one. The convolution of $f(x)$ and $g(x)$ is written as $f \otimes g$ and is defined as

$$(f \otimes g)(x) \equiv \int_{-\infty}^{\infty} f(x') \cdot g(x - x')dx' \tag{2.12}$$

The *convolution theorem* says that “the Fourier-transform of the product of two functions, $f$ and $g$, is equal to the convolution of the Fourier transform of function $f$ and the Fourier-transform of function $g$”. This also works the other way round, namely “the Fourier-transform of the convolution of two functions, $f$ and $g$, is equal to the product of the Fourier transform of function $f$ and the Fourier-transform of function $g$"

$$\mathcal{F}(f \cdot g) = \mathcal{F}(f) \otimes \mathcal{F}(g) \tag{2.13}$$

$$\mathcal{F}(f \otimes g) = \mathcal{F}(f) \cdot \mathcal{F}(g). \tag{2.14}$$

This very important theorem will make it possible to understand how the diffraction pattern of an ideal infinite crystal and further on how the diffraction pattern of the surface of such a crystal looks like.

#### 2.2.1.6 Diffraction from an ideal infinite crystal

We have already said that the reciprocal lattice is the Fourier transform of the real space lattice (see Section 2.2.1.2) and that in the same way the scattering amplitudes in reciprocal space are the Fourier components of the real space crystal. This fact can be derived mathematically by starting from the elastic scattering of a free electron (Thomson scattering), going over to the scattering from an atom by integrating over the whole charge distribution, which is explained in detail elsewhere [14]. For the sake of simplicity we will give here a more descriptive explanation, namely using the convolution theorem (see Section 2.2.1.5)

Since a crystal is nothing more than the convolution of the Bravais lattice with the basis, due to Equation 2.14 the Fourier transform of the crystal has to be equal to the product of the Fourier transform of the Bravais lattice and the Fourier transform of the atom (see Figure 2.4). The Fourier transform of the Bravais lattice is the reciprocal lattice (a set of $\delta$-functions) (Section 2.2.1.2), whereas the Fourier transform of the electron density distribution is a continuous function which falls off with higher $q$ values in reciprocal space. Since the observable intensity is proportional to the squared structure factor, squaring the product gives a reciprocal lattice with distinct intensities on the lattice points, falling off with higher $q$-values.

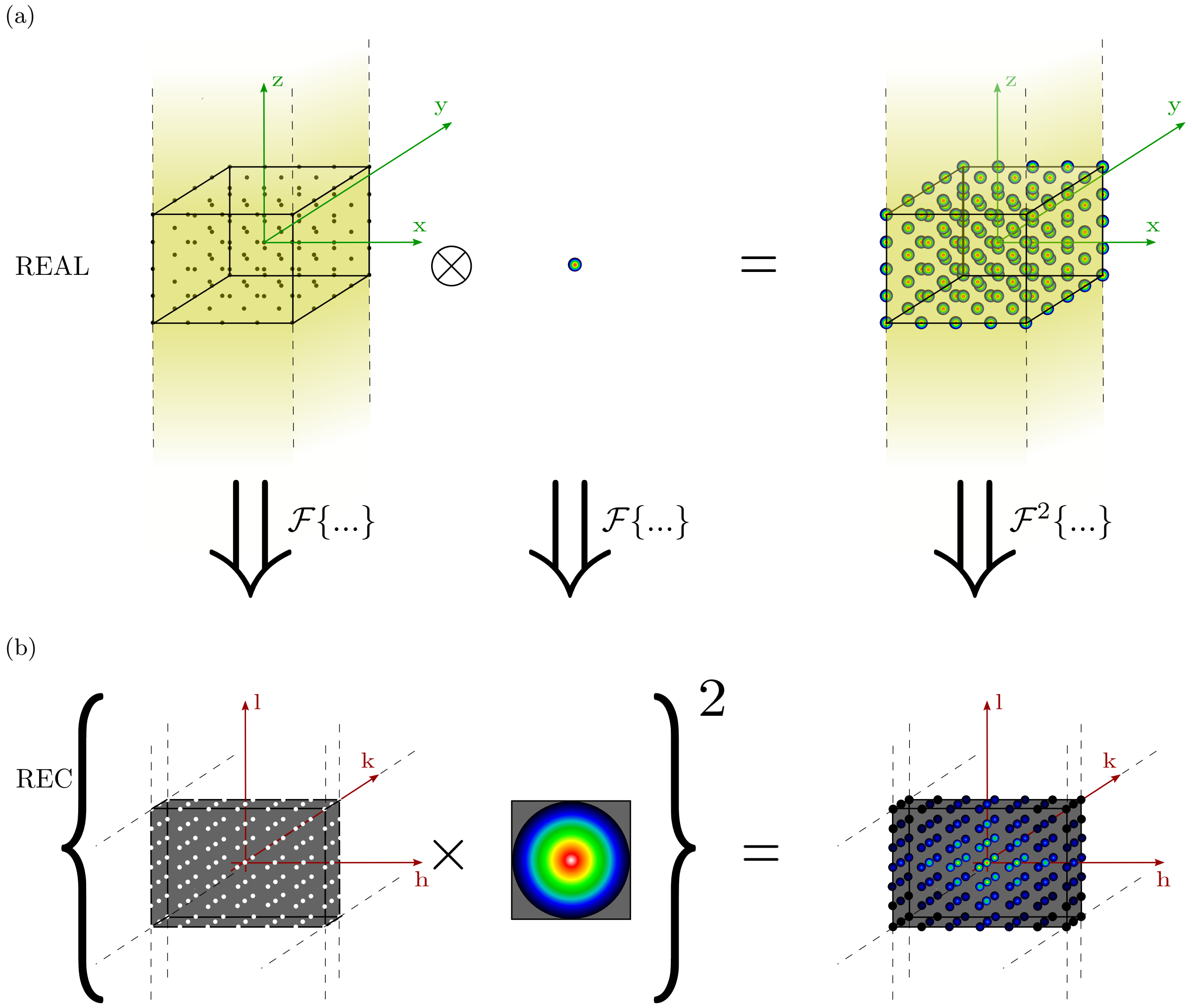

**Figure 2.4:** (a) In real space a crystal can be mathematically expressed by the convolution of two functions, one representing the Bravais lattice, say $f$, one representing the basis, say $g$. (b) The convolution theorem states that the Fourier transform $\mathcal{F}$ of $f \otimes g$ is equal to the product of $\mathcal{F}(f)$ with $\mathcal{F}(g)$. The Fourier transform of the Bravais lattice is the reciprocal lattice, which consists of a set of $\delta$-functions, whereas the Fourier transform of the basis is a continuous function which falls off with higher $q$ values in reciprocal space. The detectable quantity is the intensity.

#### 2.2.1.7 Structure factors

The Fourier transform $\mathcal{F}$ of a function $f(\mathbf{r})$ at a point $\mathbf{q}$ is defined as

$$\mathcal{F}(f(\mathbf{r}))(\mathbf{q}) \equiv \int_{-\infty}^{\infty} f(\mathbf{r}) \cdot e^{-2\pi i \mathbf{q}\mathbf{r}} d\mathbf{r}. \tag{2.15}$$

With this we can calculate the Fourier transform of the total electron density $\rho(\mathbf{r})$ in a single atom at a scattering vector $\mathbf{q}$. This quantity $f(\mathbf{q})$ is also called the *atomic form factor* and is expressed by:

$$f(\mathbf{q}) = \mathcal{F}(\rho(\mathbf{r}))(\mathbf{q}) = \int_{-\infty}^{\infty} \rho(\mathbf{r}) \cdot e^{-2\pi i \mathbf{q}\mathbf{r}} d\mathbf{r}. \tag{2.16}$$

The atomic form factors for all atoms are tabled [15] and are used whenever intensities in reciprocal space have to be calculated. Two boundary cases may be mentioned to this expression. First we note that for the case where $\mathbf{q} = 0$, $f(\mathbf{q})$ becomes $Z$, where $Z$ is the atomic number of the atom, hence $f(\mathbf{q} = 0) = Z$. Second for $\mathbf{q} \rightarrow \infty$, $e^{-2\pi i \mathbf{q}\mathbf{r}}$ oscillates with a high frequency, such that all scattering contributions cancel out on average, hence $f(\mathbf{q} \rightarrow \infty) = 0$.

For the calculation of the *structure factor* $F_{\text{uc}}(\mathbf{q})$, which is the scattering of an entire unit cell, one builds up the sum over all n atoms within this unit cell

$$F_{\text{uc}}(\mathbf{q}) = \sum_{j=1}^{n} f_j(\mathbf{q}) \cdot e^{-2\pi i \mathbf{q}\mathbf{r}_j}, \tag{2.17}$$

where $f_j(\mathbf{q})$ are the atomic form factors or the Fourier transform of the electron density of the single atoms (see Equation 2.15 and Equation 2.16) and $\mathbf{r}_j$ is the position of the atom within the unit cell.

#### 2.2.1.8 Scattering from a crystal

To calculate what the structure factor of an entire crystal looks like, one just has to add up all the structure factors of the entire crystal, taking into consideration the phase difference between the scattered waves originating from two different lattice points. The position of an atom is now given by $\mathbf{r}_j + \mathbf{R}_k$ and by summing up over all structure factors one gets:

$$F_{\text{crystal}}(\mathbf{q}) = \sum_{k=1}^{m} \sum_{j=1}^{n} f_j(\mathbf{q}) \cdot e^{-2\pi i \mathbf{q}(\mathbf{r}_j + \mathbf{R}_k)} = \overbrace{\sum_{j=1}^{n} f_j(\mathbf{q}) \cdot e^{-2\pi i \mathbf{q}\mathbf{r}_j}}^{F_{\text{uc}}(\mathbf{q})} \cdot \overbrace{\sum_{k=1}^{m} e^{-2\pi i \mathbf{q}\mathbf{R}_k}}^{\text{lattice sum}}. \tag{2.18}$$

The first sum here is the structure factor $F_{\mathrm{uc}}$ (see Equation 2.17) and we will call the second term the *lattice sum*, which is independent of the type of atoms involved, and only depends on how the atoms are arranged within the lattice.

#### 2.2.1.9 The lattice sum

In Section 2.2.1.8 we have seen that the total scattering factor from a crystal can be written as the product of the structure factor and the lattice sum. We focus here on the latter and calculate the lattice sum for a crystal containing $n_1 \times n_2 \times n_3$ atoms:.

$$\begin{aligned} S(\mathbf{q}) &= \sum_{k=1}^{m} e^{-2\pi i \mathbf{q}\mathbf{R}_k} = \sum_{n_1,n_2,n_3} e^{-2\pi i (h\mathbf{a}^*+k\mathbf{b}^*+l\mathbf{c}^*)\cdot(n_1\mathbf{a}+n_2\mathbf{b}+n_3\mathbf{c})} \\ &= \sum_{n_1} e^{-2\pi i h n_1} \cdot \sum_{n_2} e^{-2\pi i k n_2} \cdot \sum_{n_3} e^{-2\pi i l n_3}. \end{aligned} \tag{2.19}$$

For the summation over $n_1, n_2, n_3$, from 0 to $N_1-1, N_2-1, N_3-1$ each of the sums corresponds to a geometrical series, which can be calculated:

$$S_{n_1}(h) = \sum_{n_1=0}^{N_1-1} e^{-2\pi i h n_1} = \frac{1-e^{-2\pi i h N_1}}{1-e^{-2\pi i h}} = \frac{\sin(\pi N_1 h)}{\sin(\pi h)} \cdot e^{\pi i (N_1-1)h} \tag{2.20}$$

$$S_{n_2}(k) = \sum_{n_2=0}^{N_2-1} e^{-2\pi i k n_2} = \frac{1-e^{-2\pi i k N_2}}{1-e^{-2\pi i k}} = \frac{\sin(\pi N_2 k)}{\sin(\pi k)} \cdot e^{\pi i (N_2-1)k} \tag{2.21}$$

$$S_{n_3}(l) = \sum_{n_3=0}^{N_3-1} e^{-2\pi i l n_3} = \frac{1-e^{-2\pi i l N_3}}{1-e^{-2\pi i l}} = \frac{\sin(\pi N_3 l)}{\sin(\pi l)} \cdot e^{\pi i (N_3-1)l} \tag{2.22}$$

#### 2.2.1.10 Argand diagram

Apart from the interpretation of the squared structure factor, the structure factor itself has also a geometrical interpretation. As we have seen (see Equation 2.17), the structure factor is a complex number which can be represented by a vector in the complex plane. Scattering from individual atoms within the unit cell is represented hence by such a vector, and therefore the sum over all the complex atomic form factors in a unit cell is equivalent to the sum over all the corresponding vectors in the complex plane. This is represented in the *Argand diagram* (see Figure 2.5). If the positions of atoms in the unit cell are such that for a particular set of

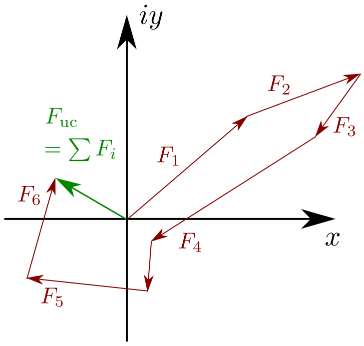

**Figure 2.5:** The Argand diagram is the graphical representation of the structure factor, it can be used to explain the extinction of some reflexes in reciprocal space. The complex structure factors are represented as complex number in the complex plane as vectors. The total structure factor can be calculated by adding up all the structure factors, hence building the sum over all vectors. If the resulting vector is 0 the structure factors cancel out each other and the reflex is extincted.

planes $(hkl)$ the total sum of complex vectors is zero, there will be no diffracted beam for that particular set of planes, even when the Bragg condition is satisfied. This explains the absence of some reflexes in the diffraction patterns.

#### 2.2.1.11 Intensity and the phase problem

As mentioned already the detectable quantity is the intensity and not the structure factor itself. The intensity is proportional to the squared structure factor

$$\begin{aligned} I_{\text{crystal}}(\mathbf{q}) &\propto |F_{\text{crystal}}(\mathbf{q}) \cdot F^*_{\text{crystal}}(\mathbf{q})|^2 \propto |F_{\text{crystal}}(\mathbf{q})|^2 \propto |S_{n_1}(h) \cdot S_{n_2}(k) \cdot S_{n_3}(l)|^2 \\ &= \left(\frac{\sin(\pi N_1 h)}{\sin(\pi h)}\right)^2 \cdot \left(\frac{\sin(\pi N_2 k)}{\sin(\pi k)}\right)^2 \cdot \left(\frac{\sin(\pi N_3 l)}{\sin(\pi l)}\right)^2 , \end{aligned} \tag{2.23}$$

where $F^*_{\text{crystal}}(\mathbf{q})$ is the complex conjugation of $F_{\text{crystal}}(\mathbf{q})$. Here we also directly see the problem arising when we measure integrated intensities in an experiment. What we would like to measure is the complex structure factors $F_{\text{uc}}(\mathbf{q})$, but there is no way of doing this. Instead we measure the intensities, which is the square of the structure factors, but by squaring the structure factor we lose the phase information. This is known as the *phase problem*.

## 2.2.2 Diffraction from a surface

### 2.2.2.1 Crystal truncation rods

We introduce now the concept of a crystal truncation rod (CTR), first detailed by I. K. Robinson in 1986 [9], where we will again make use of the mathematical description of the convolution theorem (see Section 2.2.1.5).

One can consider a crystalline surface an infinitely extended crystal which is truncated by an ideal 2-dimensional plane (see Figure 2.6(a)). Mathematically this is expressed by the product of two functions, one standing for the crystal, say $f$, one representing the truncating plane, $g$. The Fourier transform of the product of these two functions hence is, due to the convolution theorem (Equation 2.14), equal to the convolution of the Fourier transform of $f$ and the Fourier-transform of $g$ (see Figure 2.6(b)). The Fourier transform of $g$ is proportional to $1/q_z$ if the surface normal is pointing in z-direction. So, the presence of a surface in real space will smear out the $\delta$-functions in the direction of the surface normal. The result is to add a $1/q_z^2$ intensity tail to each bulk peak along the direction of the surface normal, which, in our coordinate frame, is the direction spanned by the index $L$. The bulk Bragg peaks will be aligned in linear arrays and these tails join them together to form continuous ridges of diffraction, the so-called Crystal Truncation Rods (CTR), extending all the way through reciprocal space, as illustrated in Figure 2.6(b).

### 2.2.2.2 Structure factor of a surface

We have seen in Section 2.2.1.8 what the structure factor of an infinite crystal is. Using the same approach we now want to derive what the structure factor of a surface looks like. Starting from Equation 2.18 we know that the structure factor for an infinitely extended crystal is the product of the unit cell structure factor $F_{\mathrm{uc}}(\mathbf{q})$ times the lattice sum. Here we want to calculate the structure factor along the CTR, hence we only have to consider the direction perpendicular to the surface, $z$, since the lattice sums of the in-plane directions are not influenced by the introduction of a surface.

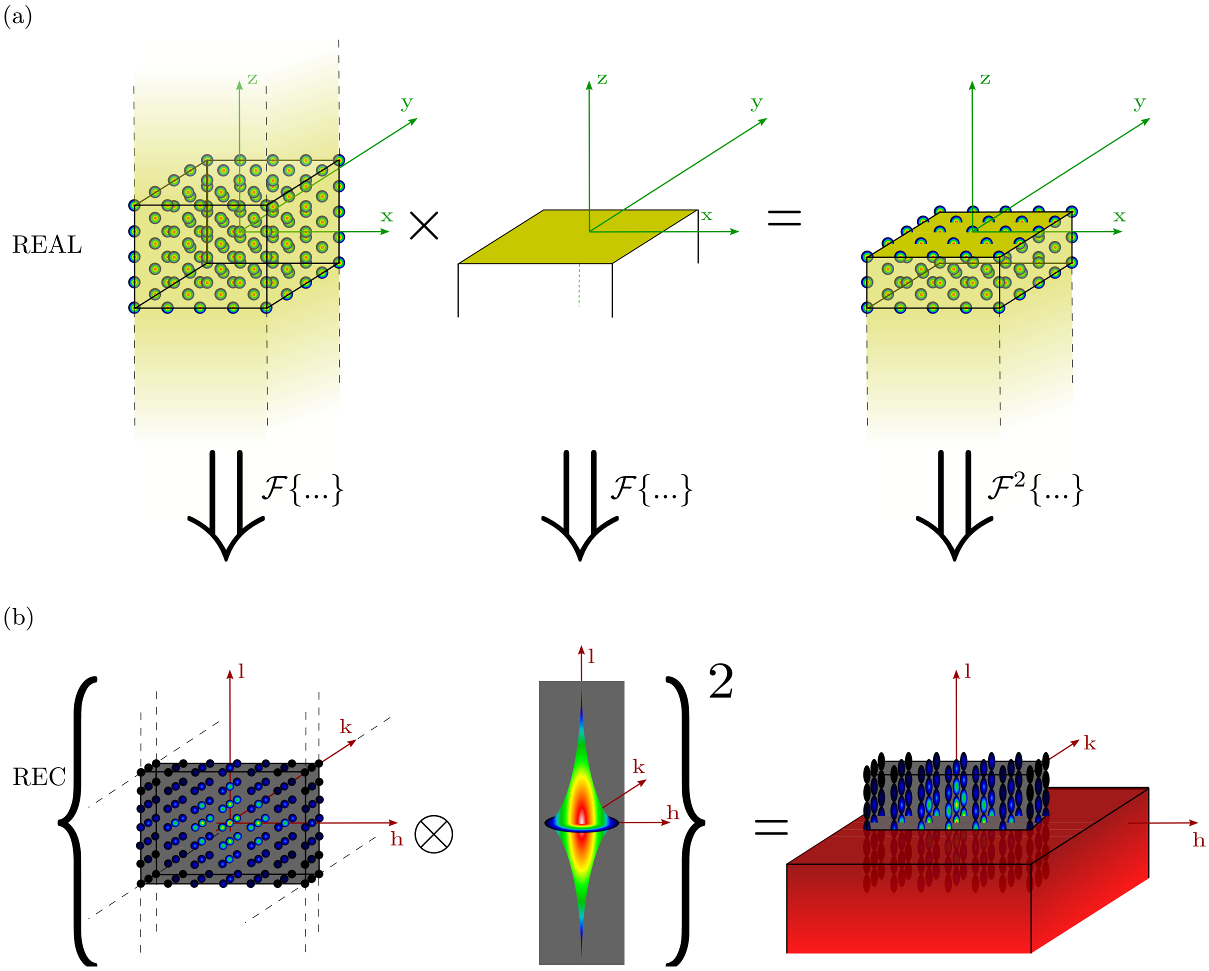

**Figure 2.6:** (a) A crystal surface can be represented by the product of a function, say $f$, representing the crystal and a function representing the surface, say $g$. (b) Due to the convolution theorem the Fourier transform the crystal surface is the product of the Fourier transform of the crystal convoluted with the Fourier transform of the surface. This gives rise to the CTRs.

The lattice sum as introduced in Section 2.2.1.9 turns then into

$$S_{\mathrm{CTR}}(l) = \sum_{k=0}^{\infty} e^{-2\pi i l n_3} = \frac{1}{1-e^{-2\pi i l}}. \tag{2.24}$$

#### 2.2.2.3 Intensity

The measurable intensity is proportional to the squared structure factor, so by using Equation 2.18 we obtain

$$I_{\text{surface}}(\mathbf{q}) \propto |F_{\text{surface}}(\mathbf{q})|^2 \propto |S_{n_1}(h) \cdot S_{n_2}(k) \cdot S_{n_3}(l)|^2 \tag{2.25}$$

$$= \frac{\sin(\pi N_1 h)}{\sin(\pi h)} \cdot \frac{\sin(\pi N_2 k)}{\sin(\pi k)} \cdot \frac{1}{4\pi \sin^2(\pi l)} \tag{2.26}$$

Here again as in Section 2.2.1.11 by squaring the structure factor we lose the phase information. In recent years several phase retrieval methods for SXRD have been proposed [16, 17, 18, 19]. They have been proven to work for relatively simple systems [20, 21, 22] but they are still in a developing stage. For the more complicated systems such as structures including reconstructions, fitting methods are indispensable.

#### 2.2.2.4 Debye-Waller factor and occupation

In general there are two more factors which will change the structure factor $F_{\text{uc}}(\mathbf{q})$ and so influence the intensity of a CTR. First the so called *Debye-Waller Factor* (DWF), is used to describe the attenuation of x-ray scattering by thermal motion of the atoms. It is defined as

$$D_j \equiv e^{-\frac{1}{2}\mathbf{q}^t \frac{\mathbf{B}_j}{8\pi^2}\mathbf{q}} \tag{2.27}$$

where $\mathbf{B}_j/(8\pi^2)$ is a $(3\times3)$ symmetric matrix, called the *Dispersion Matrix.* In a simplified case where we assume the DWF to be isotropic we can define the root mean-square-displacement of an atom $j$ as

$$\sigma_j = \sqrt{\frac{B_j}{8\pi^2}}. \tag{2.28}$$

The second parameter to be mentioned is the *occupation parameter*, which is used to describe partially occupied atom sites, here denoted as $\Theta_j$. It can assume values between 0 and 1. The unit cell structure factor is newly written as

$$F_{\text{uc}}(\mathbf{q}) = \Theta_j \cdot D_j \cdot \sum_{j=1}^{n} f_j(\mathbf{q}) \cdot e^{-2\pi i \mathbf{q}\mathbf{r}_j} \tag{2.29}$$

#### 2.2.2.5 Superstructure rods

Atoms at the surface of a crystal often assume a different structure than that of the bulk, this is called a *surface reconstruction*. This structural changes will alter the physical properties of the surface compared to the bulk. Surface reconstructions are also important in that they help in the understanding of surface chemistry for various materials, especially in the case where a different material is adsorbed at the surface.

In an ideal infinite crystal, the equilibrium position of each individual atom is determined by the forces acting by all the other crystal atoms, resulting in a periodic structure. If a surface is introduced to the system, these forces are different and hence they change the equilibrium positions of the atoms. It is most noticeable for the atoms in the surface region, as they now experience no inter-atomic forces from above the structure. This imbalance results in the atoms near the surface assuming positions with different spacing and symmetry from the bulk atoms, creating a different surface structure than present in the bulk material. Often the periodicity of the surface structure is bigger in the surface plane than the one of the bulk structure and hence this will be expressed in the diffraction pattern by the appearance of new CTRs, which in this case are called “superstructure rods” (SSRs), since they originate from a superstructure.

Because SSRs arise from rearrangements only in the surface region, SSRs do not have the intense Bragg peaks associated with bulk diffraction that one finds in CTRs. Instead, SSRs have intensities that remain comparable to those found at the weakest positions of CTRs, due to the relatively small number of scatterers involved.

## 2.3 Experimental Setup

### 2.3.1 The Materials Science beamline

A detailed description of the Materials Science Beamline at the SLS can be found elsewhere [23, 24].

The Materials Science Beamline at the SLS produces hard x-rays in the photon-energy range $5 - 40$ keV employing in the present setup a “minigap wiggler” as the insertion device. After

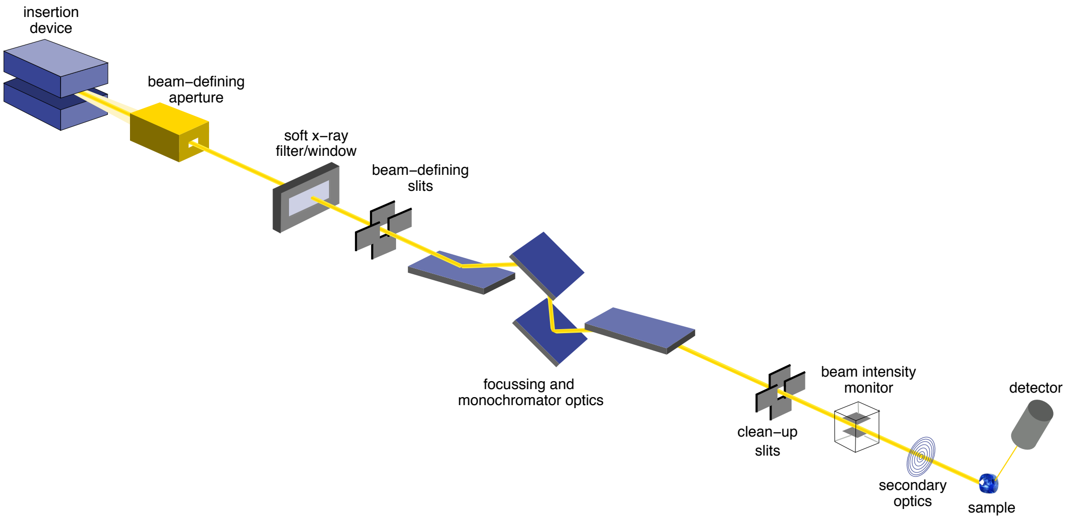

**Figure 2.7:** A typical beamline setup, as it is found also at the Materials Science beamline, SLS, PSI. When electrons pass through an insertion device, in this case an undulator or a wiggler, a strong photon source is produced. After having passed some optics elements, the monochromator selects the energy by changing the Bragg angle. The beam hits the sample and is diffracted, and the diffracted intensities are recorded with the 2D PILATUS 100k detector.

the x-ray beam has passed the beam defining apertures, it hits a rotating carbon filter, which acts as a high band pass filter for energies below 5 keV. This is important since photons in this energy range interact strongly with material and would destroy sensitive components of the beamline. Because carbon can stand high temperatures and has a good thermal conductivity, it is optimally suited for this component. After a set of beam-defining slits the beam hits the double crystal monochromator, which is enclosed by two mirrors, both needed for vertical focussing of the beam. The first crystal is responsible for the energy selection and for the horizontal focussing, whereby the second one provides a constant height of the beam entering the experimental hutch.

### 2.3.2 The diffractometer

There can be found a lot of literature regarding different types of diffractometer and angle calculations [25, 26, 27, 28, 29, 30]. Here we describe the surface diffractometer (Micro-Controle Newport, France) used for SXRD-measurements at the Materials Science beamline, Swiss Light

Source, Paul Scherrer Institut. It is a so-called $(2 + 3)$-circle diffractometer, which means 2 circles act for the sample movement and 3 circles for the detector movement. The diffractometer can be run either in vertical or in horizontal geometry. In the vertical geometry, used throughout all the present experiments, the sample circles are $\alpha$ and $\omega_v$ (see Figure 2.8), where $\alpha$ denotes the incoming angle of the x-rays with respect to the sample surface and $\omega_v$ is the rotation of the sample around its surface normal. The detector circles for horizontal and vertical geometry are the same, namely $\gamma, \delta$ and $\nu$. $\gamma$ stands for the rotation around the vertical direction which is the normal to the base plane of the diffractometer, which itself can be adjusted to be perfectly horizontal by $Y_1, Y_2$ and $Y_3$. $\delta$ describes the polar angle. $\nu$ is the rotation of the detector around its normal axis. In a horizontal geometry the sample rotations are represented by $\phi$ and $\omega_h$ (see Figure 2.8). The hexapod is based on six high-resolution actuators that control the platform and hence the sample surface with 3 translational and 3 rotational degrees of freedom. It can be mounted in horizontal and vertical geometry and the chambers can be directly fixed to it. The detailed calculations of the coordinate transformations from real to reciprocal space applied to this specific kind of diffractometer can be found in [31, 32].

### 2.3.3 UHV-baby chamber

For obtaining the structural information of well-prepared surfaces it is very important to provide and maintain a very well-defined state of the surface. For this purpose high-quality surfaces can often only be prepared using ultrahigh vacuum (UHV) techniques. Exposures of well-prepared surfaces to ambient air, containing oxygen and other reactive components will often result in a change of the surface structure. To avoid this, the goal is to prepare and measure the surface structure without having to break the vacuum. Since preparation and measurements often take place at different locations, as it was for the experiments here presented, the motivation was to design and build a transportable UHV-baby chamber specially suited for SXRD-measurements [see Figure 2.9(a)]. This approach enables one to combine not only the growth of samples with the SXRD-measurements, but also to use different surface analysis tools for pre-characterization of the surface structure, such as scanning tunneling microscopy (STM), low-energy electron-spectroscopy (LEED), x-ray photoelectron spectroscopy (XPS), ultraviolet photoelectron spectroscopy (UPS), x-ray photoelectron diffraction (XPD), which usually are

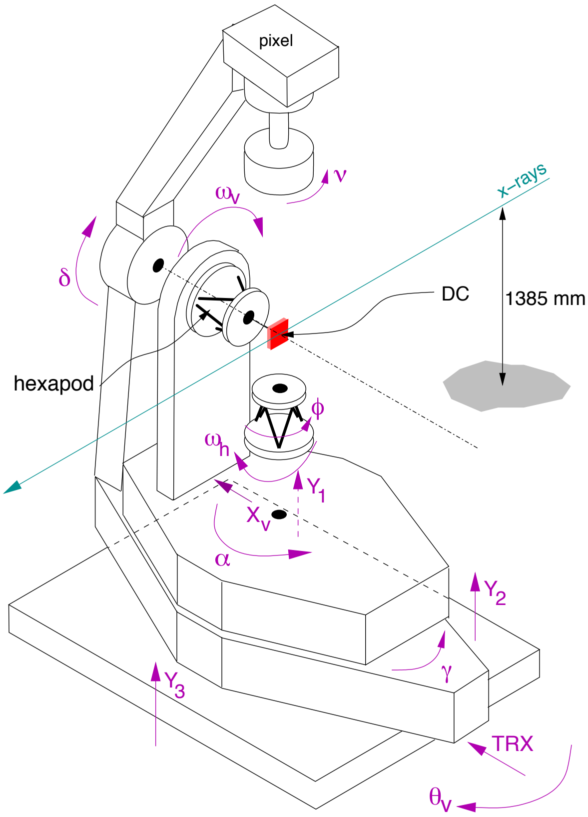

**Figure 2.8:** The diffractometer as it is found at the Surface Diffraction station of the Materials Science beamline, SLS, PSI. It is a (2 + 3)-circle diffractometer, 2 motors regard the sample movement, 3 are used for positioning the detector. It is equipped with a hexapod, which controls the alignment of the sample with micrometer-accuracy.

not provided at an SXRD-beamline. For the present work all pre-characterizations of the samples were done at the ESCA-Lab of the Physik Institut, Unviversiät Zürich, Switzerland. For the transfer the chamber is connected via a $DN40CF$ UHV flange to a tee connector attached to a docking port of the larger UHV chamber (see Figure 2.10(a)). A Varian VacIon Plus 20 pump allows one to maintain good UHV conditions (pressure of better than $2 \times 10^{-9}$ mbar). A cold cathode ion gauge tracks the pressure inside the chamber. Two 12 V batteries provide the power during transport and last (depending on the pressure) usually more than 20 hours. The whole chamber can be directly mounted to the hexapod (see Figure 2.10(b)). The hemispherical beryllium dome (Brush Wellman Inc.) acts as an x-ray window allowing for the entry of x-rays. It has an inner radius of 31.5 mm and a thickness of 0.4 mm. The sample holder

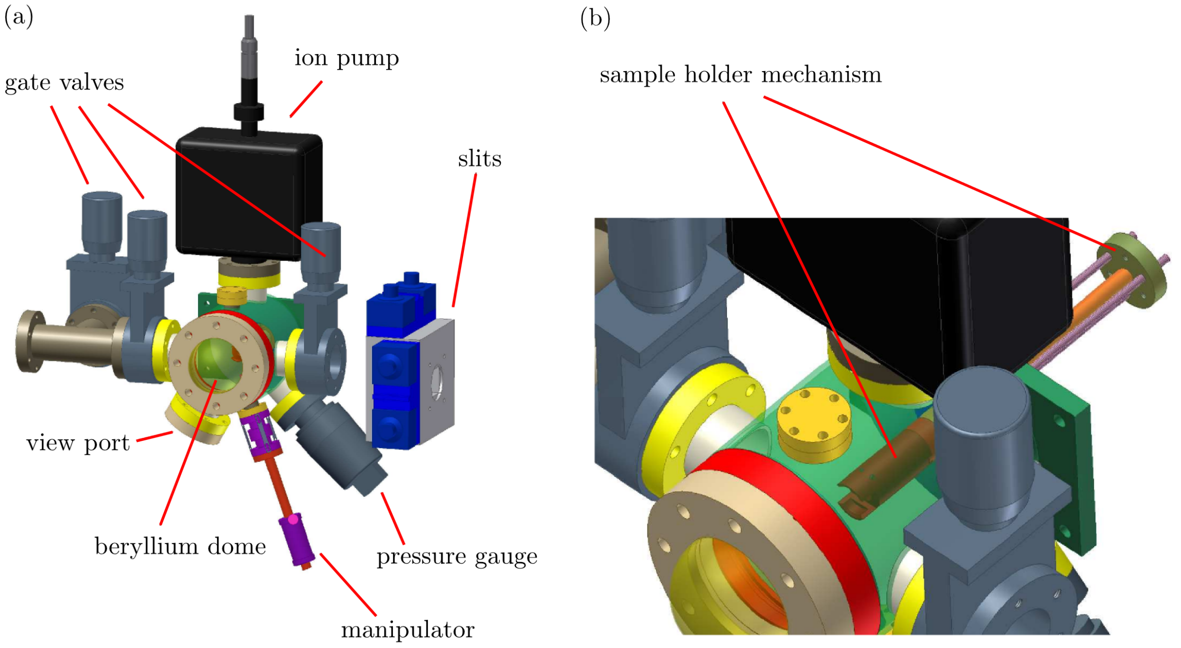

**Figure 2.9:** Schematic drawing of the UHV-baby chamber. It is equipped with an x-ray transparent beryllium dome, an ion pump assuring pressures below $2 \times 10^{-9}$ mbar, a pressure gauge, a manipulator for fixing the sample holder within the chamber and a battery supply of $2 \times 12$ V. The chamber can transfer samples via a $DN40CF$ flange. It ensures UHV-conditions during sample transport for more than 20 hours and can be directly mounted on the diffractometer at the SXRD-station of the Materials Science beamline, SLS.

mechanism can accommodate our standard sample holder (see Figure 2.9), Swiss Stubs and allows to heat the sample to temperatures of at least 900°C. A 600 mm transfer arm allows to pick up the sample at distances up to 400 mm away from the gate valve. The design of the chamber basis on [33].

### 2.3.4 The PILATUS 100k detector

In SXRD-experiments one often has to deal with weak signals originating from the topmost reconstructed layers of the investigated surface. To achieve the best possible signal quality detectors with a large dynamic range, high count-rate capability, low dark noise and fast read-out times are required. This is what the here used detector was designed and developed for.

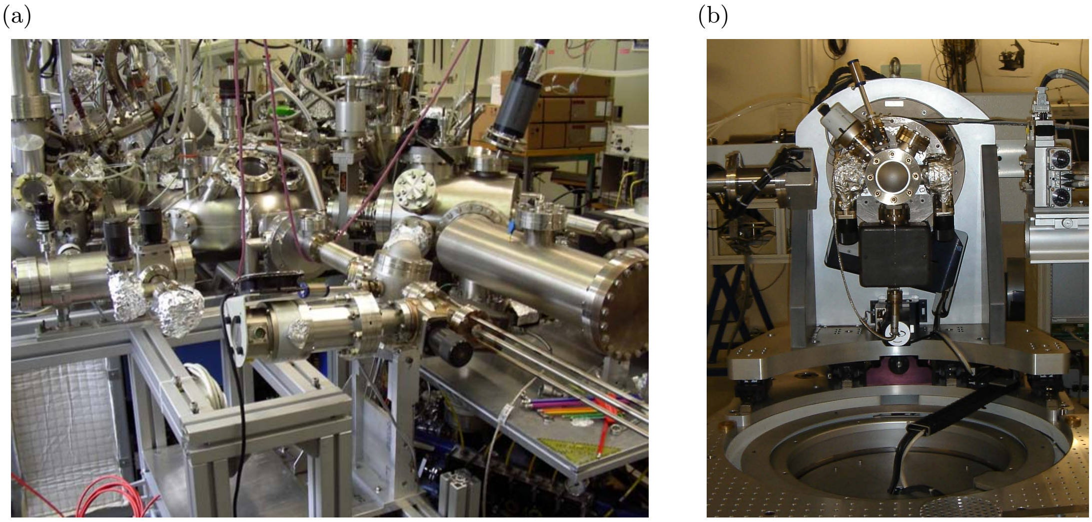

**Figure 2.10:** (a) The UHV-baby chamber mounted at the ESCA-lab at the Physik-Institut, Universität Zürich. It is attached to the load-lock via a $DN40CF$ flange and the long transfer arm transfers the sample from the main chamber to the UHV-baby chamber. (b) The UHV-baby chamber can be mounted on the diffractometer at the surface diffraction station of the Materials Science beamline, SLS, PSI. The beryllium dome ensures the transparency for x-rays.

The PILATUS 100k detector is a single photon counting pixel detector for x-ray applications. It relies on the hybrid pixel technology combining silicon sensors with complementary metal oxide semiconductor (CMOS) technology. It was developed at the Paul Scherrer Institut and was first used at the Surface Diffraction station of the Material Science beamline, SLS. It consists of $487 \times 195 = 94965$ pixels in total each with a pixel size is $(172 \times 172)$ $\mu$m [34, 35, 36]. Each pixel hence covers an angle of $(0.0086 \times 0.0086)^o$ taking into account that the distance of the detector to the center of the diffractometer is 1141 mm. The total angular acceptance of the whole detector at this distance is $(4.2 \times 1.7)^o$, which ensures that the whole signal can be captured in a single shot and gives visual feedback in discriminating signal from artifact-features.

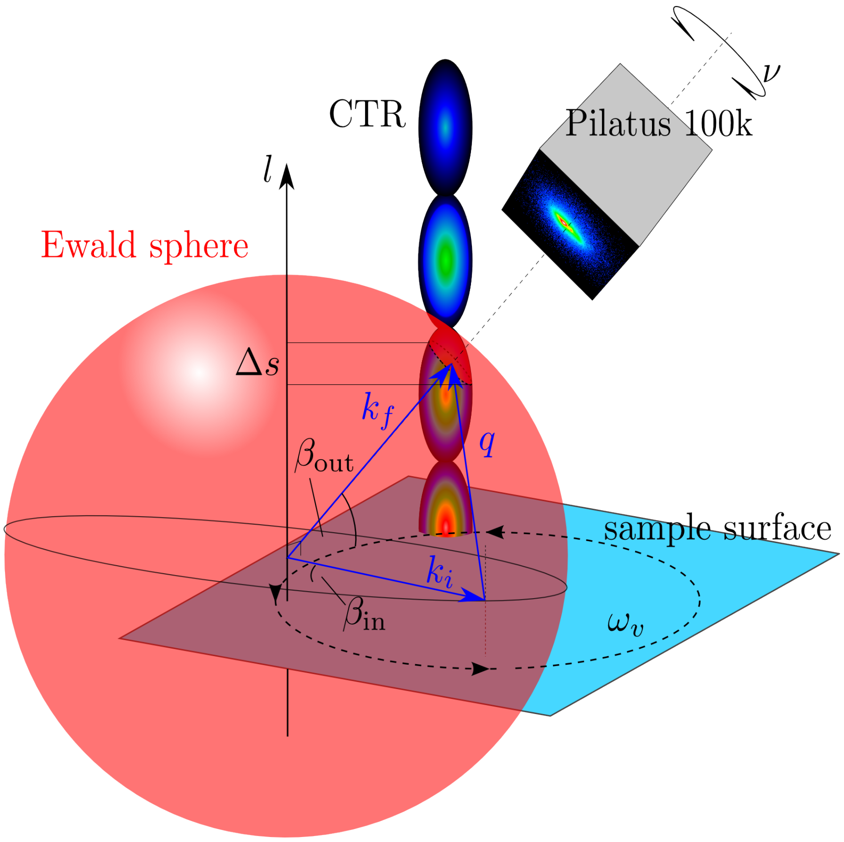

**Figure 2.11:** A typical measurement setup with a PILATUS 100k detector image taken on the (11)-CTR on graphene/Ru(0001) at $l = 1.5$. The whole signal, which is the intercept of the CTR with the Ewald sphere fits on the detector due to the large subtended angle of the detector.

## 2.4 Data recording, extraction and correction

Traditionally SXRD-data is recorded by performing so called *rocking scans* [27]. A measurement of the diffracted intensity is done by holding fixed the detector relative to the incident beam, while rotating, or “rocking” the sample. Nowadays using the new 2D-detectors there is also another way of recording data. Here one can measure the integrated intensity for one $l$-value in one single shot. In this section we will briefly describe the different modes to record data, the extraction and correction of it as they were used for the present work. A visualization of a typical measurement setup is given in Figure 2.11. The detected signal on the detector is given by the intersection of the Ewald Sphere with the CTR.

### 2.4.1 Rocking scan

In a standard SXRD-experiment the rocking scans are performed by first orienting the sample and the detector to fulfill the diffraction condition and then rotating the sample at positive and negative $\omega_v$-values around its surface normal. During the rotation of the sample, the detector positions are kept fixed. The integrated intensity at each $l$-value of a CTR is then extracted by integrating the whole rocking curve for each $l$-value, after having subtracted the background. Using a 2D-detector the advantage is that one can choose $\Delta s$, the sampled $l$-section by setting a region of interest and integrate the signal inside it for each point of the rocking scan.

### 2.4.2 Stationary mode

When using a 2D-detector, instead of taking rocking scans for each $l$-value it is possible to catch the whole integrated intensity in a single image. One orients the sample and the detector to fulfill the desired diffraction condition and takes one image representing a certain $l$-value, then one moves to the next point along the $l$-direction [27]. In principle there are two ways of performing a scan along the $l$-direction. Either one can rotate the sample around its surface normal and readjusts the detector angles to match up the Bragg condition, or one just changes the radius of the Ewald sphere by tuning the energy (this is done in LEED). Since the definition and alignment of the beam have to be redone for every energy, which would result in aligning the sample at every $l$-step, rotating the sample is much more straightforward in SXRD-measurements (see Figure 2.11).

#### 2.4.2.1 Limitations of the stationary mode

Although the stationary mode in comparison to the rocking scan mode is the much faster way of recording data, there are some limitations to it. When the Ewald sphere intercepts with the CTR (see Figure 2.11) what we see on the detector is not only one exact $l$-value, but a range of $l$-values, which we will call $\Delta s$. Now, if we integrate the picture and read out the integrated intensity, first we have to be aware that depending on where the Ewald sphere cuts the CTR this range is different. It can be seen, that

$$\Delta s \propto \frac{1}{\sin\left(\beta_{\text{out}}\right)}, \tag{2.30}$$

where $\beta_{\text{out}}$ denotes the angle between the outgoing x-ray wavevector $k_f$ and the sample surface (see Figure 2.11). It can be calculated [31] that

$$\sin\left(\beta_{\text{out}}\right) = \cos\left(\delta\right) \cdot \sin\left(\gamma - \beta_{\text{in}}\right) \tag{2.31}$$

Second as we see in Figure 2.11 we have to make sure that the sampled $l$-section is smaller than the desired resolution $\Delta l$, so $\Delta s \leq \Delta l$. This is achieved by having good crystal quality and by using the stationary mode only above a critical $\beta_{\text{out}_{\text{crit}}}$. A good sample quality with large terraces results, according to the Scherrer equation, in much thinner CTRs, and hence in a smaller sampled $\Delta s$. Another disadvantage of the stationary mode is in the case of a bad crystal quality, where scattered intensities from impurities or small crystallites inside the crystal can be found within the region of interest which one carefully selects for each image. When recording one image per $l$-value, this structure factor will be missing for the data analysis. When performing a rocking scan, the curve can still be interpolated. Mainly because of the last reason all SSRs within this work have been recorded performing the more reliable but much slower rocking scans.

### 2.4.3 $h$- or $k$- scan

In order to measure the precise size of superstructures (see Chapter 5, 8, 9, 6, 7), scans along the reciprocal directions $h$ or $k$ should be done. These scans are very similar to rocking scans, although, since we are not scanning perpendicular to the tangential of the Ewald sphere, as it is done in a rocking scan, one has to move also the detector to match up the correct diffraction conditions. This means that the correction factors will be slightly different (see Section 2.4.4).

### 2.4.4 Extraction and correction

The CTR- and SSR- data has been extracted and corrected using standard procedures, which are described elsewhere [28, 32, 37]. There is only one point which has to be mentioned: We have seen, that during an $h$- or $k$-scans one moves the detector motors $\delta$ and $\gamma$, in contrast to the classical rocking scan. This means that in contrast to a classical rocking scan, where all correction factors stay constant over one scan (in the case of a round sample), here the correction factors have to be applied to each point of the scan individually.

## 2.5 Fitting using Genetic Algorithms

Although SXRD is a powerful method for solving surface structures, it still suffers from the phase problem, as discussed in Section 2.2.1.11. One can attempt to resolve this problem either by using the so-called *direct methods* [18, 19, 38, 39, 40, 41], where iterative algorithms retrieve the phase, or by using classical model fitting. In order to use phase-retrieval algorithms one requires large datasets, ideally complete datasets, whereby all the structure factors accessible within the Ewald sphere are collected.

In comparison to “normal” XRD, where a complete dataset can be recorded fairly quickly, a complete dataset in SXRD can be much larger due to the breaking of the symmetry along the third dimension. Recording a complete dataset of a non-reconstructed surface typically requires two days. Of course this depends on the sample quality, symmetry of the sample, the detector, and diffractometer type. When the surface is reconstructed and superstructure rods arise, the time needed for recording such a dataset increases accordingly, especially if there are many superstructure rods as it is the case in the present work, recording a complete dataset becomes impossible.

Therefore the method used for solving the structure in Chapter 9 was model fitting. In model fitting the goal is to reach the global minimum of differences between the simulation and the recorded data. In the systems presented in this thesis, the number of contributing atoms is so large that one has to parametrize the structure as a single periodic deviation from an ideal flat starting structure using Fourier components.

Depending on the number of parameters involved, the “landscape” can be highly complicated. The choice of parametrization is critical in obtaining the correct final structure. This is why complementary experimental methods, such as STM, LEED and UPS are so important in this respect.

Once the parametrization has been defined, the central effort is to find the so called *global minimum* of the landscape, since this will represent the best fit and hence the structure which best reflects the experimental data. Often the number of parameters involved in this fitting procedure is large and fitting the data is time-consuming, especially in the case of large unit cells. Also here the importance of complementary methods has to be stressed, since the maximum of additional information reduces the necessary size of parameter space. But even for a modest parameter space, the global minimum is usually only found when the starting model is close to the correct solution. Classical fitting techniques include the *Downhill simplex* [42] and the *Levenberg-Marquardt* [43, 44] methods, but these are unable to escape from local minima, and both therefore require fairly good estimates for the initial guess in order to find the correct minimum. The *Monte Carlo Method* and the *Simulated Annealing* are only two of several more methods, which can be applied to find the correct minimum.

For the present work a so-called *genetic algorithm* named GenX [45] was used, which takes its name and functionality from the evolution of biological systems in nature. Every iteration is called a generation. Generation after generation, a population adapts itself to the environment by selecting the best suited individuals according to a certain criterion. The system evolves thanks to the recombination of the genes from the previous generation and random mutation in each generation. Mutations guarantee the diversity of the population, which lends the necessary randomness to the system, while gene recombination helps to concentrate the search in the most promising regions of the parameter space, as only the genes (parameters) which are closest to the experiment (these are the best suited individuals) are allowed to recombine for the next generation.

# Bibliography

[1] W. C. Röntgen: "On a New Kind of Rays." *Nature* **53**(1369), 274–276 (1896), doi:10.1038/053274b0.

[2] W. Friedrich, P. Knipping, and M. Laue: "Interferenzerscheinungen bei Röntgenstrahlen." *Ann. Phys.* **41**(10), 971–988 (1913), doi:10.1002/andp.19133461004.

[3] W. H. Bragg and W. L. Bragg: "The reflection of X-rays by crystals." *P. R. Soc. Lond. A-Conta.* **88**(605), 428–438 (1913), doi:10.1098/rspa.1913.0040.

[4] W. H. Bragg and W. L. Bragg: "The structure of the diamond." *Nature* **91**, 557–557 (1913), doi:10.1098/rspa.1913.0084.

[5] W. L. Bragg: "The structure of some crystals as indicated by their diffraction of x-rays." *P. R. Soc. Lond. A-Conta.* **89**(610), 248–277 (1913), doi:10.1098/rspa.1913.0083.

[6] W. L. Bragg: "The specular reflection of X rays." *Nature* **90**, 410–410 (1913), doi:10.1038/090410b0.

[7] J. M. Cowley: *Diffraction physics*. Elsevier Science B.V., Amsterdam, The Netherlands, third edition (1995).

[8] B. E. Warren: *X-ray diffraction*. Addison-Wesley Publishing Company, Massachusetts (1969).

[9] I. K. Robinson: "Crystal Truncation Rods and Surface-Roughness." *Phys. Rev. B* **33**(6), 3830–3836 (1986), doi:10.1103/PhysRevB.33.3830.

[10] R. Feidenhans'l: "Surface structure determination by X-ray diffraction." *Surf. Sci. Rep.* **10**(3), 105–188 (1989), doi:10.1016/0167-5729(89)90002-2.

[11] I. K. Robinson: "Surface Crystallography." In *Handbook on Synchrotron Radiation, Vol. 3*, Edited by G. Brown and D. E. Moncton, 221–266, Amsterdam, North-Holland, third edition (1991).

[12] C. Kittel: *Introduction to Solid State Physics*. John Wiley & Sons Inc., New York, fifth edition (1976).

[13] P. P. Ewald: "Zur Theorie der Interferenzen der Roïtgentstrahlen in Kristallen." *Physikalische Zeitschrift* **14**, 465–472 (1913).

[14] J. D. Jackson: *Classical Electrodynamics*. John Wiley & Sons Inc., New York, second edition (1975).

[15] E. Prince (Editor): *International Tables for Crystallography, Vol. C, Mathematical, physical and chemical tables*. International Union of Crystallography, Chester, first online edition (2006), doi: 10.1107/97809553602060000001.

[16] J. Rius, C. Miravitlles, and R. Allmann: "A Tangent Formula Derived from Patterson-Function Arguments. IV. The Solution of Difference Structures Directly from Superstructure Reflections." *Acta Crystallogr. Sect. E* **52**(4), 634 (1996), doi:10.1107/s0108767396003285.

[17] Y. Yacoby, R. Pindak, R. MacHarrie, L. Pfeiffer, L. Berman, and R. Clarke: "Direct structure determination of systems with two-dimensional periodicity." *J. Phys. Condens. Matter* **12**(17), 3929–3938 (2000), doi:10.1088/0953-8984/12/17/301.

[18] D. K. Saldin, R. J. Harder, V. L. Shneerson, and W. Moritz: "Phase retrieval methods for surface x-ray diffraction." *J. Phys. Condens. Matter* **13**(47), 10689–10707 (2001), doi:10.1088/0953-8984/13/47/311.

[19] M. Björck, C. M. Schlepütz, S. A. Pauli, D. Martoccia, R. Herger, and P. R. Willmott: "Atomic imaging of thin films with surface x-ray diffraction: introducing DCAF." *J. Phys. Condens. Matter* **20**(44), 445006 (2008), doi:10.1088/0953-8984/20/44/445006.

[20] P. R. Willmott, S. A. Pauli, R. Herger, C. M. Schlepütz, D. Martoccia, B. D. Patterson, B. Delley, R. Clarke, D. Kumah, C. Cionca, and Y. Yacoby: "Structural basis for the conducting interface between $LaAlO_3$ and $SrTiO_3$." *Phys. Rev. Lett.* **99**(15), 155502 (2007), doi: 10.1103/PhysRevLett.99.155502.

[21] R. Herger, P. R. Willmott, C. M. Schlepütz, M. Björck, S. A. Pauli, D. Martoccia, B. D. Patterson, D. Kumah, R. Clarke, Y. Yacoby, and M. Dobeli: "Structure determination of monolayer-by-monolayer grown $La_{1-x}Sr_xMnO_3$ thin films and the onset of magnetoresistance." *Phys. Rev. B* **77**(8), 085401 (2008), doi:10.1103/PhysRevB.77.085401.

[22] D. P. Kumah, S. Shusterman, Y. Paltiel, Y. Yacoby, and R. Clarke: "Atomic-scale mapping of quantum dots formed by droplet epitaxy." *Nat. Nanotechnol.* (2009), doi:10.1038/nnano.2009.271.

[23] B. D. Patterson, R. Abela, H. Auderset, Q. Chen, F. Fauth, F. Gozzo, G. Ingold, H. Kuhne, M. Lange, D. Maden, D. Meister, P. Pattison, T. Schmidt, B. Schmitt, C. Schulze-Briese, M. Shi, M. Stampanoni, and P. R. Willmott: "The Materials Science Beamline at the Swiss Light Source: design and realization." *Nucl. Instrum. Meth. A* **540**(1), 42–67 (2005), doi: 10.1016/j.nima.2004.11.018.

[24] B. D. Patterson, C. Brönnimann, D. Maden, F. Gozzo, A. Groso, B. Schmitt, M. Stampanoni, and

P. R. Willmott: “The materials science beamline at the Swiss Light Source.” *Nucl. Instrum. Meth. B* **238**(1-4), 224–228 (2005), doi:10.1016/j.nimb.2005.06.194.

[25] W. R. Busing and H. A. Levy: “Angle Calculations for 3- and 4- Circle X-Ray and Neutron Diffractometers.” *Acta Crystallogr.* **22**, 457 (1967), doi:10.1107/S0365110X67000970.

[26] K. W. Evans-Lutterodt and M. T. Tang: “Angle Calculations for a $2 + 2$ Surface X-Ray Diffractometer.” *J. Appl. Crystallogr.* **28**, 318–326 (1995), doi:10.1107/S0021889894011131.

[27] E. Vlieg: “Integrated Intensities Using a Six-Circle Surface X-ray Diffractometer.” *J. Appl. Crystallogr.* **30**(5), 532 (1997), doi:10.1107/s0021889897002537.

[28] E. Vlieg: “A (2+3)-type surface diffractometer: Mergence of the z-axis and (2+2)-type geometries.” *J. Appl. Crystallogr.* **31**, 198–203 (1998), doi:10.1107/S0021889897009990.

[29] H. You: “Angle calculations for a 4S+2D’ six-circle diffractometer.” *J. Appl. Crystallogr.* **32**, 614–623 (1999), doi:10.1107/S0021889899001223.

[30] O. Bunk and M. M. Nielsen: “Angle calculations for a z-axis/(2S+2D) hybrid diffractometer.” *J. Appl. Crystallogr.* **37**, 216–222 (2004), doi:10.1107/S0021889803029686.

[31] P. R. Willmott and C. M. Schlepütz: “Angle calculations for the 5-circle surface diffractometer of the Materials Science beamline at the Swiss Light Source.” (2007).
URL `http://sls.web.psi.ch/view.php/beamlines/ms/sd/primer/anglecalculations.pdf`

[32] C. M. Schlepütz: *Systematic Structure Investigation of YBCO Thin Films with Direct Methods and Surface X-ray Diffraction.* Ph.D. thesis, University of Zurich (2009).

[33] F. U. Renner, Y. Grunder, and J. Zegenhagen: “Portable chamber for the study of UHV prepared electrochemical interfaces by hard x-ray diffraction.” *Rev. Sci. Instrum.* **78**(3), 033903 (2007), doi:10.1063/1.2714046.

[34] B. Henrich, A. Bergamaschi, C. Brönnimann, R. Dinapoli, E. F. Eikenberry, I. Johnson, M. Kobas, P. Kraft, A. Mozzanica, and B. Schmitt: “PILATUS: A single photon counting pixel detector for X-ray applications.” *Nucl. Instrum. Meth. A* **607**(1), 247–249 (2009), doi:10.1016/J.Nima.2009.03.200.

[35] P. Kraft, A. Bergamaschi, C. Brönnimann, R. Dinapoli, E. F. Eikenberry, B. Henrich, I. Johnson, A. Mozzanica, C. M. Schlepütz, P. R. Willmott, and B. Schmitt: “Performance of single-photon-counting PILATUS detector modules.” *J. Synchrotron Radiat.* **16**, 368–375 (2009), doi:10.1107/S0909049509009911.

[36] P. Kraft, A. Bergamaschi, C. Brönnimann, R. Dinapoli, E. F. Eikenberry, H. Graafsma, B. Henrich, I. Johnson, M. Kobas, A. Mozzanica, C. A. Schlepütz, and B. Schmitt: “Characterization and Calibration of PILATUS Detectors.” *IEEE Trans. Nucl. Sci.* **56**(3), 758–764 (2009), doi: 10.1109/Tns.2008.2009448.

[37] C. M. Schlepütz, R. Herger, P. R. Willmott, B. D. Patterson, O. Bunk, C. Brönnimann, B. Henrich, G. Hulsen, and E. F. Eikenberry: “Improved data acquisition in grazing-incidence X-ray scattering experiments using a pixel detector.” *Acta Crystallogr. Sect. E* **61**, 418–425 (2005), doi: 10.1107/S0108767305014790.

[38] X. Torrelles, J. Rius, F. Boscherini, S. Heun, B. H. Mueller, S. Ferrer, J. Alvarez, and C. Miravitlles: “Application of x-ray direct methods to surface reconstructions: The solution of projected superstructures.” *Phys. Rev. B* **57**(8), 4281 (1998), doi:10.1103/physrevb.57.r4281.

[39] X. Torrelles, J. Rius, C. Miravitlles, and S. Ferrer: “Application of the direct methods difference sum function to the solution of reconstructed surfaces.” *Surf. Sci.* **423**(2-3), 338 (1999), doi:10.1016/s0039-6028(98)00928-5.

[40] Y. Yacoby, M. Sowwan, E. Stern, J. O. Cross, D. Brewe, R. Pindak, J. Pitney, E. M. Dufresne, and R. Clarke: “Direct determination of epitaxial interface structure in $Gd_2O_3$ passivation on GaAs(100).” *Nat. Mater.* **1**(2), 99–101 (2002), doi:10.1038/Nmat735.

[41] L. D. Marks, N. Erdman, and A. Subramanian: “Crystallographic direct methods for surfaces.” *J. Phys. Condens. Matter* **13**(47), 10677–10687 (2001), doi:10.1088/0953-8984/13/47/310.

[42] J. A. Nelder and R. Mead: “A Simplex-Method for Function Minimization.” *Comput. J.* **7**(4), 308–313 (1965), doi:10.1093/comjnl/7.4.308.

[43] K. Levenberg: “A Method for the Solution of Certain Non-Linear Problems in Least Squares.” *Quart. Appl. Math. 2* 164168. (1944).

[44] D. W. Marquardt: “An Algorithm for Least-Squares Estimation of Nonlinear Parameters.” *Journal of the Society for Industrial and Applied Mathematics* **11**(2), 431–441 (1963), doi:10.1137/0111030.

[45] M. Björck and G. Andersson: “GenX: an extensible X-ray reflectivity refinement program utilizing differential evolution.” *J. Appl. Crystallogr.* **40**(6), 1174–1178 (2007), doi: 10.1107/S0021889807045086.

# Chapter 3

# Complementary methods

## 3.1 Introduction

The history of surface science hails back to the beginning of the $20^{\text{th}}$ century with the discovery of the Haber process. In the intervening century many new methods have been developed. Using incident and emitted electrons, photons, atoms and ions, techniques have been developed to study the composition, structural, electronic and vibrational properties of surfaces. A key feature for the successful study of surface structures has been the exploitation and combination of several complementary methods.

In this chapter the basic principles, advantages and limitations of the complementary methods used for this thesis will be discussed. All the presented studies included precharacterization with STM, LEED and UPS before performing the SXRD-measurements.

## 3.2 Scanning tunneling microscopy (STM)

Scanning tunneling microscopy (STM) was invented in 1981 by Gerd Binnig and Heinrich Rohrer [1] at IBM Zürich Research Laboratories, in Switzerland. The technique is based on the basic principle of the tunneling effect. A piezo-electric scanner is used to accurately position an atomically sharp tip above a sample. Changing the position in the lateral $(x, y)$-plane allows one to scan continuously across the sample surface and monitoring changes in the vertical $z$-position. If this distance becomes small enough $(0.1-10)$ Å and a bias voltage is applied between the sample and the the tip, a classically forbidden potential barrier can be overcome and electrons from occupied states of the tip tunnel into unoccupied states of the sample. The tunneling current $(0.1-1)$ nA can be observed (see Figure 3.1). The tunneling current depends exponentially on the tip–sample separation. If a feedback loop is used to adjust the vertical position to keep the current constant, the *constant current scanning mode*, the tip–sample separation can be kept constant with great precision, hence the topography of the surface can be measured with great accuracy. In another mode the *constant height scanning mode*, the $z$-coordinate of the tip and the bias voltage can be held constant and the variation of the tunneling current is measured, which reflects the charge density of the surface. Since the readjustment of the sample-tip distance is not needed, the scanning frequency can be higher than in the constant current scanning mode [2, 3]. In addition to scanning across the sample, information on the electronic structure at a precise location can be obtained by changing the bias voltage while measuring the tunneling current. This results in a plot of the local density of states as a function of energy within the sample, it is called *Scanning Tunneling Spectroscopy (STS)*.

In principle, STM should only work with conducting samples and not with insulators, since the tunneling current originates from the fact that electrons from the occupied states of the tip travel through the barrier to unoccupied states of the sample. Today it is also possible to perform STM on insulators by injecting electrons into the conduction band of the insulator. The big advantage of STM is its local nature. It is suited to locally probe the surface with high resolution. The biggest limitation of STM is the inability to prepare stable, atomically-sharp tips with well-known physical and chemical properties. The unknown geometry and electronic properties of the tip are usually the largest uncertainties regarding interpretation of STM images.

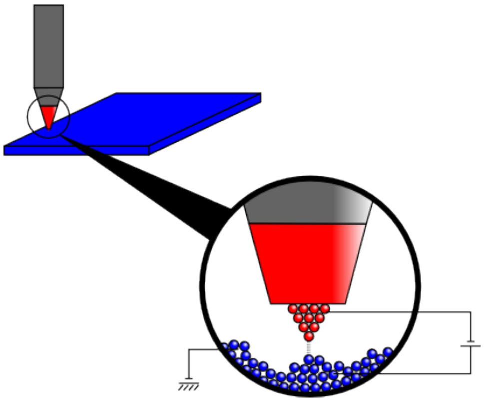

**Figure 3.1:** Schematics of a scanning tunneling microscope. A sharp tip is moved by a piezoelectric positioning system over a sample surface. By applying a voltage between tip and sample a weak tunneling current (in the nA range) flows if the tip is sufficiently close to the sample. The positioning system is made of three orthogonal piezoelectric bars. Application of suitable voltages allows movement of the tip in x-, y- and z-directions. A feedback loop keeps the local interaction constant during the scanning of the sample.

## 3.3 Low-energy electron-diffraction (LEED)

Low-energy electron-diffraction (LEED) was invented in 1927 by Davisson and Germer [4, 5] and is one of the most widely used experimental probes of surface structures. The principle is similar to that of SXRD (see Chapter 2), but instead of x-ray photons impinging onto the surface, one uses electrons with low energies (50 – 300) eV. These have wavelengths comparable to interatomic distances, and are therefore diffracted by the periodically ordered surface structure. In contrast to SXRD, where the CTRs are recorded by rotating the sample, and keeping the photon energy constant, one changes the intersection point of the Ewald sphere with the rod varying the electron energy and hence the size of the Ewald sphere. This is called LEED I/V data analysis.

At low electron energies the mean free path of the electrons in the surface is typically 1 nm, hence LEED is a very surface sensitive technique. In principle this is a good thing for investigating surfaces, but at the same time it presents the limitations of providing no information about the system below 2 or 3 atomic layers. In addition since the interaction of these low-energy electrons with the surface atoms is high, the electrons are strongly scattered, and this gives rise to the problem of multiple scattering [6]. The kinematical approximation does not hold anymore in LEED I/V analysis, hence the calculations have to be performed dynamically, which is far more computationally demanding.

## 3.4 Ultraviolet Photoelectron Spectroscopy (UPS)

The basic physical principle behind all photoemission experiments is the *photoelectric effect*. When a surface of a solid is illuminated by photons of sufficiently high energy, it will emit photoelectrons. These electrons are released from either a core level, in which case the analyzing technique is called *x-ray photoelectron spectroscopy* (XPS), or from the valence band, then the technique is called *ultraviolet photoelectron spectroscopy* (UPS) [7]. The kinetic energy $E_{kin}$ of the photoelectrons contains information of the binding energy $E_B$ of the respective energy level according to the following relation:

$$E_B = h\nu - E_{kin} - \phi_s, \tag{3.1}$$

where $\phi_s$ is the work function of the the material, the energetic difference between the Fermi level and the vacuum level. In an XPS- or UPS-experiment one plots the intensity of the detected electrons versus the energy. The discrete peaks reflect the binding energies, which are specific to each chemical element.

In the case of nanomeshes, $\sigma$-band and $\pi$-band splitting is observed, originating from the two distinct height levels of the corrugated surface combing slightly different binding energies.

# Bibliography

[1] G. Binnig, H. Rohrer, C. Gerber, and E. Weibel: "Surface Studies by Scanning Tunneling Microscopy." *Phys. Rev. Lett.* **49**(1), 57–61 (1982), doi:10.1103/PhysRevLett.49.57.

[2] L. E. C. van de Leemput and H. van Kempen: "Scanning Tunneling Microscopy." *Rep. Prog. Phys.* **55**(8), 1165–1240 (1992), doi:10.1088/0034-4885/55/8/002.

[3] G. Binnig and H. Rohrer: "In touch with atoms." *Rev. Mod. Phys.* **71**(2), S324–S330 (1999), doi:10.1103/RevModPhys.71.S324.

[4] C. Davisson and L. H. Germer: "Diffraction of electrons by a crystal of nickel." *Phys. Rev.* **30**(6), 705–740 (1927), doi:10.1103/PhysRev.30.705.

[5] C. Davisson and L. H. Germer: "The scattering of electrons by a single crystal of nickel." *Nature* **119**, 558–560 (1927), doi:10.1038/119558a0.

[6] E. G. McRae: "Self-Consistent Multiple-Scattering Approach to Interpretation of Low-Energy Electron Diffraction." *Surf. Sci.* **8**(1-2), 14 (1967), doi:10.1016/0039-6028(67)90071-4.

[7] Siegbahn: *ESCA; Atomic, molecular and solid state structure studied by means of electron spectroscopy.* Nova acta regiae societatis scientiarum Upsaliensis, ser. 4, Uppsala (1967).

# Chapter 4

# Nanomeshes

## 4.1 Introduction

Nanotemplates are attracting much interest in the field of materials science research. They can be used to produce well-ordered arrays of single molecules and nanoparticles with nanometer-scale periodicity [1, 2, 3, 4]. In this context, self-organized nanotemplates are more and more the focus of investigations, due to their fairly easy fabrication. When *h*-BN- and graphene single layers are grown on substrates with slightly different lattice parameters, as Rh(111) or Ru(0001), they form commensurate superstructures, so-called *nanomeshes* [5, 6, 7]. Due to the lattice mismatch and the resulting varying strength of interaction with the substrate [8, 9, 10, 11, 12, 13] across the surface, the surfaces tend to corrugate, hence varying the height across the surface in a regular way. These $sp^2$ hybridized layers have strong $\sigma$ in-plane bonds, but also surprisingly strong $\pi$ out-of-plane bonds (see Chapter 8). Depending on the substrate type these materials are grown on and their lattice mismatch to them, they might form nanomeshes, but they can also form $1 \times 1$ superstructures [14] or moiré-patterns, lacking any corrugations [15].

It has been shown that nanomeshes are stable in air [16] (see Section 5) in aqueous solutions [1], and remain stable up to very high temperatures [17] (see Section 6). Conceptually the *h*-BN and graphene nanomeshes are very similar, however graphene has attracted much more attention due to its unique electronic properties - it is a gapless semiconductor. For its application in making electronic devices the introduction of a bandgap is crucial. Recently it was reported that the growth on substrates can alter the electronic properties of graphene significantly; it can become metallic [18] due to a shift of the Fermi energy $E_F$, but it can also be that a bandgap is opened and it exhibits semiconducting behaviour [19]. These findings suggest the possibility of preparing semiconducting graphene layers for future carbon-based nanoelectronic devices via direct deposition onto strongly interacting substrates.

$h$-BN on the other hand is purely insulating, even when grown on a substrate. Although the $h$-BN and graphene are similar from a structural point of view, they are very different regarding their electronic properties. The similarities of these structures and the interesting electronic structure of graphene, altered when grown on substrates and the potential use for nanotemplates make these materials highly interesting from a detailed structural point of view.

This chapter focuses on the properties of the nanomeshes investigated in this thesis, namely single layers of $h$-BN and of graphene on the surfaces of the transition metals Rh(111) and Ru(0001). A more extended overview and review about these systems can be found elsewhere [4, 20, 21, 22, 23]. First the two surfaces of Ru(0001) and Rh(111) are described, then the focus turns to the $sp^2$ hybridized nanomesh $h$-BN and graphene. After a short overview of the electronic properties of these materials, a motivation for the analysis of these systems with SXRD is given.

## 4.2 hcp(0001)- and fcc(111)-surfaces

Ruthenium is a transition metal, with the atomic number of $Z = 44$. It crystallizes in the hexagonal close packed (hcp) structure. Its lattice constants are $a = 2.700$ Å, $b = 2.700$ Å, $c = 4.277$ Å [24]. Rhodium on the other hand, is a transition metal with the atomic number $Z = 45$, which crystallizes in a face centered cubic structure. The lattice constants of rhodium are $a = 2.689$ Å, $b = 2.689$ Å, $c = 6.587$ Å [24]. The (hcp) and the (fcc) structures both have a packing factor of 0.74, consist of closely packed planes of atoms, and have a coordination number of 12. The difference between the (hcp) and (fcc) structures is the stacking sequence.

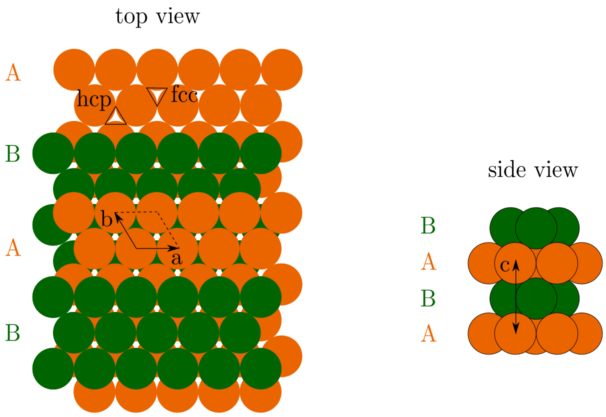

**Figure 4.1:** Schematic view of the Ru(0001)-surface. The structure starts with a layer A, on top of which one puts layer B, filling up the hcp-sites, and leaving hence the fcc-sites free. The third layer is positioned on top of the first one, hence the stacking sequence follows the ABABABA...-scheme.

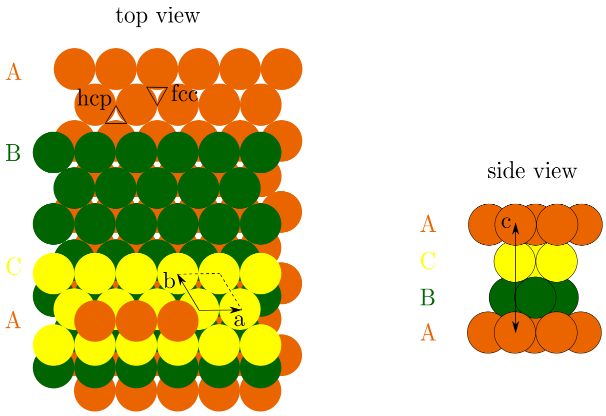

**Figure 4.2:** Schematic view of the Rh(111)-surface. The structure starts with a closed-packed A-layer, followed by a B-layer, which fills up the (hcp)-sites. The following, third layer C, fills out the (fcc)-sites. This leads to a ABCABCABC... stacking sequence. Hence when looked from a top view, there are no holes in this structure.

The (hcp) layers cycle among the two equivalent shifted positions whereas the fcc layers cycle between three positions. As can be seen in Figure 4.1, the (hcp) structure contains only two types of planes with an alternating ABAB arrangement. Note how the atoms of the third plane are in exactly the same position as the atoms in the first plane. However, the fcc structure (see Figure 4.2) contains three types of planes with a ABCABC arrangement. Here the atoms in rows A and C are no longer aligned.

## 4.3 $sp^2$-hybridization

In order to explain the hexagonal honeycomb structure of $sp^2$-hybridized meshes, as *h*-BN and graphene, 3 orbitals in the hybrid set are required.

Let us consider graphene as an example of $sp^2$-hybridization. In the ground-state, carbon has a $1s^2 2s^2 2p_x^1 2p_y^1$ electronic configuration (see Figure 4.3). The first step in the process of $sp^2$-hybridization is that the nucleus attracts one of the electrons in the valence band, which will make one of the two $2s$-electrons hop to the free $2p_z$ orbital. This gives 4 non degenerate energy states. Because of this new electronic configuration the effective core potential has increased and the orbital structure reorganizes: The $2s$ orbital is mixed with two of the three available $2p$ orbitals, namely $2p_x$,$2p_y$, forming three $sp^2$ hybridized, energetically degenerate orbitals (see Figure 4.3). The name $sp^2$ comes from the fact, that one $s$-orbital and two $p$-orbitals are involved in this process.

The unit cell of an $sp^2$-hybridized layer is made of 2 atoms (see Figure 4.4). The corresponding Brillouin zone in $k$-space shows six equivalent K-points. If the two atoms are identical (as in free-standing graphene), the valence and conduction band are degenerate. When the sublattice symmetry is broken, (as in *h*-BN) the K and K' points are no longer degenerate anymore.

## 4.4 Moiré patterns

In the case of *h*-BN and graphene grown on substrates, it is important to know whether the structure formed is a moiré pattern or a commensurate superstructure. A moiré pattern appears when a lattice is superposed to another one with different lattice constants. The resulting structure has a much larger periodicity than either of the original patterns (see Figure 4.5). If one represents the patterns with wavevectors, $\vec{k}_1$ and $\vec{k}_2$, the periodicity of the moiré pattern is

$$\vec{k}_{\text{moiré}} = \Delta\vec{k} = \vec{k}_2 - \vec{k}_1. \tag{4.1}$$

Certain structural techniques such as STM are unable to distinguish between a moiré structure and a true corrugated nanomesh superstructure, as it is difficult to differentiate between changes

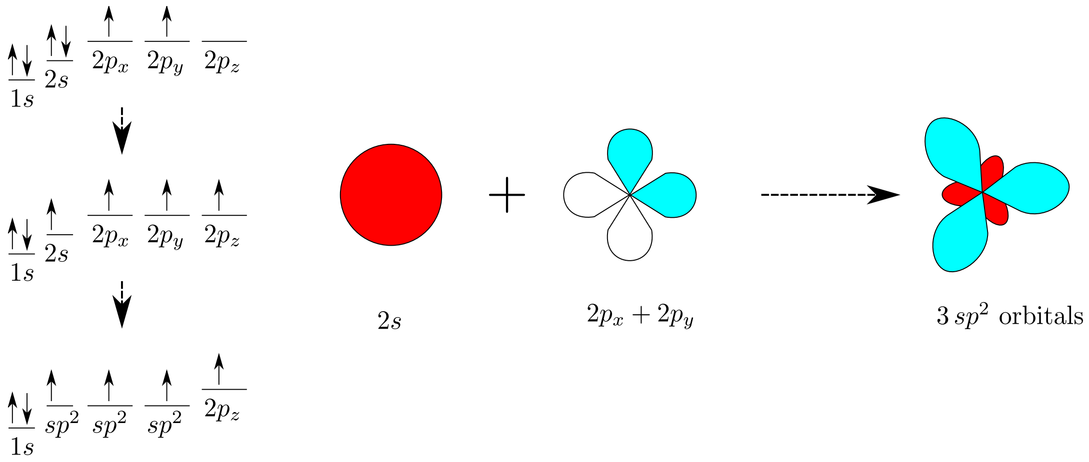

**Figure 4.3:** The $sp^2$-hybridization in graphene. First one of the two $2s$-electrons hops to the free $2p_z$-state. Due to a increase in the effective core potential the orbital structure reorganizes. The $2s$-orbital mixes with two of the three $2p$-orbitals, which leads to three $sp^2$ energetically degenerate hybridized orbitals.

in electron density and vertical shifts in atomic positions. This problem can be overcome by using diffraction techniques for the investigations, e.g., LEED or SXRD.

## 4.5 Hexagonal Boron Nitride ($h$-BN) on transition metal surfaces

In $h$-BN crystals (see Figure 4.6), alternating boron (B) and nitrogen (N) atoms form a 2-dimensional plane. The strong in-plane $sp^2$-hybridized bonds between two atoms are of a covalent character. These planes are stacked on top of each other such that each boron of the next layer is on top of another boron. They are held together via weak van der Waals interactions [25]. The lattice constants are $a = b = 2.504$ Å and $c = 6.660$ Å [26].

One can deposit single $h$-BN layers on transition metal surfaces via chemical vapor deposition (CVD) of borazine $(HBNH)_3$ [20]. On some surfaces, such as Pd(111) [27], Pt(111) [28], and Ni(111) [29, 30, 31, 32], the $h$-BN monolayer is flat. Because of a strong reduction of the surface reactivity once the flat monolayer of BN has been deposited the growth rate of the BN subsequently becomes extremely small. This facilitates the growth of a single monolayer film [33]. The electronic properties of this layer are almost independent of the substrate [34, 35].

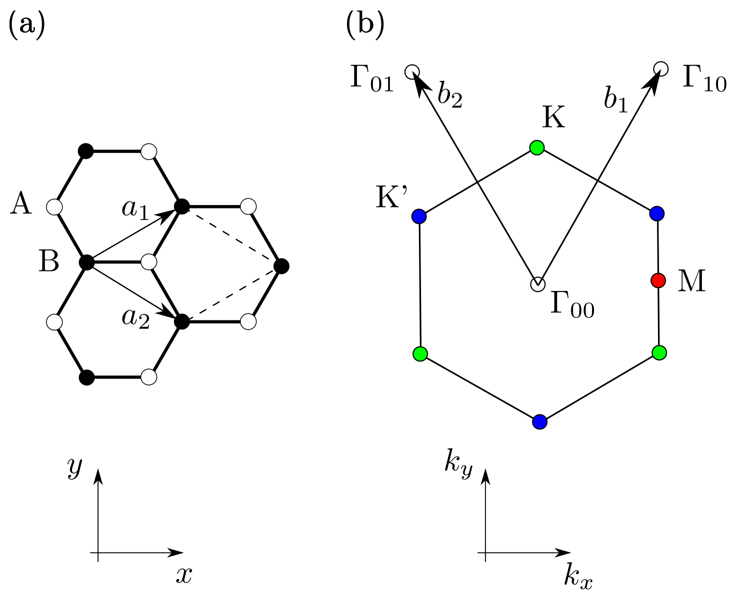

**Figure 4.4:** (a) The real space unit cell of $sp^2$-hybridized layers with lattice vectors $a_1$ and $a_2$ and the two atoms A and B is shown. The $sp^2$-hybridization couples the two sublattices A and B. (b) The corresponding Brillouin zone in $k$-space is shown. $K$ and $K'$ are nonequivalent, when the symmetry of the sublattice is broken, as in the case of $h$-BN, which consists of two different atoms. For the case of free-standing graphene, where the two sublattices are indistinguishable, this leads to a gap-less semiconductor with Dirac points at the K points.

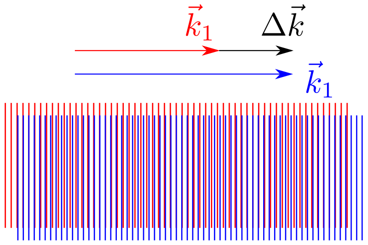

**Figure 4.5:** A moiré pattern arises by the superposition of two regular patterns with slightly different lattice constants. When represented by two wave vectors, $\vec{k}_1$ and $\vec{k}_2$, the difference of the two $\Delta\vec{k} = \vec{k}_2 - \vec{k}_1$ gives the much smaller wavevector than the two original patterns had, and hence a larger distance between two maxima in the pattern.

The bonding between the mentioned substrates and the $h$-BN-layer is very weak, the structures formed are either of type $1 \times 1$ or they are flat moiré structures [27]. As described in Section 4.4 moiré patterns are not necessarily nanomeshes. The SXRD signal of a moiré pattern lacks the

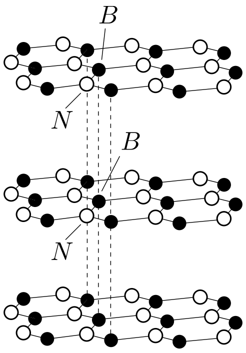

**Figure 4.6:** The layer stacking in *h*-BN crystals. The N sits exactly on top of a N of the subsequent layer, and so does the B.

"real reconstruction peak" (see Section 4.7).

On the other hand nanomeshes, defined by their periodic corrugation, have been observed on Rh(111) and Ru(0001) surfaces [5, 17]. Nanomesh formation is driven by the fact, that boron is attracted to the metallic surface, while nitrogen is repelled. There is a slight transfer of charge from *h*-BN-layer to the substrate. Since the $p_z$-state of the nitrogen is lower than the $p_z$-state of boron (see Figure 4.7), there is a small charge transfer from the boron $p_z$-level to the nitrogen $p_z$-level. Since the substrate is negatively charged, the negatively charged nitrogen will be repelled, while the positively charged boron will be attracted.

Due to a strong covalent interaction of the boron with the substrate's $d_z$-orbitals, the bonding and antibonding bands split. While the bonding orbitals of both elements are below the Fermi level, the boron antibonding band contribution remains well above the Fermi level of the system whereas part of the nitrogen band contribution antibonding is below the Fermi level and is thus partially filled (see Figure 4.7). Due to the lattice mismatch this situation changes gradually with the nanomesh-substrate registry, resulting in certain regions being attracted, where the boron is on top of a substrate atom and others being repelled, where the nitrogen are on top of the substrate atom. This leads to the formation of a commensurate superstructure, which in the case of *h*-BN on Rh(111) consists of $13 \times 13$ *h*-BN on $12 \times 12$ Rh (called 13-on-12) [5, 16, 36] (see Chapter 5 and Chapter 6), while for *h*-BN on Ru(0001) the structure is $14 \times 14$ *h*-BN on $13 \times 13$ Ru (i.e., 14-on-13) (see Chapter 7).

The exact binding energies have been calculated by ab-initio calculations [12], where the $4d$

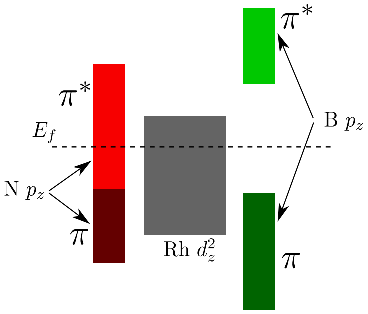

**Figure 4.7:** Diagram of the density of states around the Fermi level of $h$-BN grown on Rh(111) [11]. Because of the strong interaction of the $p_z$-orbital of the boron and the $d_z$-orbital of the Rh(111) surface, the $\pi$-band split. The antibonding band contribution of the boron remains above the Fermi level, whereas the N antibonding band is below the Fermi level and thus partially filled. This makes the B being attracted and the N being repelled. When grown on a substrate with a large enough lattice mismatch, this situation changes over a large period, and the formation of a superstructure is stimulated.

transition metals exhibit the strongest bonding. It is claimed that the bond strength correlates with the $d$-band occupancy (see Table 4.1). The more occupied the $d$-shell of the element is, the lower is the binding energy.

The critical point determining whether a nanomesh, or a more free floating flat layer is formed (producing a moiré pattern) is the lattice mismatch. In the following Table 4.1 the lattice mismatches are listed for $h$-BN for various substrates, whereby the lattice mismatch is defined by Zangwill *et al.* [37] as:

$$M = \frac{a_{h-\mathrm{BN}} - a_s}{a_s}, \tag{4.2}$$

where $a_{h-\mathrm{BN}}$ is the in-plane lattice constant of $h$-BN and $a_s$ is the in-plane lattice constant of the substrate surface.

## 4.6 Graphene on transition metal surfaces

Graphite has a crystal structure very similar to that of $h$-BN. Two-dimensional sheets of carbon arranged in a honeycomb network containing two atoms per unit cell, $A_1$ and $A_2$, stack on top of each other to form the crystal. In contrast to $h$-BN the stacking of the sheets follows the

| Element | Ni | Rh | Ru | Pd | Pt |
|---|---|---|---|---|---|
| Electronic configuration | [Ar]$4s^2 3d^8$ | [Kr]$5s^1 4d^8$ | [Kr]$5s^1 4d^7$ | [Kr]$4d^{10}$ | [Xe]$6s^1 4f^{14} 5d^9$ |
| Structure | fcc | fcc | hcp | fcc | fcc |
| Surface | (111) | (111) | (0001) | (111) | (111) |
| $a_s$ | 2.489 Å | 2.689 Å | 2.700 Å | 2.751 Å | 2.772 Å |
| $M$ | 0.60% | -6.88% | -7.26% | -8.98% | -9.67% |

**Table 4.1:** Structure and in-plane lattice (in surface coordinates) constants of some transition metals [24, 38]. The lattice mismatch compared to a bulk lattice constant of $h$-BN = 2.504 Å [39] are given by the definition $M$ by Zangwill *et al.* [37]

.

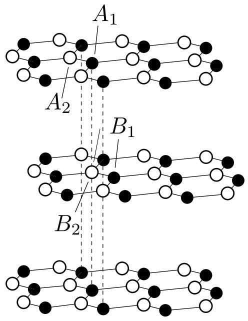

**Figure 4.8:** The stacking of graphite. Graphite follows the Bernal stacking scheme: $A_1$ and $B_2$ atoms of the consecutive layers are on top of each other, but $A_2$ and $B_1$ are obviously not, the $B_2$ is under the unoccupied center of the adjacent cell.

*Bernal stacking* ABAB scheme shown in Figure 4.8. It has an in-plane lattice constant of $a = b = 2.462$ Å and a $c$ lattice constant of 6.708 Å.

Graphene, the constituent monolayer sheet of graphite, was discovered in 2004 by Novoselov *et al.* [40]. Apart from the fact that graphene has two equivalent carbon atoms in one unit cell it is structurally identical to monolayer $h$-BN. Although the two materials are isoelectronic, their electronic properties are completely different: while $h$-BN is an insulator, graphene has remarkable electronic properties and is a zero-gap semiconductor [23, 41, 42, 43]. The reason for this lies in the fact that graphene has two identical atoms in the unit cell.

Interaction between the $sp^2$ orbitals of two neighbouring carbon atoms, forms the bonding $\sigma$

band and the antibonding $\sigma^*$ band. $\pi$ and $\pi^*$ bands are formed by the overlap of the delocalized $2p_z$ orbitals perpendicular to the molecular plane.

Since $\sigma$ bonds are very strong, the occupied $\sigma$ bands, and the unoccupied $\sigma^*$ band are well separated - the $\sigma$ band is well below the Fermi level and is a valence band, whereas the $\sigma^*$ is empty and is a conduction band. Each $2p_z$ orbital has one extra electron, the $\pi$ band is half filled, the $\pi^*$ band is empty.

The electronic properties are determined by the energy levels around the Fermi energy, hence the $\sigma$ and $\sigma^*$ bands can be neglected, and only the $\pi$ and $\pi^*$ bands are considered. When calculating the dispersion relations according to a tight binding model for the two equal atoms in the unit cell, the valence and conduction band meet at a crossing exactly at the K point of the Brillouin zone, the Dirac point, giving rise to a single state at the Fermi energy. The valence and conduction bands are degenerate at these points, graphene is a zerogap semiconductor. This results in a relativistic behaviour of graphene's effectively massless charge carriers (the Dirac fermions), which is the origin of the intriguing physical properties of freestanding graphene [see Figure 4.9 (a)].

In the case of *h*-BN, where the unit cell consists of two different atoms, the calculation leads to a band gap opening. One can also break the equivalence of the two carbon atoms in graphene, by adsorbing it on a metal substrate resulting in a change of the electronic properties [18, 19, 44, 45, 46, 47, 48]. The same is true when graphene is grown on BN(0001) [49, 50], or on SiC(0001) [47, 51]. The atoms within the graphene unit cell can no longer be considered as being identical, since the $d_z$-orbital of the substrate starts to mix with the $p_z$-orbital of graphene and depending at which site the graphene atoms adsorb, they interact with different strengths. The interaction with the substrate opens up a bandgap. This makes these systems very interesting, since it provides an insight about the interaction of the graphene layer with the substrate and also potentially allows one to tune its physical properties. Even on strongly interacting substrates, graphene can recover its original electronic properties and behave as if it were free-standing, by oxygen intercalation between the graphene and the substrate, as has been shown for the case of Ru(0001) [52].

Investigations of graphene/Ir(111) found that the system forms a moiré pattern with a weak interaction with the substrate [15]. The band structure of free-standing graphene is

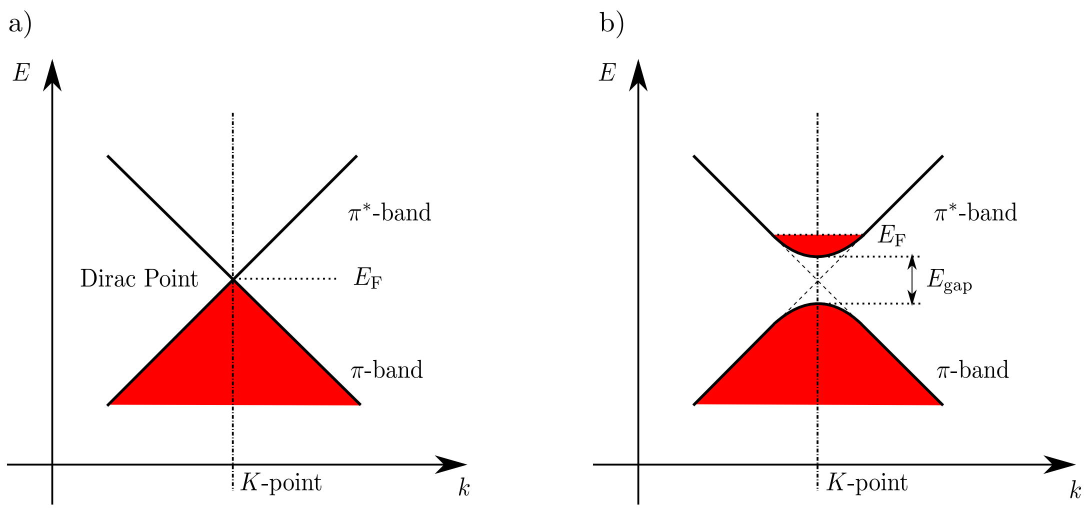

**Figure 4.9:** a) The dispersion relation of freestanding graphene. The $\pi$- and $\pi^*$-band meet at the dirac point. Here the valence and conduction bands are degenerate and graphene is a gapless semiconductor. b) The dispersion relation of graphene can change when grown on a substrate. Charge transfer between substrate and graphene shifts the Fermi energy and a band gap $E_{\text{gap}}$ can open, caused by the strong interaction of the $p_z$-orbital with the $d_z$-orbital of the substrate. Graphene shows metallic or semiconducting behaviour.

almost perfectly preserved [53] and it is only 0.2 eV. However, unlike free-standing graphene, where the Fermi level lies at the conical point, the Fermi level is shifted for weak interacting substrates , there is charge transfer between the graphene and the substrate, and the graphene is doped $n$-type or $p$-type [45].

In the case of graphene on Ni(111) [54], where a $1 \times 1$ superstructure was observed the $2p_z$ orbitals of graphene hybridize with the $3d_z$ orbitals of Ni. As a result some charge is shifted from the $3d$ band into the empty $\pi^*$ states of graphene, causing an energy shift of the $\pi$ system and a band gap opening [20]. Very similar effects have been seen for graphene/Ru(0001), where a 2 eV downshifted $\pi$ band [18, 44] opens a band gap of several eV.

In contrast to the graphene/Ni(111) case, here a superstructure is formed [55], although there are large areas in the superstructure where the A and B atoms reside on similar sites as in the case of graphene/Ni(111). The formation of superstructures leads to locally different electronic structures, depending on where the atoms above the Ru(0001) surface atoms are located [13], hence to a modulated electronic structure.

### 4.6.1 The Mermin-Wagner Theorem

Graphene was for a long time believed to not exist, due to structural instabilities. The question whether a 2D crystal can be stable was addressed first in 1934 by Peierls *et al.* [56]. It was shown that in the standard harmonic approximation, thermal fluctuations would destroy the long-range order. Mermin and Wagner [57] proved more than 30 years later, that magnetic long-range order could not exist in 2D-crystals, in the *Mermin-Wagner Theorem*. Later they also extended their theory to crystalline order in 2D [58]. They showed that the amplitude of long-wavelength fluctuations grow logarithmically with the size of a 2D structure, and would therefore become infinite in structures of infinite size. A sufficiently large 2D structure, in the absence of applied lateral tension, will bend and crumple to form a fluctuating 3D structure. Ripples have been observed in suspended layers of graphene, and it has been proposed that the ripples are caused by thermal fluctuations in the material [59, 60], hence the *Mermin-Wagner theorem* is not violated by graphene, as graphene does not appear to be strictly a 2D structure.

## 4.7 Nanomeshes investigated with LEED and SXRD

As pointed out in Section 4.4 often the problem arises to distinguish between a commensurate superstructure, a nanomesh, and a moiré pattern, and that it is much easier to approach the problem in reciprocal space. However, this is not the full truth. As mentioned in Section 3.3 due to the large cross-section of the electrons interacting with matter, scattering dynamic LEED theory is necessary for the determination of atomic structures. This makes computation and analysis of LEED spot-intensities much more difficult than it is for SXRD. In particular if looking at the reconstruction peaks, in LEED it is not possible to distinguish at first sight between a corrugated commensurate layer, a nanomesh, and a "free floating layer". Here we will focus on the $h$-BN/Rh(111) system (see Section 5 and 6) as an example of nanomeshes, and discuss the above mentioned problem in detail on *the real reconstruction peak.*

Consider the one-dimensional case in the in-plane region near the first Bragg peak $(h, k) = (1, 0)$, and at a non-zero out-of-plane component, fixed at $l = 0.4$. We start with the simplest case, of a non-reconstructed surface [see Figure 4.10 (a)], twelve boron atoms match up with 12 rhodium atoms. The intensity produced along the $h$-direction will only be visible at $h = 1 = 12/12$. There are no superstructure rods, since there is no superstructure. If we now consider the moiré pattern produced by 13 boron atoms matching up with 12 rhodium atoms the diffraction pattern signal in the $h$-direction will include in addition to the Bragg-rod, produced by the rhodium, also a superstructure-rod showing up at $h = 13/12$ [see Figure 4.10 (b)]. The signal is the Bragg-rod of the boron. Importantly, for a moiré structure, one observes no signal at $h = 11/12$. Note that although this is true for SXRD, which satisfies the kinematical approximation, for strongly scattered low-energy electrons (as in LEED) multiples of the Bragg-rod, also at $h = 11/12$, will be seen even in a moiré structure. Hence LEED is unable to provide immediate informations on the nature of the superstructure, e.g., whether it is a true nanomesh or a flat moiré structure, at least not without any time consuming dynamical calculation.

We now introduce a corrugation on the boron, which can have shape as long as its periodicity is the same as that of the 12 underlying rhodium atoms. One now sees all the $h = 1/12$ Fourier-components [see Figure 4.10 (c)]. This is caused by the fact that the unit cell is now 12 times larger than the rhodium unit cell. In particular the satellite on $h = 12/12$, which sits at the same location as the large signal coming from the bulk-rhodium, and on $h = 14/12$ will be the strongest ones. Lastly, we include a similar corrugation on the uppermost layers of the substrate which will make, arguing the same way, appearing again all $h = 1/12$-rods, the strongest satellites of the Bragg-rod are the next ones, hence the $h = 11/12$ and the $h = 13/12$. In summary we will have a very strong rhodium Bragg-rod at the $h = 12/12$-position, a strong satellite coming from the corrugation of the rhodium on the $h = 11/12$-position and a strong rod on the $h = 13/12$-position coming from the strongest satellite of the rhodium and from the boron Bragg-rod. One can say, that although the atomic form factors for B, N, and C, are not suitable for investigating these materials with photons, the special situation of having signal coming from the weakly corrugated substrate, and signal coming from the light scattering adsorbed layers on the same rods, gives us the possibility of looking at these materials using SXRD. More than that, since the substrates investigated in this thesis, rhodium and ruthenium, both are strong scattering materials, the contrast to $h$-BN and graphene is high, and therefore the signals are better distinguishable.

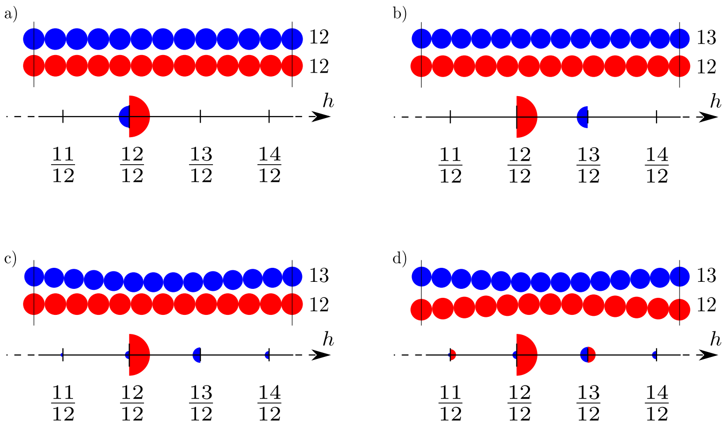

**Figure 4.10:** Schematic view of a nanomesh. The intensities in reciprocal space reflect the situation in real space. (a) When 12 boron atoms match up with 12 rhodium atoms in two flat layers, all the intensity has to be expected on the $h = 12/12$-position, since there is no reconstruction and both Bragg-rods from adsorbate and substrate meet at the same point in reciprocal space. (b) When 13 boron atoms match on top of 12 substrates atoms, the Bragg-rod of the boron will be shifted towards higher $q$-values, namely $h = 13/12$, since the lattice spacings between two boron atoms is $12/13$. (c) If one includes in a corrugation on the boron, defining a superlattice of 12 rhodium atoms, the result is the appearance of satellite spots of the boron- Bragg-rod, the strongest ones are the $h = 12/12$-rod and the $h = 14/12$-rod. (d) Corrugating the substrate, has a similar effect as seen with the adsorbate layer. Satellites appear next to the rhodium Bragg-rod of the rhodium, here the strongest ones are the $h = 11/12$ and the $h = 13/12$.

Using this method, we established the superstructures in Chapter 6 7 8 9 to be corrugated and commensurate. This principle can be applied exactly the same way to a 25/23-reconstruction. There the situation is slightly more complicated, since a doubling of the frequency of the superstructure alone, makes every even rod be forbidden.

# Bibliography

[1] S. Berner, M. Corso, R. Widmer, O. Groening, R. Laskowski, P. Blaha, K. Schwarz, A. Goriachko, H. Over, S. Gsell, M. Schreck, H. Sachdev, T. Greber, and J. Osterwalder: "Boron Nitride Nanomesh: Functionality from a Corrugated Monolayer." *Angew. Chem. Int. Ed.* **46**(27), 5115 (2007), doi:10.1002/anie.200700234.

[2] A. Goriachko, A. A. Zakharov, and H. Over: "Oxygen-etching of h-BN/Ru(0001) nanomesh on the nano- and mesoscopic scale." *J. Phys. Chem. C* **112**(28), 10423–10427 (2008), doi: 10.1021/jp802359u.

[3] H. Dil, J. Lobo-Checa, R. Laskowski, P. Blaha, S. Berner, J. Osterwalder, and T. Greber: "Surface trapping of atoms and molecules with dipole rings." *Science* **319**(5871), 1824–1826 (2008), doi: 10.1126/science.1154179.

[4] A. Goriachko and H. Over: "Modern Nanotemplates Based on Graphene and Single Layer h-BN." *Z. Phys. Chem.* **223**(1-2), 157–168 (2009), doi:10.1524/zpch.2009.6030.

[5] M. Corso, W. Auwärter, M. Muntwiler, A. Tamai, T. Greber, and J. Osterwalder: "Boron Nitride Nanomesh." *Science* **303**(5655), 217–220 (2004), doi:10.1126/science.1091979.

[6] S. Marchini: *Scanning Tunneling Microscopy and Spectroscopy investigations of Graphene on Ru(0001) and (CO+O) on Rh(111)*. Ph.D. thesis, Ludwig-Maximilians-Universität München (2007).
URL `http://edoc.ub.uni-muenchen.de/7975`

[7] S. Marchini, S. Günther, and J. Wintterlin: "Scanning tunneling microscopy of graphene on Ru(0001)." *Phys. Rev. B* **76**(7), 075429 (2007), doi:10.1103/PhysRevB.76.075429.

[8] A. B. Preobrajenski, M. A. Nesterov, M. L. Ng, A. S. Vinogradov, and N. Mårtensson: "Monolayer h-BN on lattice-mismatched metal surfaces: On the formation of the nanomesh." *Chem. Phys. Lett.* **446**(1-3), 119–123 (2007), doi:10.1016/j.cplett.2007.08.028.

[9] A. B. Preobrajenski, A. S. Vinogradov, M. L. Ng, E. Ćavar, R. Westerström, A. Mikkelsen, E. Lundgren, and N. Mårtensson: "Influence of chemical interaction at the lattice-mismatched h-BN/Rh(111) and h-BN/Pt(111) interfaces on the overlayer morphology." *Phys. Rev. B* **75**(24), 245412 (2007), doi:10.1103/PhysRevB.75.245412.

[10] R. Laskowski, P. Blaha, T. Gallauner, and K. Schwarz: "Single-Layer Model of the Hexagonal Boron Nitride Nanomesh on the Rh(111) Surface." *Phys. Rev. Lett.* **98**(10), 106802 (2007), doi: 10.1103/physrevlett.98.106802.

[11] R. Laskowski and P. Blaha: "Unraveling the structure of the h-BN/Rh(111) nanomesh with ab initio calculations." *J. Phys. Condens. Matter* **20**(6), 064207 (2008), doi:10.1088/0953-8984/20/6/064207.

[12] R. Laskowski, P. Blaha, and K. Schwarz: "Bonding of hexagonal BN to transition metal surfaces: An ab initio density-functional theory study." *Phys. Rev. B* **78**(4), 045409 (2008), doi: 10.1103/PhysRevB.78.045409.

[13] B. Wang, M. L. Bocquet, S. Marchini, S. Günther, and J. Wintterlin: "Chemical origin of a graphene moiré overlayer on Ru(0001)." *Phys. Chem. Chem. Phys.* **10**(24), 3530–3534 (2008), doi: 10.1039/b801785a.

[14] W. Auwärter, H. Suter, H. Sachdev, and T. Greber: "Synthesis of One Monolayer of Hexagonal Boron Nitride on Ni(111) from B-Trichloroborazine $(ClBNH)_3$." *Chem. Mater.* **16**(2), 343 (2004), doi:10.1021/cm034805s.

[15] A. T. N'Diaye, J. Coraux, T. N. Plasa, C. Busse, and T. Michely: "Structure of epitaxial graphene on Ir(111)." *New J. Phys.* **10**, 043033 (2008), doi:10.1088/1367-2630/10/4/043033.

[16] O. Bunk, M. Corso, D. Martoccia, R. Herger, P. R. Willmott, B. D. Patterson, J. Osterwalder, J. F. van der Veen, and T. Greber: "Surface X-ray diffraction study of boron-nitride nanomesh in air." *Surf. Sci.* **601**(2), L7–L10 (2007), doi:10.1016/J.Susc.2006.11.018.

[17] A. Goriachko, Y. He, M. Knapp, and H. Over: "Self-Assembly of a Hexagonal Boron Nitride Nanomesh on Ru(0001)." *Langmuir* **23**(6), 2928–2928 (2007), doi:10.1021/la062990t.

[18] T. Brugger, S. Günther, B. Wang, J. H. Dil, M.-L. Bocquet, J. Osterwalder, J. Wintterlin, and T. Greber: "Comparison of electronic structure and template function of single-layer graphene and a hexagonal boron nitride nanomesh on Ru(0001)." *Phys. Rev. B* **79**(4), 045407 (2009), doi: 10.1103/PhysRevB.79.045407.

[19] S.-Y. Kwon, C. V. Cobanu, V. Petrova, V. B. Shenoy, J. Bareño, V. Gambin, I. Petrov, and S. Kodambaka: "Growth of Semiconducting Graphene on Palladium." *Nano Lett. (accepted)* (2009), doi:10.1021/nl902140j.

[20] C. Oshima and A. Nagashima: "Ultra-thin epitaxial films of graphite and hexagonal boron nitride on solid surfaces." *J. Phys. Condens. Matter* **9**(1), 1–20 (1997), doi:10.1088/0953-8984/9/1/004.

[21] T. Greber: "Graphene and Boron Nitride Single Layers." *Preprint at http://arxiv:0904.1520v1* (2009).

[22] J. Wintterlin and M. L. Bocquet: “Graphene on metal surfaces.” *Surf. Sci.* **603**(10-12), 1841–1852 (2009), doi:10.1016/j.susc.2008.08.037.

[23] A. H. C. Neto, F. Guinea, N. M. R. Peres, K. S. Novoselov, and A. K. Geim: “The electronic properties of graphene.” *Rev. Mod. Phys.* **81**(1), 109–162 (2009), doi:10.1103/RevModPhys.81.109.

[24] N. W. Ashcroft and N. D. Mermin: *Solid State Physics*. Holt, Rinehart and Winston, New York (1969).

[25] N. Ooi, A. Rairkar, L. Lindsley, and J. Adams: “Electronic structure and bonding in hexagonal boron nitride.” *J. Phys. Condens. Matter* **18**(1), 97 (2006), doi:10.1088/0953-8984/18/1/007.

[26] V. L. Solozhenko, G. Will, and F. Elf: “Isothermal Compression of Hexagonal Graphite-Like Boron-Nitride up to 12 Gpa.” *Solid State Commun.* **96**(1), 1–3 (1995), doi:10.1016/0038-1098(95)00381-9.

[27] M. Morscher, M. Corso, T. Greber, and J. Osterwalder: “Formation of single layer h-BN on Pd(111).” *Surf. Sci.* **600**(16), 3280 (2006), doi:10.1016/j.susc.2006.06.016.

[28] E. Ćavar, R. Westerström, A. Mikkelsen, E. Lundgren, A. S. Vinogradov, M. L. Ng, A. B. Preobrajenski, A. A. Zakharov, and N. Mårtensson: “A single h-BN layer on Pt(111).” *Surf. Sci.* **602**(9), 1722–1726 (2008), doi:10.1016/J.Susc.2008.03.008.

[29] Y. Gamou, M. Terai, A. Nagashima, and C. Oshima: “Atomic structural analysis of a monolayer epitaxial film of hexagonal boron nitride Ni(111) studied by LEED intensity analysis.” *Sci. Rep. RITU* **44**(2), 211–214 (1997).

[30] W. Auwärter, T. J. Kreutz, T. Greber, and J. Osterwalder: “XPD and STM investigation of hexagonal boron nitride on Ni(111).” *Surf. Sci.* **429**(1-3), 229–236 (1999), doi:10.1016/s0039-6028(99)00381-7.

[31] G. B. Grad, P. Blaha, K. Schwarz, W. Auwärter, and T. Greber: “Density functional theory investigation of the geometric and spintronic structure of h-BN/Ni(111) in view of photoemission and STM experiments.” *Phys. Rev. B* **68**(8), 085404 (2003), doi:10.1103/physrevb.68.085404.

[32] M. N. Huda and L. Kleinman: “h-BN monolayer adsorption on the Ni(111) surface: A density functional study.” *Phys. Rev. B* **74**(7), 075418 (2006), doi:10.1103/physrevb.74.075418.

[33] A. B. Preobrajenski, A. S. Vinogradov, and N. Mårtensson: “Ni 3dBN $\pi$ hybridization at the h-BNNi(111) interface observed with core-level spectroscopies.” *Phys. Rev. B* **70**(16), 165404 (2004), doi:10.1103/physrevb.70.165404.

[34] A. Nagashima, N. Tejima, Y. Gamou, T. Kawai, and C. Oshima: “Electronic Structure of Mono-

layer Hexagonal Boron Nitride Physisorbed on Metal Surfaces." *Phys. Rev. Lett.* **75**(21), 3918 (1995), doi:10.1103/physrevlett.75.3918.

[35] A. Nagashima, N. Tejima, Y. Gamou, T. Kawai, and C. Oshima: "Electronic dispersion relations of monolayer hexagonal boron nitride formed on the Ni(111) surface." *Phys. Rev. B* **51**(7), 4606 (1995), doi:10.1103/physrevb.51.4606.

[36] D. Martoccia, S. A. Pauli, T. Brugger, T. Greber, B. D. Patterson, and P. R. Willmott: "$h$−BN on Rh(111): Persistence of a commensurate 13-on-12 superstructure up to high temperatures." *Surf. Sci.* **604**(5-6), L9–L11 (2010), doi:10.1016/J.Susc.2009.12.016.

[37] A. Zangwill: *Physics at surfaces.* Cambridge University Press, Cambridge (1988).

[38] Entry [5 - 685] of database Powder Diffraction File PDF 2, Release 2001, International Centre for Diffraction Data (ICDD), Newton Square, Pennsylvania, USA.

[39] E. K. Sichel, R. E. Miller, M. S. Abrahams, and C. J. Buiocchi: "Heat-Capacity and Thermal-Conductivity of Hexagonal Pyrolytic Boron-Nitride." *Phys. Rev. B* **13**(10), 4607–4611 (1976), doi: 10.1103/PhysRevB.13.4607.

[40] K. S. Novoselov, A. K. Geim, S. V. Morozov, D. Jiang, Y. Zhang, S. V. Dubonos, I. V. Grigorieva, and A. A. Firsov: "Electric field effect in atomically thin carbon films." *Science* **306**(5296), 666–669 (2004), doi:10.1126/science.1102896.

[41] K. S. Novoselov, D. Jiang, F. Schedin, T. J. Booth, V. V. Khotkevich, S. V. Morozov, and A. K. Geim: "Two-dimensional atomic crystals." *PNAS* **102**(30), 10451–10453 (2005), doi: 10.1126/science.1102896.

[42] C. Berger, Z. M. Song, X. B. Li, X. S. Wu, N. Brown, C. Naud, D. Mayou, T. B. Li, J. Hass, A. N. Marchenkov, E. H. Conrad, P. N. First, and W. A. de Heer: "Electronic confinement and coherence in patterned epitaxial graphene." *Science* **312**(5777), 1191–1196 (2006), doi: 10.1126/science.1125925.

[43] H. B. Heersche, P. Jarillo-Herrero, J. B. Oostinga, L. M. K. Vandersypen, and A. F. Morpurgo: "Bipolar supercurrent in graphene." *Nature* **446**(7131), 56–59 (2007), doi:10.1038/Nature05555.

[44] F. J. Himpsel, K. Christmann, P. Heimann, D. E. Eastman, and P. J. Feibelman: "Adsorbate Band Dispersions for C on Ru(0001)." *Surf. Sci.* **115**(3), L159–L164 (1982), doi:10.1016/0039-6028(82)90379-X.

[45] P. A. Khomyakov, G. Giovannetti, P. C. Rusu, G. Brocks, J. van den Brink, and P. J. Kelly:

"First-principles study of the interaction and charge transfer between graphene and metals." *Phys. Rev. B* **79**(19), 195425 (2009), doi:10.1103/Physrevb.79.195425.

[46] E. Sutter, D. P. Acharya, J. T. Sadowski, and P. Sutter: "Scanning tunneling microscopy on epitaxial bilayer graphene on ruthenium (0001)." *Appl. Phys. Lett.* **94**(13), 133101 (2009), doi: 10.1063/1.3106057.

[47] X. Y. Peng and R. Ahuja: "Symmetry Breaking Induced Bandgap in Epitaxial Graphene Layers on SiC." *Nano Lett.* **8**(12), 4464–4468 (2008), doi:10.1021/Nl802409q.

[48] D. Eom, D. Prezzi, K. T. Rim, H. Zhou, M. Lefenfeld, S. Xiao, C. Nuckolls, M. S. Hybertsen, T. F. Heinz, and G. W. Flynn: "Structure and Electronic Properties of Graphene Nanoislands on Co(0001)." *Nano Lett.* **9**(8), 2844–2848 (2009), doi:10.1021/Nl900927f.

[49] T. Kawasaki, T. Ichimura, H. Kishimoto, A. A. Akbar, T. Ogawa, and C. Oshima: "Double atomic layers of graphene/monolayer h-BN on Ni(111) studied by scanning tunneling microscopy and scanning tunneling spectroscopy." *Surf. Rev. Lett.* **9**(3-4), 1459–1464 (2002), doi: 10.1142/S0218625X02003883.

[50] G. Giovannetti, P. A. Khomyakov, G. Brocks, P. J. Kelly, and J. van den Brink: "Substrate-induced band gap in graphene on hexagonal boron nitride: Ab initio density functional calculations." *Phys. Rev. B* **76**(7), 073103–1 (2007), doi:10.1103/PhysRevB.76.073103.

[51] S. Y. Zhou, G. H. Gweon, A. V. Fedorov, P. N. First, W. A. De Heer, D. H. Lee, F. Guinea, A. H. C. Neto, and A. Lanzara: "Substrate-induced bandgap opening in epitaxial graphene." *Nat. Mater.* **6**(10), 770–775 (2007), doi:10.1038/nmat2003.

[52] H. Zhang, Q. Fu, Y. Cui, D. L. Tan, and X. H. Bao: "Growth Mechanism of Graphene on Ru(0001) and $O_2$ Adsorption on the Graphene/Ru(0001) Surface." *J. Phys. Chem. C* **113**(19), 8296–8301 (2009), doi:10.1021/Jp810514u.

[53] I. Pletikosić, M. Kralj, P. Pervan, R. Brako, J. Coraux, A. T. N'Diaye, C. Busse, and T. Michely: "Dirac Cones and Minigaps for Graphene on Ir(111)." *Phys. Rev. Lett.* **102**(5), 056808 (2009), doi:10.1103/PhysRevLett.102.056808.

[54] G. Bertoni, L. Calmels, A. Altibelli, and V. Scrin: "First-principles calculation of the electronic structure and EELS spectra at the graphene/Ni(111) interface." *Phys. Rev. B* **71**(7) (2005), doi: 10.1103/PhysRevB.71.075402.

[55] D. Martoccia, P. R. Willmott, T. Brugger, M. Björck, S. Günther, C. M. Schlepütz, A. Cervellino, S. A. Pauli, B. D. Patterson, S. Marchini, J. Wintterlin, W. Moritz, and T. Greber:

"Graphene on Ru(0001): A 25×25 Supercell." *Phys. Rev. Lett.* **101**(12), 126102 (2008), doi: 10.1103/PhysRevLett.101.126102.

[56] R. Peierls: "The vacuum in Dirac's theory of the positive electron." *Proceedings of the Royal Society of London Series a-Mathematical and Physical Sciences* **146**(A857), 0420–0441 (1934), doi:10.1098/rspa.1934.0164.

[57] N. D. Mermin and H. Wagner: "Absence of Ferromagnetism or Antiferromagnetism in One- or 2-Dimensional Isotropic Heisenberg Models." *Phys. Rev. Lett.* **17**(22), 1133 (1966), doi: 10.1103/PhysRevLett.17.1133.

[58] N. D. Mermin: "Crystalline Order in 2 Dimensions." *Phys. Rev.* **176**(1), 250 (1968), doi: 10.1103/PhysRev.176.250.

[59] A. Fasolino, J. H. Los, and M. I. Katsnelson: "Intrinsic ripples in graphene." *Nat. Mater.* **6**(11), 858–861 (2007), doi:10.1038/nmat2011.

[60] J. M. Carlsson: "Buckle or break." *Nat. Mater.* **6**(11), 801–802 (2007), doi:10.1038/nmat2051.

# Chapter 5

# Surface X-ray diffraction study of boron-nitride nanomesh in air

The work presented in this chapter has been published in:

O. Bunk, M. Corso, D. Martoccia, R. Herger, P.R. Willmott, B.D. Patterson, J. Osterwalder, J.F. van der Veen, T. Greber: "Surface X-ray diffraction study of boron-nitride nanomesh in air." *Surf. Sci.* **601**(2), L7-L10 (2007),
doi:10.1016/J.Susc.2006.11.018 [a]

artikel1.pdf is the online version of the library Zentralbibliothek Zürich

## Abstract

The hexagonal boron-nitride nanomesh surface reconstruction on Rh(1 1 1) [Corso et al., Science 303 (2004) 217-220] has been investigated using surface x-ray diffraction utilizing synchrotron radiation. This unique structure has been found to be stable under ambient atmosphere which provides an important basis for technological applications like templating and coating. The previously suggested (12 × 12) periodicity of this reconstruction has been unambiguously confirmed and structural

features are discussed in the light of the x-ray diffraction results.

Reprinted with kind permission from Elsevier.

[a] Note that you need a subscription for this journal to directly access the article.

Available online at www.sciencedirect.com

ScienceDirect

Surface Science 601 (2007) L7–L10

SURFACE SCIENCE

www.elsevier.com/locate/susc

Surface Science Letters

# Surface X-ray diffraction study of boron-nitride nanomesh in air

O. Bunk [a,*], M. Corso [b], D. Martoccia [a], R. Herger [a], P.R. Willmott [a], B.D. Patterson [a], J. Osterwalder [b], J.F. van der Veen [a,c], T. Greber [b]

[a] *Research Department Synchrotron Radiation and Nanotechnology, Paul Scherrer Institut, 5232 Villigen PSI, Switzerland*
[b] *Physik-Institut, Universität Zürich, 8057 Zürich, Switzerland*
[c] *ETH Zurich, 8093 Zürich, Switzerland*

Received 3 October 2006; accepted for publication 13 November 2006

---

## Abstract

The hexagonal boron-nitride 'nanomesh' surface reconstruction on Rh(1 1 1) [Corso et al., Science 303 (2004) 217–220] has been investigated using surface X-ray diffraction utilizing synchrotron radiation. This unique structure has been found to be stable under ambient atmosphere which provides an important basis for technological applications like templating and coating. The previously suggested (12 × 12) periodicity of this reconstruction has been unambiguously confirmed and structural features are discussed in the light of the X-ray diffraction results.

*Keywords:* Surface X-ray diffraction; Boron-nitride; Rhodium; Nanomesh

---

## 1. Introduction

At elevated temperatures borazine decomposes on Rh(1 1 1) to form a self assembled surface reconstruction of thermally very stable hexagonal boron-nitride (h-BN) [1]. The unit cell of this highly regular structure is, at 32 Å, huge by surface science standards. The detailed geometry of this 'nanomesh' is still under debate but major efforts are being taken to further investigate and utilize this unique system. This is attested, for example, by the formation of a specific targeted research project 'NanoMesh' supported within the sixth framework program (FP6) of the European Commission, a recent NanoMesh workshop, and the successful use of the nanomesh as template for the ordering of fullerenes [1].

Related but different structures of hexagonal boron-nitride have been reported for other surfaces like for example Ru(0 0 0 1), Pt(1 1 1) [2,3], Cu(1 1 1), Ni(1 1 1) [4] and Pd(1 1 0) [5]. From a fundamental and an applied point of view is it important to disentangle the delicate balance in the surface free energy between h-BN and substrate contributions and the processes that lead to the formation of this fascinating structure and related structures on other substrates. For applications, it is mandatory to have detailed knowledge of the atomic and electronic structure of the surface for utilizing it as an oxygen- and carbon-free template, e.g., for the production of nanocatalysts and nanomagnets.

To solve the structure of a reconstruction involving several hundred atoms the best technique currently applicable is surface X-ray diffraction (SXRD) [6–8]. X-rays easily penetrate the surface and are therefore sensitive to the structure of an extended surface region rather than only the topmost layer. The data can be analyzed within the kinematical framework and this facilitates solving such large reconstructions. However, due to the low scattering cross-sections of boron and nitrogen, is it necessary to perform such an experiment at a 3rd-generation synchrotron source.

With applications like templating and ordering of liquids in mind, we studied the nanomesh structure on

---

[*] Corresponding author. Tel.: +41 563103077.
*E-mail address:* oliver.bunk@psi.ch (O. Bunk).

0039-6028/$ - see front matter © 2006 Elsevier B.V. All rights reserved.
doi:10.1016/j.susc.2006.11.018

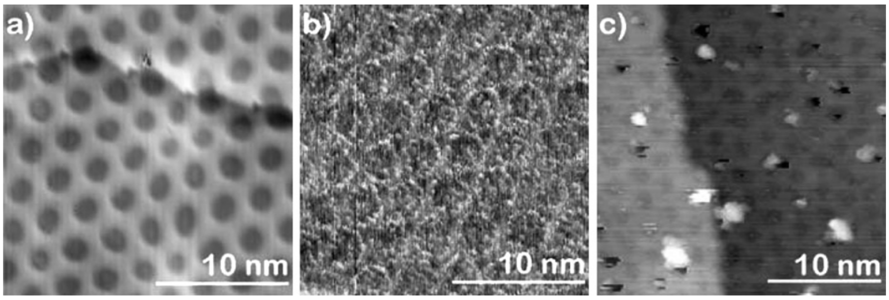

Fig. 1. Constant current STM images measured at $I_t = 1$ nA and $V_s = -1$ V. (a) STM image of the h-BN on Rh(1 1 1) nanomesh taken after preparation in UHV. The nanomesh survived 60 h air exposure as demonstrated by (b) STM and LEED images. (c) A short annealing up to 950 K is enough to remove a relevant part of the contaminants (as $H_2O$, $O_2$, $CO_2$, and CO) from the surface and bring the nanomesh back to its initial (pre-air exposure) configuration.

Rh(1 1 1) under ambient conditions. It turned out that the nanomesh is stable even under these extreme conditions, in contrast to typical surface reconstructions, which normally require ultra-high vacuum to be preserved.

## 2. Experimental

The samples were prepared in an ultra-high vacuum (UHV) system equipped with low energy electron diffraction and a scanning tunneling microscope (STM) [9]. The Rh(1 1 1) surface has been cleaned by repeated sputtering and annealing cycles. The surface was held at 1070 K and exposed to borazine at a pressure of $3 \times 10^{-7}$ mbar, then subsequently cooled down to room temperature.

As a pre-study of the stability of the reconstruction STM investigations have been performed before and after a 60 h air exposure, see Fig. 1.

Freshly prepared samples for the X-ray experiments were transferred to the beamline and mounted under ambient conditions inside a chamber with Kapton windows. The chamber was flushed by a constant overpressure of helium to reduce the background scattering. The X-ray photon energy was set to 15.0 keV and the glancing angle of incidence to 0.20°. A dataset consisting of 816 fractional order and 17 integer order in-plane reflections was recorded. Details about the beamline, the surface diffractometer and the data acquisition using a novel 2D pixel detector can be found elsewhere [10,11].

The integrated intensity of the recorded reflections was determined and the standard geometrical correction factors applied [11]. Averaging reflections which are equivalent due to the p3m symmetry of the substrate yielded 402 fractional and nine integer order reflections. The systematic error determined in this standard averaging procedure [7] was as high as 74%, rendering a quantitative data analysis impossible. Among other things is the use of the stationary geometry without sample rocking scans [12] and scattering from the sample holder responsible for this. Nevertheless, valuable qualitative structural information can be obtained from the SXRD data.

In the following we use the conventional surface coordinate system with $\mathbf{a} = 1/2[1 0 \bar{1}]_{\text{cubic}}, \mathbf{b} = 1/2[\bar{1} 1 0]_{\text{cubic}}$, and $\mathbf{c} = 1/3[1 1 1]_{\text{cubic}}$. The cubic coordinates are in units of the rhodium lattice constant, 3.80 Å at 300 K.

## 3. Results and discussion

One of the main results of our investigations is the stability of the nanomesh reconstruction under ambient atmosphere. As an example, the effect of a 60 h exposure to air is shown in Fig. 1. The basic structural elements can still be recognized after this prolonged exposure. After removing the adsorbates by a short annealing at 950 K, the original structure is restored. This means that this unique surface reconstruction is an ideal candidate for practical applications, such as its use as a template for the production of nanomaterials.

That the nanomesh structure is a commensurate reconstruction with a $(12 \times 12)$ unit cell has been confirmed by in-plane scans along directions of high symmetry. An example is shown in Fig. 2. The (13/12 0) peak of the reconstruction is of course weak but clearly observable and exactly at the expected position.

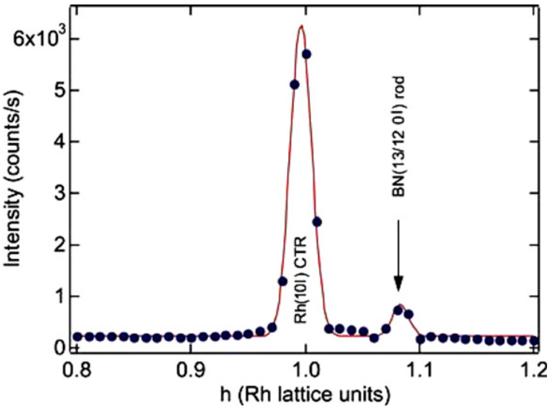

Fig. 2. SXRD intensity profile recorded in the plane of the surface ($l = 0.07$) at constant, $k = 0$. The (1 0 0.07) peak of the Rh(1 1 1) substrate and the (13/12 0 0.07) peak of the nanomesh reconstruction are observed, thereby confirming a commensurate superstructure with a $(12 \times 12)$ Rh(1 1 1) unit cell.

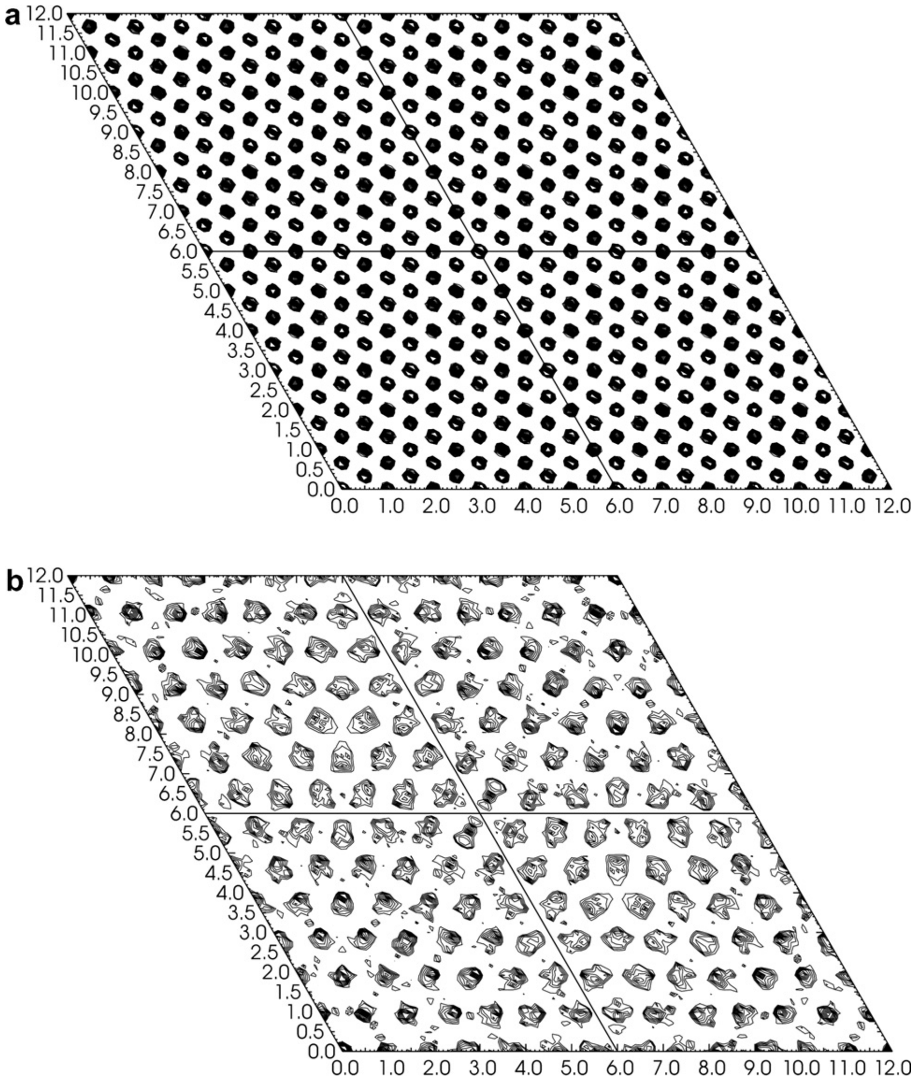

Fig. 3. Patterson functions of h-BN on Rh(1 1 1). Each peak of these contour plots of the Patterson function calculated from the in-plane reflections corresponds to an important interatomic distance projected in the surface plane. (a) The Patterson function calculated from all and (b) only from the fractional order reflections is shown. The observed distances show a clear fingerprint of a (13 × 13) coincidence lattice of h-BN on a (12 × 12) Rh(1 1 1) unit cell.

The Patterson function is the auto correlation function of the electron density. The peaks in the Patterson function correspond to interatomic distances. The projection of this function in the surface plane can be calculated from the near in-plane reflections which have a small momentum transfer perpendicular to the surface [6–8]. A contour plot of this projection is shown in Fig. 3. Taking both integer and fractional order reflections into account, the Patterson function is sensitive to both the bulk-like substrate and the reconstructed surface region. The resulting contour plot is shown in Fig. 3a. The plot is dominated by peaks originating from interatomic distances between bulk Rh atoms since these atoms scatter significantly more than h-BN.[1] A regular mesh of 12 × 12 peaks over the (12 × 12) unit cell is observed.[2]

The Patterson function calculated from the fractional order reflections alone is only sensitive to the reconstructed surface region, i.e., to the h-BN nanomesh and any Rh atoms showing in-plane deviations from their bulk positions, see Fig. 3b. Again a hexagonal structure can be observed but this time with 13 × 13 peaks within the (12 × 12) unit cell. This is a clear fingerprint of the nanomesh, which has been interpreted as a coincidence structure of 13 h-BN per 12 Rh units [1]. The internal structure of the nanomesh cannot be deduced from the Patterson function. However, one more important point can be made: The Rh substrate

---

[1] Rh has $Z = 45$ electrons compared to $Z = 5$ for B and $Z = 7$ for N, i.e., Rh scatters about $45^2/5^2 = 81$ times stronger than B and ~41 times stronger than $N$.

[2] The shift vector from one to the following bulk Rh layer is $(1/3\,2/3\,-1)$ and the Patterson function is sensitive to the projection of all these layers in the surface plane.

does not exhibit significant relaxations since otherwise the Patterson function calculated from the fractional order reflections, Fig. 3b, would be dominated by the Rh signal in the vicinity of points corrsponding to bulk distances, i.e., peak positions in Fig. 3a. Therefore we can conclude that the adsorbate–substrate interaction is sufficiently strong to yield a commensurate and long-range well-ordered structure but does not induce strong relaxations of the Rh atoms from their bulk-like positions in the surface plane.

## 4. Summary and outlook

We have investigated the nanomesh structure of hexagonal boron-nitride on Rh(1 1 1). This unique surface reconstruction has been found to be stable under prolonged exposure to ambient atmosphere and X-ray radiation. The initially proposed $(12 \times 12)$ unit cell has been confirmed by the SXRD results. As a preliminary result indications have been presented that the nanomesh is a coincidence structure of 13 h-BN units per 12 Rh substrate units and that no major deviations from the in-plane bulk positions occur for the bulk Rh atoms.

A detailed three-dimensional structure determination of the nanomesh structure in UHV is planned to gain a detailed picture of the structure including all atomic positions.

## Acknowledgements

This work was performed at the Swiss Light Source, Paul Scherrer Institut, Villigen, Switzerland. We thank Dominik Meister, Michael Lange and Martin Klöckner for technical support.

## References

[1] M. Corso, W. Auwärter, M. Muntwiler, A. Tamai, T. Greber, J. Osterwalder, Science 303 (2004) 217.

[2] M.T. Paffett, R.J. Simonson, P. Papin, R.T. Paine, Surf. Sci. 232 (1990) 286.

[3] F. Müller, K. Stöwe, H. Sachdev, Chem. Mater. 17 (2005) 3464.

[4] A.B. Preobrajenski, A.S. Vinogradov, N. Mårtensson, Surf. Sci. 582 (2005) 21.

[5] M. Corso, T. Greber, J. Osterwalder, Surf. Sci. 577 (2005) L78.

[6] R. Feidenhans'l, Surf. Sci. Rep. 10 (1989) 105.

[7] I.K. Robinson, Surface crystallography, in: G.S. Brown, D.E. Moncton (Eds.), Handbook on Synchrotron Radiation, vol. 3, North-Holland, Amsterdam, 1991, p. 221 (Chapter 7).

[8] H. Dosch, Critical Phenomena at Surfaces and Interfaces – Evanescent X-ray and Neutron Scattering, Springer, New York, 1992.

[9] W. Auwärter, T.J. Kreutz, T. Greber, J. Osterwalder, Surf. Sci. 429 (1999) 229.

[10] B.D. Patterson, R. Abela, H. Auderset, Q. Chen, F. Fauth, F. Gozzo, G. Ingold, H. Kühne, M. Lange, D. Maden, D. Meister, P. Pattison, T. Schmidt, B. Schmitt, C. Schulze-Briese, M. Shi, M. Stampanoni, P.R. Willmott, Nucl. Instr. Meth. Phys. Res. A 540 (2005) 42.

[11] C.M. Schlepütz, R. Herger, P.R. Willmott, B.D. Patterson, O. Bunk, C. Brönnimann, B. Henrich, G. Hülsen, E.F. Eikenberry, Acta Cryst. A 61 (2005) 418.

[12] E. Vlieg, J. Appl. Cryst. 30 (1997) 532.

## Chapter 6

# *h*-BN on Rh(111): Persistence of a commensurate 13-on-12 superstructure up to high temperatures

The work presented in this chapter has been published in:

D. Martoccia, S.A. Pauli, T. Brugger, T. Greber, B.D. Patterson, P.R. Willmott: "*h*-BN on Rh(111): Persistence of a commensurate 13-on-12 superstructure up to high temperatures." *Surf. Sci.* **604**(5-6), L9-L11 (2010),
doi:10.1016/J.Susc.2009.12.016 [a]

artikel2.pdf is the online version of the library Zentralbibliothek Zürich

### Abstract

We present a high-resolution surface x-ray diffraction study of hexagonal boron nitride (*h*-BN) on the surface of Rh(111). The previously observed commensurate 13-on-12 superstructure for this system is stable in the temperature range between room temperature and 830° C. Surface x-ray diffraction measurements up to 830° C

on the superstructure show no sign of a shift towards a different superstructure, demonstrating the high thermal stability and strong bonding between film and substrate. At lower temperatures, an anomalous thermal expansion behaviour of the topmost surface region of rhodium is observed, where the rhodium in-plane lattice constant remains invariant. This can be explained by the *h*-BN single-layer being compressively strained, whereby the strong bonding to the substrate causes the latter to be tensile strained.

Reprinted with kind permission from Elsevier.

[a] Note that you need a subscription for this journal to directly access the article.

Surface Science 604 (2010) L9–L11

Contents lists available at ScienceDirect

Surface Science

journal homepage: www.elsevier.com/locate/susc

Surface Science Letters

# $h$-BN on Rh(1 1 1): Persistence of a commensurate 13-on-12 superstructure up to high temperatures

D. Martoccia [a], S.A. Pauli [a], T. Brugger [b], T. Greber [b], B.D. Patterson [a], P.R. Willmott [a,*]

[a] *Swiss Light Source, Paul Scherrer Institut, CH-5232 Villigen, Switzerland*
[b] *Institute of Physics, University of Zürich, Winterthurerstrasse 190, CH-8057 Zürich, Switzerland*

ARTICLE INFO

*Article history:*
Received 4 November 2009
Accepted for publication 16 December 2009
Available online 29 December 2009

*Keywords:*
Boron nitride
Rh(1 1 1)
Surface X-ray diffraction
Superstructure
Nanomesh
Low-energy electron-diffraction
Ultraviolet photoelectron spectroscopy
Scanning tunneling microscopy

ABSTRACT

We present a high-resolution surface X-ray diffraction study of hexagonal boron nitride ($h$-BN) on the surface of Rh(1 1 1). The previously observed commensurate 13-on-12 superstructure for this system is stable in the temperature range between room temperature and 830 °C. Surface X-ray diffraction measurements up to 830 °C on the superstructure show no sign of a shift towards a different superstructure, demonstrating the high thermal stability and strong bonding between film and substrate. At lower temperatures, an anomalous thermal expansion behaviour of the topmost surface region of rhodium is observed, where the rhodium in-plane lattice constant remains invariant. This can be explained by the ($h$-BN) single-layer being compressively strained, whereby the strong bonding to the substrate causes the latter to be tensile strained.

## 1. Introduction

The technological goal of engineering template structures on the scale of a few nanometers for the purpose of creating regular two-dimensional arrays of molecules has important potential applications, e.g., in molecular recognition [1]. This task can be addressed by the formation of superstructures, which can act as nanotemplates. The size and stability in different physical environments of the superstructure cell is of fundamental importance. In 2004, a highly regular mesh was found to form when a clean Rh(1 1 1) surface was exposed to borazine, $(HBNH)_3$, at high temperature [2]. This so-called hexagonal boron nitride ($h$-BN) nanomesh has been shown to act as an ideal template for assembling nanoparticles [3] or trapping single molecules [4,1,5].

From low-energy electron-diffraction (LEED) measurements [2] (which show a surface reconstruction), ultraviolet photoelectron spectroscopy (UPS) measurements (which reveal a $\sigma$-band splitting [2]); scanning tunneling microscopy (STM) [3,4,6], and subsequently from density functional theory calculations [7–9], the structural model of the nanomesh has been deduced to be a single corrugated BN layer consisting of hexagonally arranged “high” and “low” regions formed by differences in the chemical bonding strength of the B and N atoms to the Rh atoms underneath. Surface X-ray diffraction (SXRD) experiments confirmed a large unit cell for the ($h$-BN) layer, consisting of (13 × 13) N and (13 × 13) B atoms above a substrate-surface unit cell of (12 × 12) Rh atoms [10] (referred henceforth as 13-on-12). The periodicity of the superstructure is 3.22 nm. Recently it was reported in a LEED study that ($h$-BN) grown on Rh–YSZ–Si(1 1 1), a system better suited for technological applications, exhibits a (14 × 14) ($h$-BN) on (13 × 13) Rh(1 1 1) superstructure [11]. It was argued that the different thermal expansion behaviours of the multilayer substrates and the single crystal substrate is the reason for the formation of the different sized superstructures. Similar structures were also found for ($h$-BN)/Ru(0 0 0 1) [3,12,13] and for graphene/Ru(0 0 0 1) [14–17].

The ($h$-BN)/Rh structure results as a consequence of a balance between repulsive forces acting on N and attractive forces acting on the B atoms. The strength of these forces varies with the lateral BN position relative to the underlying Rh-substrate atoms – the ($h$-BN) monolayer therefore deforms (corrugates) vertically [7,8]. This theoretically predicted, highly corrugated monolayer structure was later confirmed experimentally by STM [4]. Although there are several reports on the growth of this system, the explanations why the reconstruction adopts a 13-on-12 signature are rare [11].

To precisely assess the effect of the commensurate fit of the ($h$-BN) with respect to the substrate we performed high-resolution surface X-ray diffraction (SXRD) measurements. We measured the

---

[*] Corresponding author.
*E-mail address:* philip.willmott@psi.ch (P.R. Willmott).

0039-6028/$ - see front matter © 2009 Elsevier B.V. All rights reserved.
doi:10.1016/j.susc.2009.12.016

dependence of the superstructure lattice constant on the temperature and compared it to expectations from the known thermal expansion coefficients of bulk Rh and (*h*-BN).

## 2. Experimental

The single-crystal Rh(1 1 1) surface was prepared in an ultra-high vacuum (UHV) system equipped with LEED, STM and UPS by the standard preparation method [2,12]. The growth temperature was 750 °C. UPS and LEED measurements after preparation and directly before transfer under UHV to the Materials Science beamline, Swiss Light Source, Paul Scherrer Institut, confirmed the presence of the (*h*-BN) nanomesh.

The nanomesh was investigated by SXRD using a beam energy of 12.398 keV (1.00 Å) by recording six peaks [given in reciprocal lattice units (r.l.u.) of the rhodium bulk] per temperature value, at the $h = 11/12$, $h = 1$, $h = 13/12$ and $h = -11/12$, $h = -1$ and $h = -13/12$ positions, whereby $k = 0$ and $l = 1.2$ remained constant. The angle of the incoming X-rays was fixed to the critical angle, $\alpha_{crit} = 0.315^\circ$ for Rh at this X-ray energy, where the X-ray evanescent wave intensity is strongest, and only penetrates the surface to a depth of a few nanometers. At each peak position a high-resolution scan covering at least a range of ±0.04 r.l.u. was performed. The background was fit with a polynomial function and was subtracted from the measured data. The resulting signal itself was fit using a pseudo-Voigt function. At each new temperature, enough time was allowed to ensure thermal equilibration (which was especially important at lower temperatures) before the sample was carefully realigned and crystallographically oriented. The integer Bragg-rod positions of the Rh-substrate were used to determine the substrate lattice constant. Previous temperature calibrations of the substrate heater ensured the accuracy of the temperature to better than ±20 °C.

## 3. Results and discussion

First we confirmed the 13-on-12 reconstruction of the (*h*-BN)/Rh(1 1 1)-system at room temperature (see Fig. 1). Importantly, in addition to the (10)-Rh-peak and the 13/12 principal (*h*-BN)-peak, we observe the 11/12 peak. We call this the “real reconstruction” peak – since SXRD is not affected by multiple scattering (it satisfies to a high degree of accuracy the kinematical approximation), this peak can only arise if the system exhibits a true commensurate superstructure, which in this case is due to a corrugation over 12 × 12 Rh-atoms. Such a signal would not be observed in a simple Moiré structure resulting from the coincidental overlay of a flat (*h*-BN) monolayer on a flat Rh-substrate. This peak is still observed at 780 °C, a sign that even at these high temperatures, the commensurate superstructure remains well defined.

The temperature-dependent in-plane lattice constant of bulk rhodium, $a_{Rh}$ [18], and bulk (*h*-BN) [19] given in Angstrom are:

$$a_{Rh} = 3.8026/\sqrt{2} + 29.27\times10^{-6}\cdot T + 10.49\times10^{-9}\cdot T^2 + 0.54\times10^{-12}\cdot T^3 \quad (1)$$

$$a_{h-BN} = 2.504 - 7.42\times10^{-6}\cdot(T-25) + 4.79\times10^{-9}(T-25), \quad (2)$$

with the temperature $T$ given in °C. However, in this system comprising of only a single monolayer of (*h*-BN) it is possible that the in-plane lattice constant may deviates significantly in its temperature dependence from that of bulk (*h*-BN). There is no literature on the lattice constant of free-floating (*h*-BN) monolayers, so we assume here that it follows a similar temperature dependence to the bulk lattice constant.

The measured in-plane Rh-lattice constant at room temperature is 2.689 Å, in agreement with the literature [18]. However, we should view this value with some caution. The controlling diffractometer software (SPEC) fits the lattice parameters $a$, $b$, $c$, $\alpha$, $\beta$, and $\gamma$. After careful analysis of these values as a function of temperature, we estimate that the systematic errors for the lattice constants are ±0.01 Å. The statistical errors are at least an order of magnitude smaller.

In Fig. 2a we compare the expected lattice expansion (blue solid line) [see Eq. (1)] for the bulk rhodium with the measured lattice expansion (blue line with circles) of the topmost Rh surface region between room temperature and 830 °C. As explained above, the absolute measured lattice constant of the rhodium at room temperature is associated with a systematic error of ±0.01 Å, however the shape of the curve is reliable. Hence the boundaries of possible vertical displacement of the measured lattice constant of rhodium are given by the grey band.

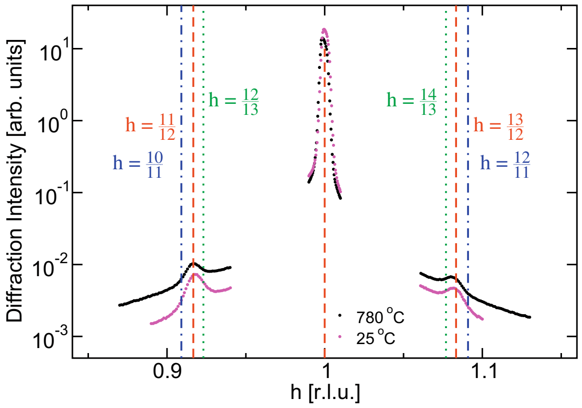

**Fig. 1.** Raw data for scans along $h$ at $l = 1.2$, $k = 0$ r.l.u. measured at two different temperatures, 25 °C (black) and for 780 °C (magenta). The real reconstruction peak and the principal (*h*-BN) peak both unambiguously confirm a 13-on-12 commensurate superstructure (indicated by the red dashed line) at both temperatures. The 13-on-12 superstructure is unambiguous and well defined, as the peak-width is smaller than the separation between the $h = 13/12$ and the $h = 14/13$ positions (green dotted line) or between $h = 12/11$ (blue dash-dotted) and $h = 13/12$. Note that only the background increases with higher temperatures, the signals differ by less than 10% in peak height and integrated intensity.

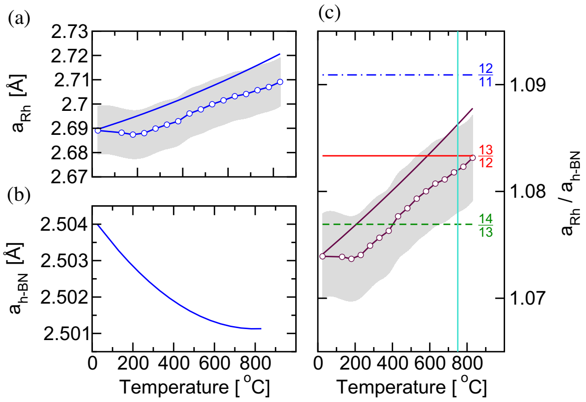

**Fig. 2.** (a) The temperature-dependent in-plane rhodium lattice constant, expected (solid blue line with grey error band) and measured (blue line with circles). (b) The expected (*h*-BN) lattice expansion as given in [19]. (c) The ratio of the plots given in Fig. 2a and b. At the growth temperature of 750 °C (vertical solid line) a 13-on-12 superstructure is expected, whereas at room temperature a 14-on-13 would seem more favourable. (For interpretation of the references to colour in this figure legend, the reader is referred to the web version of this article.)

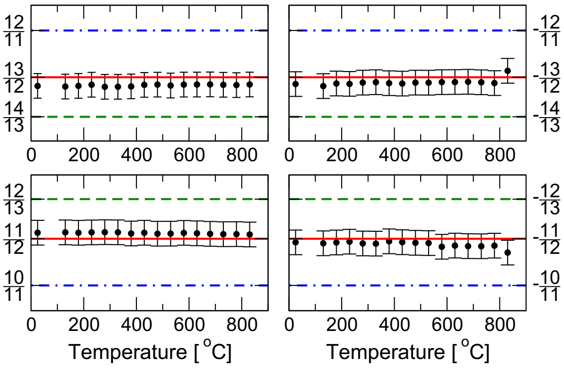

**Fig. 3.** Temperature dependence of the four superstructure peaks 13/12, −13/12, 11/12, and −11/12 r.l.u. The reconstruction remains stable even up to above 780 °C. This proves that the reconstruction is commensurate and that 13 × 13 BN in fact lock-in to 12 × 12 Rh-atoms. A 14-on-13 superstructure was never observed.

A plot of the temperature dependent lattice expansion of bulk (*h*-BN) given in Eq. (2) is shown in Fig. 2b. Note that the bulk rhodium lattice expands with temperature, whereas the (*h*-BN) exhibits a contraction up to 774 °C, and a dilation higher in temperature. In Fig. 2c we show the ratio of the plots shown in Fig. 2a and b. The ratio of the measured rhodium lattice expansion and the expected (*h*-BN) contraction between approximately 200 °C and the highest measured temperature of 830 °C has the same gradient as the predicted curve and therefore follows the expected behaviour given by Eqs. (1) and (2). Note, however, that between room temperature and 200 °C the experimental data disagrees with the predicted curve insofar that the in-plane rhodium lattice constant remains constant over this temperature range. From Fig. 2c, one can see that at the growth temperature of 750 °C the superstructure closest to both the predicted and experimentally determined lattice constant ratios is 13-on-12, whereas at room temperature a 14-on-13 would appear to be more likely.

The size of the measured superstructure as a function of the temperature is shown in Fig. 3. At all temperatures up to 780 °C the peaks were found to match a 13-on-12 superstructure within their experimental uncertainty. The errors associated with the peak positions were calculated from the standard deviation of the recorded positions and the error estimated from the pseudo-Voigt fit to the signal and found to be $\sigma = \pm 0.002$ r.l.u. No indication of a drift towards a 14-on-13 superstructure could be established, even at room temperature. This can be only explained by the fact that the (*h*-BN) layer is locked in with the rhodium atoms due to strong lock-in to the substrate, seen also by Preobrajenski et al. [20]. We know that the lock-in energy of the corrugated system is lower than the absorption energy [9], but larger than the strain energy. This latter is difficult to quantify for our corrugated system, but we can set a lower limit to this for a flat (*h*-BN) layer, which we have calculated to be 0.3 eV per superstructure cell. Corrugation will of course increase this value substantially.

As the temperature was raised from 780 °C to 830 °C, the (*h*-BN) superstructure and real reconstruction peaks started to irreversibly vanish, presumably due to thermal degradation. This caused the diffraction peak intensities of the last temperature measurement to be lower, although all the peaks still matched a 13-on-12 reconstruction. We propose that the anomalous lattice expansion behaviour of the rhodium seen in Fig. 2 up to 200 °C is explained as follows: when grown, the (*h*-BN) forms a commensurate superstructure, evident from the real reconstruction peak at 11/12 r.l.u. At this temperature, 750 °C, the lattice constants of rhodium and (*h*-BN) favour a 13-on-12 superstructure (see Fig. 2c). During subsequent cooling, the strong bonding of the (*h*-BN) to the Rh-substrate prohibits a change of the superstructure registry to 14-on-13, although this would be more relaxed for the (*h*-BN) as well as for the rhodium surface. The (*h*-BN) becomes more and more compressively strained, and at approximately 200 °C, this force is strong enough to hinder the upper region of the rhodium from further contraction, causing this latter to become tensile strained.

## 4. Summary and conclusions

In this report we have investigated the (*h*-BN)/Rh(1 1 1) structure as a function of temperature. The 13-on-12 superstructure is confirmed. The existence of a reconstruction peak at 11/12 r.l.u. proves that the system is a real commensurate superstructure caused by corrugation and not merely a flat Moiré pattern. The structure is remarkably thermally stable, with the 13-on-12 reconstruction peaks remaining clearly visible up to 830 °C.

Calculations based on the thermal expansion coefficients of (*h*-BN) and Rh lead to the conclusion that the superstructure is formed at the growth temperature. Moreover, it is proposed that the observation of a hindered thermal expansion of the topmost rhodium surface layers below 200 °C is caused by strain coupling from the increasingly compressively strained (*h*-BN) layer as the system is cooled to the upper region of the Rh-substrate, which in turn becomes tensile strained.

## Acknowledgements

This work was partly performed at the Swiss Light Source, Paul Scherrer Institut, Villigen, Switzerland. We thank Dominik Meister, Michael Lange and Martin Klöckner for technical support. Support of this work by the Schweizerischer Nationalfond zur Förderung der wissenschaftlichen Forschung is gratefully acknowledged.

## References

[1] H. Dil, J. Lobo-Checa, R. Laskowski, P. Blaha, S. Berner, J. Osterwalder, T. Greber, Science 319 (2008) 1824.
[2] M. Corso, W. Auwärter, M. Muntwiler, A. Tamai, T. Greber, J. Osterwalder, Science 303 (2004) 217.
[3] A. Goriachko, A.A. Zakharov, H. Over, J. Phys. Chem. C 112 (2008) 10423.
[4] S. Berner, M. Corso, R. Widmer, O. Groening, R. Laskowski, P. Blaha, K. Schwarz, A. Goriachko, H. Over, S. Gsell, et al., Angew. Chem. Int. Ed. 46 (2007) 5115.
[5] A. Goriachko, H. Over, Z. Phys. Chem. 223 (2009) 157.
[6] A.B. Preobrajenski, A.S. Vinogradov, M.L. Ng, E. Ćavar, R. Westerström, A. Mikkelsen, E. Lundgren, N. Mårtensson, Phys. Rev. B 75 (2007) 245412.
[7] R. Laskowski, P. Blaha, T. Gallauner, K. Schwarz, Phys. Rev. Lett. 98 (2007) 106802.
[8] R. Laskowski, P. Blaha, J. Phys. Condens. Matter 20 (2008) 064207.
[9] R. Laskowski, P. Blaha, K. Schwarz, Phys. Rev. B 78 (2008) 045409.
[10] O. Bunk, M. Corso, D. Martoccia, R. Herger, P.R. Willmott, B.D. Patterson, J. Osterwalder, J.F. van der Veen, T. Greber, Surf. Sci. 601 (2007) L7.
[11] F. Müller, S. Hüfner, H. Sachdev, Surf. Sci. 603 (2009) 425.
[12] A. Goriachko, Y. He, M. Knapp, H. Over, Langmuir 23 (2007) 2928.
[13] M.T. Paffett, R.J. Simonson, P. Papin, R.T. Paine, Surf. Sci. 232 (1990) 286.
[14] J.T. Grant, T.W. Haas, Surf. Sci. 21 (1970) 76.
[15] M.C. Wu, Q. Xu, D.W. Goodman, J. Phys. Chem. 98 (1994) 5104.
[16] S. Marchini, S. Günther, J. Wintterlin, Phys. Rev. B 76 (2007) 075429.
[17] D. Martoccia, P.R. Willmott, T. Brugger, M. Björck, S. Günther, C.M. Schlepütz, A. Cervellino, S.A. Pauli, B.D. Patterson, S. Marchini, J. Wintterlin, W. Moritz, et al., Phys. Rev. Lett. 101 (2008) 126102.
[18] H.P. Singh, Acta Crystallogr. A 24 (1968) 469.
[19] R.S. Pease, Acta Crystallogr. 5 (1952) 356.
[20] A.B. Preobrajenski, M.A. Nesterov, M.L. Ng, A.S. Vinogradov, N. Mårtensson, Chem. Phys. Lett. 446 (2007) 119.

# Chapter 7

# *h*-BN on Ru(0001) nanomesh: A 14-on-13 superstructure with 3.5 nm periodicity

The work presented in this chapter has been published in:

D. Martoccia, T. Brugger, M. Björck, C.M. Schlepütz, S.A. Pauli, B.D. Patterson, T. Greber, and P.R. Willmott: "*h*-BN on Ru(0001) nanomesh: A 14-on-13 superstructure with 3.5 nm periodicity" *Surf. Sci.* **604**(5-6), L16-L19 (2010), doi:10.1016/J.Susc.2010.01.003 [a]

artikel3.pdf is the online version of the library Zentralbibliothek Zürich

## Abstract

The structure of epitaxially grown hexagonal boron nitride (*h*-BN) on the surface of a Ru(0001) single crystal was investigated using surface x-ray diffraction, which clearly showed the system to form a commensurate 14-on-13 superstructure. This result disagrees with previous reports on superstructures of the same system and

arguments based on simple thermal expansion coefficient calculations. We argue here that the larger observed superstructure forms because the stronger bonding of $h$-BN/Ru in comparison to $h$-BN/Rh(111) can accommodate the induced lateral in-plane strain- or *lock-in* energy over larger regions (referred to as the *holes*) within the superstructure, which itself can consequently become larger.

Reprinted with kind permission from Elsevier.

[a] Note that you need a subscription for this journal to directly access the article.

Surface Science 604 (2010) L16–L19

Contents lists available at ScienceDirect

Surface Science

journal homepage: www.elsevier.com/locate/susc

Surface Science Letters

# $h$-BN/Ru(0001) nanomesh: A 14-on-13 superstructure with 3.5 nm periodicity

D. Martoccia [a], T. Brugger [b], M. Björck [a,1], C.M. Schlepütz [a,2], S.A. Pauli [a], T. Greber [b], B.D. Patterson [a], P.R. Willmott [a,*]

[a] Swiss Light Source, Paul Scherrer Institute, CH-5232 Villigen, Switzerland
[b] Institut of Physics, University of Zürich, Winterthurerstrasse 190, CH-8057 Zürich, Switzerland

ARTICLE INFO

*Article history:*
Received 4 November 2009
Accepted for publication 7 January 2010
Available online 14 January 2010

*Keywords:*
Boron nitride
Ru(0001)
Surface X-ray diffraction
Superstructure
Nanomesh

ABSTRACT

The structure of epitaxially grown hexagonal boron nitride ($h$-BN) on the surface of a Ru(0001) single crystal was investigated using surface X-ray diffraction, which showed the system to form a commensurate 14-on-13 superstructure. This result disagrees with previous reports on superstructures of the same system and arguments based on simple thermal expansion coefficient calculations. We argue that the larger observed superstructure forms because of the strong bonding of $h$-BN to Ru. In comparison to $h$-BN/Rh(111) it can accommodate more induced lateral in-plane strain- or *lock-in* energy over larger regions (referred to as the *holes*) within the superstructure, which itself can consequently become larger.

## 1. Introduction

The formation of large superstructures on the scale of a few nanometers, which act as nanotemplates [1] has great potential in future applications [2]. Ideally, such templates should remain stable and inert in air and up to high temperatures [3,4].

Borazine, $(HBNH)_3$, deposited on a transition metal surface at high temperatures decomposes and forms a single-layer $h$-BN [5]. Depending on the lattice mismatch to the transition metal substrate, the $h$-BN can be either flat, or form a corrugated nanomesh structure consisting of weaker bound regions, the *wires*, and stronger bound regions, the so-called *holes*. It has been shown that the formation of $h$-BN on 3$d$- and 5$d$- metals, like Ni(111) [6–9] and Pt(111) [10], leads to flat layers, which are weakly bound to the metal substrates. Also, on 4$d$-metals, the bond strength increases with the unoccupied states in the $d$-shell of the substrate [11,12]. Bonding is weaker for growth on Pd(111) [13], and stronger on Rh(111) [14] and Ru(0001) [15]. This, together with the lattice mismatch to Rh(111) and Ru(0001), results in the formation of a nanomesh, first observed by Corso et al. [14] on $h$-BN/Rh(111). The reported commensurate 13-on-12 structure was later confirmed by surface X-ray diffraction (SXRD) measurements [3,16]. In 2007, the formation of a nanomesh for $h$-BN on Ru(0001) was reported [15]. The periodicity of 13-on-12, as originally proposed by Paffett et al. [5], was considered to be the most likely.

In a recent study, $h$-BN was deposited on thin Rh(111)-films grown on yttrium stabilized zirconia on Si(111) [17]. A 14-on-13 structure was reported. It was argued that the slightly smaller lattice constant of the Rh-film compared to bulk Rh(111) and the slightly different thermal expansion coefficients are responsible for the formation of this larger superstructure. Extrapolating this line of argument to a Ru(0001) single crystal, it was predicted that either a 12-on-11 or a 13-on-12 nanomesh superstructure would be formed at the growth temperature of 900 K. Note that the difference in the linear dimensions of the hexagons of the $h$-BN between a 13-on-12 and a 12-on-11 structure is less than 2 pm, or 0.76 % of the unit cell size.

In order to resolve the question of the size of the $h$-BN/Ru(0001)superstructure we have performed high-resolution SXRD measurements. SXRD is uniquely capable of determining lattice constants of surface structures with picometer resolution [3,4,16,18].

## 2. Experimental

The Ru(0001) single crystal was prepared by several sputtering and annealing cycles. For the growth of the $h$-BN layer the crystal was heated to 1030 K in ultrahigh vacuum (UHV), and a single layer of $h$-BN was deposited by dosing borazine at a pressure of $6 \times 10^{-7}$ mbar for 180 s. After the growth this temperature was held for another 60 s, after which, the crystal was cooled to room temperature over 10 min.

---

* Corresponding author.
*E-mail address:* philip.willmott@psi.ch (P.R. Willmott).

[1] Present address: MAX-lab, P.O. Box 118, SE-22100 Lund, Sweden.

[2] Present address: Physics Department, University of Michigan, Ann Arbor, MI 48109-1120, USA.

0039-6028/$ - see front matter © 2010 Elsevier B.V. All rights reserved.
doi:10.1016/j.susc.2010.01.003

The resulting structure was studied in situ by low-energy electron-diffraction (LEED) (Fig. 1). The LEED-image taken at an energy of 74.0 eV after the growth process shows clear satellite spots around the Ru Bragg-rod, demonstrating a well-ordered superstructure. The Ru Bragg-rod, labelled *Ru* in the figure, is henceforth referred to as the *Ru-peak*. The *h*-BN Bragg-rod, which we henceforth refer to as the *principal h-BN-peak*, is labelled *h-BN*, and at 74.0 eV it is the strongest LEED signal. In addition, several other signals in a hexagonal arrangement can be identified. We call these the *real reconstruction peaks* for reasons that will become evident below. An example of such a real reconstruction peak is labelled *rr* in Fig. 1.

Before we proceed, it is important to note that the weak elastic-scattering cross-section of X-ray photons with electrons means that SXRD very well satisfies the kinematical approximation of single scattering events. The low-energy electrons used in LEED, on the other hand, undergo multiple scattering and produce dynamical diffraction. One consequence of this is that while in SXRD real reconstruction peaks appear only for true commensurate superstructures, similar signals at the same positions can arise in LEED even for incommensurate overlayers. An example might be a flat structure with in-plane lattice constants marginally different from those of the substrate, which results in a flat moiré structure. Hence, from the LEED pattern of Fig. 1 alone, we are unable to state with confidence whether *h*-BN on Ru(0001) produces such a flat moiré structure or a true commensurate superstructure. SXRD can resolve this uncertainty.

The valence bands of *h*-BN/Ru(0001) recorded by ultraviolet photoelectron spectroscopy (Fig. 2) indicates splitting of the $\sigma$- and $\pi$-bands, both of which are due to a corrugation and consequent heterogeneous local environment (hole and wire regions) of the B and N atoms [15], the $\sigma_\alpha$ and $\pi_\alpha$ peaks refer to the more weakly bound wires of the corrugation, whereas the $\sigma_\beta$ and $\pi_\beta$ peaks are associated with the stronger bound holes.

The sample was prepared at the University of Zurich and was transferred inside a UHV-baby chamber ($10^{-9}$ mbar) equipped with a hemispherical Be-dome. After the chamber was mounted on the surface diffractometer of the Materials Science beamline, Swiss Light Source, the nanomesh was investigated by SXRD using a beam energy of 12.398 keV (1.00 Å). The incident angle was 0.3°, close to the critical angle, thereby enhancing the surface sensitivity. The structure factors were recorded using the PILATUS 100 k pixel detector and the data were extracted and corrected using standard procedures, described elsewhere [19–21].

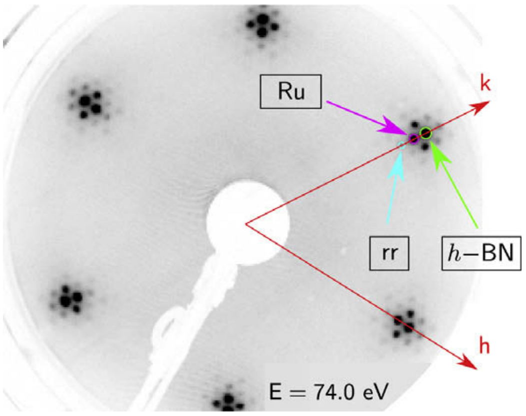

**Fig. 1.** LEED pattern of *h*-BN/Ru(0001) taken at an energy $E = 74.0$ eV. The reciprocal lattice vectors *h* and *k* are indicated in red. Hexagonally arranged satellite spots (one of which is labelled *rr*) can be seen around the Ru-peak, labelled *Ru*. The principal *h*-BN-peak is labelled *h-BN*. (For interpretation of the references to colour in this figure legend, the reader is referred to the web version of this article.)

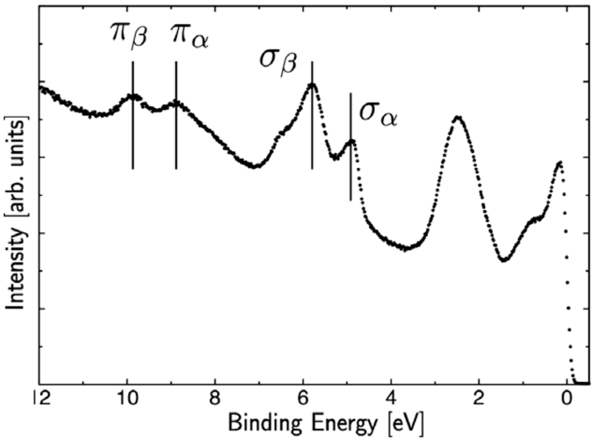

**Fig. 2.** He I$\alpha$ ($h\nu = 21.2$ eV) normal emission photoemission spectrum of *h*-BN/Ru(0001). The $\sigma$- and $\pi$-band splitting of about 1 eV originate from a corrugated single-layer *h*-BN; $\sigma_\alpha$ and $\pi_\alpha$ refer to the wires, $\sigma_\beta$ and $\pi_\beta$ to the holes, which are more strongly bound.

A total of 18 scans were recorded, consisting of three peaks (one real reconstruction peak, the Ru-peak and the *h*-BN-peak) for each of the six high-symmetry directions, namely the $\{h,k\} = \{1,0\}$. Each of the 18 high-resolution scans covered ±0.04 r.l.u. in the radial directions and were performed at an *l*-value of 0.4 r.l.u.

## 3. Results and discussion

Fig. 3 shows a *k*-scan over the $(h,k) = (0,1)$-Ru-peak. Note that in addition to the Ru-peak, we observe the principal *h*-BN-peak and the real reconstruction peak. Representative scans are shown in Fig. 4. It can be seen that they lie at the positions $(h,k) = (0,14/13)$ and $(h,k) = (0,12/13)$, respectively. The width of both peaks of $6 \times 10^{-3}$ r.l.u. is less than the separation between the superstructures under discussion (12-on-11, 13-on-12, and 14-on-13) and, from the Scherrer equation, the domain size is determined to be of the order of 45 nm or larger. The error associated with the peak positions was calculated from the standard deviation of the 12 peak positions and the error estimated from the pseudo-Voigt fit to the signal, and was found to be $\sigma = 1.4 \times 10^{-3}$ r.l.u. Eleven of the 12 peaks lie within $\pm\sigma$ of the nominal values. Therefore we can unambiguously state that *h*-BN on Ru(0001) grows as 14-on-13, with a superstructure size of 3.5 nm.

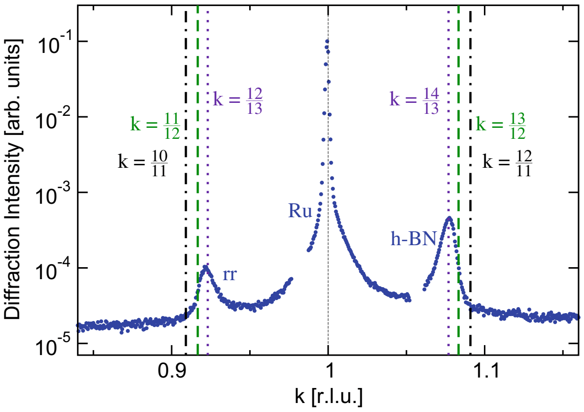

**Fig. 3.** Data of a *k*-scan around the (01)-peak at $l = 0.4$. The real reconstruction peak and the principal *h*-BN peak both unambiguously confirm a 14-on-13 superstructure. The appearance of a $k = 12/13$-peak shows that the unit cell of 13 Ru-atoms is well defined, most probably by a corrugation over this same period.

This result of a 14-on-13 superstructure is in disagreement with previous LEED studies on the same system [5,15,22] and also contradicts interpolation of data predicting a 13-on-12 or a 12-on-11 superstructure on this same system [17]. Using the thermal expansion coefficients for *h*-BN-bulk [23] and Ru-bulk [24] one would indeed expect the superstructure with the lowest in-plane strain at the growth temperature of 1030 K to be 13-on-12. On the other hand, at room temperature, one would expect the superstructure with the lowest in-plane strain to be 14-on-13. We have argued in another study [16] detailing temperature-dependent measurements on *h*-BN/Rh(1 1 1) that film and substrate lock in at the growth temperature and the strong bonding between film and substrate causes this superstructure to remain intact even after cooling to room-temperature. Interestingly, in the system presented here, where bonding between the *h*-BN and the Ru(0 0 0 1) surface is thought to be even stronger than that between *h*-BN and Rh(1 1 1) [12], this argument fails – the observed 14-on-13 superstructure does not agree with that expected at the growth temperature. Even when we use the thermal expansion behaviour for Ru as given in [25], where an anisotropic thermal expansion of ruthenium is observed, the result remains the same.

The formation of the 14-on-13 structure may be related to the less perfect long range order of *h*-BN/Ru(0 0 0 1) [15] compared to *h*-BN/Rh(1 1 1), though potential mechanisms for this remain obscure. Another more interesting possibility is that the formation of the 14-on-13 superstructure might be related to the theoretically predicted higher BN bond energy to Ru compared to that to Rh [12] and the consequently larger lock-in energy. The lock-in energy depends on the BN position with respect to the substrate atoms and is largest for N on top of a substrate atom. It is expected to be proportional to the bond energy to the substrate and is responsible for the formation of corrugated superstructures i.e., to the formation of a dislocation network with regions of tensile strained *h*-BN, in the holes, where BN is strongly bound to the substrate. This produces the opposite effect for the substrate atoms, which undergo lateral compressive strain in these strong bonding regions. The size of the holes depends on the lattice mismatch and the bonding strength [26]. As we propose here, it is the lock-in energy that allows a stronger bonding to the substrate, hence the formation of larger holes *and* a 16% larger superstructure. This offers an explanation for the formation of a larger unit cell in the case of *h*-BN/Ru(0 0 0 1) compared to *h*-BN/Rh(1 1 1), whereby a larger BN lock-in energy is expected to induce the formation of a superstructure that is larger than that expected from the lattice mismatch at the growth temperature. At the growth temperature, the ideal match of *h*-BN on the Ru surface would be a 12.7-on-11.7 structure. The strain energy associated with stretching from a 13-on-12 h-BN on Rh to a commensurate 1-on-1 structure has been calculated by Laskowski et al. [27] to be 0.5 eV per BN unit. Using the corresponding elastic constant, the energy needed for straining the *h*-BN lattice from an ideal match of 12.7 BN on 11.7 Ru cells to the observed 14-on-13 structure is calculated to be 4.3 meV per BN unit. The gain in lock-in energy for the whole superstructure cell must therefore be at least 0.8 eV, since this strain energy is a lower limit for the lock-in energy. Interestingly the calculated binding energy of *h*-BN to Ru, which was determined to be between 0.64 and 0.98 eV per BN unit [27] is of the order of the minimal BN strain energy needed for the 14-on-13 superstructure.

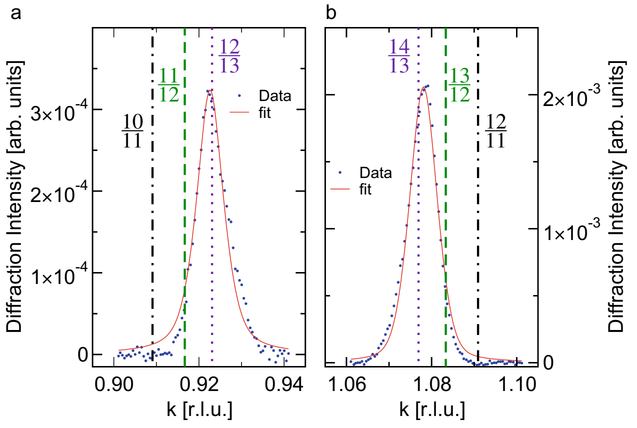

**Fig. 4.** The real reconstruction peak (a) and the principal *h*-BN-peak (b) in units of the experimentally determined Ru-reciprocal lattice unit. The signals were fit using a pseudo-Voigt-function.

## 4. Summary and conclusions

In this report we have investigated the *h*-BN/Ru(0 0 0 1) structure using surface X-ray diffraction. We have shown unambiguously that this is a 14-on-13 superstructure. The observed size of the superstructure contradicts previously reported studies [15,17,22] and cannot be simply explained by the formation of the superstructure at the growth temperature, as expected from the lattice mismatch of bulk materials. We argue that energy minimization from the stronger bonding of *h*-BN to the Ru in comparison to *h*-BN/Rh(1 1 1) overcomes the increased strain energy and leads to the formation of a larger superstructure, 14-on-13 rather than the smaller 13-on-12.

## Acknowledgements

This work was performed at the Swiss Light Source, Paul Scherrer Institut, Villigen, Switzerland. We thank Dominik Meister, Michael Lange and Martin Klöckner for technical support and S. Günther for providing the Ru-crystal. Support of this work by the Schweizerischer Nationalfond zur Förderung der wissenschaftlichen Forschung is gratefully acknowledged.

## References

[1] H. Dil, J. Lobo-Checa, R. Laskowski, P. Blaha, S. Berner, J. Osterwalder, T. Greber, Science 319 (2008) 1824.
[2] A. Goriachko, H. Over, Z. Phys. Chem. 223 (2009) 157.
[3] O. Bunk, M. Corso, D. Martoccia, R. Herger, P.R. Willmott, B.D. Patterson, J. Osterwalder, J.F. van der Veen, T. Greber, Surf. Sci. 601 (2007) L7.
[4] D. Martoccia, M. Björck, C.M. Schlepütz, T. Brugger, S.A. Pauli, B.D. Patterson, T. Greber, P.R. Willmott, 2009. <http://arXiv:0908.4517v1>.
[5] M.T. Paffett, R.J. Simonson, P. Papin, R.T. Paine, Surf. Sci. 232 (1990) 286.
[6] Y. Gamou, M. Terai, A. Nagashima, C. Oshima, Sci. Rep. RITU 44 (1997) 211.
[7] W. Auwärter, T.J. Kreutz, T. Greber, J. Osterwalder, Surf. Sci. 429 (1999) 229.
[8] G.B. Grad, P. Blaha, K. Schwarz, W. Auwärter, T. Greber, Phys. Rev. B 68 (2003) 085404.
[9] M.N. Huda, L. Kleinman, Phys. Rev. B 74 (2006) 075418.
[10] E. Ćavar, R. Westerström, A. Mikkelsen, E. Lundgren, A.S. Vinogradov, M.L. Ng, A.B. Preobrajenski, A.A. Zakharov, N. Mårtensson, Surf. Sci. 602 (2008) 1722.
[11] R. Laskowski, P. Blaha, J. Phys. Condens. Matter 20 (2008) 064207.
[12] R. Laskowski, P. Blaha, K. Schwarz, Phys. Rev. B 78 (2008) 045409.
[13] M. Morscher, M. Corso, T. Greber, J. Osterwalder, Surf. Sci. 600 (2006) 3280.
[14] M. Corso, W. Auwärter, M. Muntwiler, A. Tamai, T. Greber, J. Osterwalder, Science 303 (2004) 217.
[15] A. Goriachko, Y. He, M. Knapp, H. Over, Langmuir 23 (2007) 2928.
[16] D. Martoccia, S.A. Pauli, T. Brugger, T. Greber, B.D. Patterson, P.R. Willmott, Surf. Sci., in press, doi:10.1016/j.susc.2009.12.016.
[17] F. Müller, S. Hüfner, H. Sachdev, Surf. Sci. 603 (2009) 425.
[18] D. Martoccia, P.R. Willmott, T. Brugger, M. Björck, S. Günther, C.M. Schlepütz, A. Cervellino, S.A. Pauli, B.D. Patterson, S. Marchini, et al., Phys. Rev. Lett. 101 (2008) 126102.
[19] E. Vlieg, J. Appl. Crystallogr. 30 (1997) 532.
[20] C.M. Schlepütz, R. Herger, P.R. Willmott, B.D. Patterson, O. Bunk, C. Brönnimann, B. Henrich, G. Hülsen, E.F. Eikenberry, Acta Crystallogr. Sec. E 61 (2005) 418.
[21] C.M. Schlepütz, Ph.D. thesis, University of Zurich, 2009.
[22] A. Goriachko, A.A. Zakharov, H. Over, J. Phys. Chem. C 112 (2008) 10423.

[23] H.P. Singh, Acta Crystallogr. A 24 (1968) 469.
[24] B. Tryon, T.M. Pollock, M.F.X. Gigliotti, K. Hemker, Scripta Mater. 50 (2004) 845.
[25] Thermophysical Properties of matter, vol. 12, Plenum, New York, 1975.
[26] A.B. Preobrajenski, M.A. Nesterov, M.L. Ng, A.S. Vinogradov, N. Mårtensson, Chem. Phys. Lett. 446 (2007) 119.
[27] R. Laskowski, P. Blaha, T. Gallauner, K. Schwarz, Phys. Rev. Lett. 98 (2007) 106802.

# Chapter 8

# Graphene on Ru(0001): A 25×25 Supercell

The work presented in this chapter has been published in:

D. Martoccia, P.R. Willmott, T. Brugger, M. Björck, S. Günther, C.M. Schlepütz, A. Cervellino, S.A. Pauli, B.D. Patterson, S. Marchini, J. Wintterlin, W. Moritz, and T. Greber "Graphene on Ru(0001): A 25 × 25 supercell." *Phys. Rev. Lett.* **101**(12), 126102 (2008), doi:10.1103/PhysRevLett.101.126102 [a]

artikel4.pdf is the online version of the library Zentralbibliothek Zürich

## Abstract

The structure of a single layer of graphene on Ru(0001) has been studied using surface x-ray diffraction. A surprising superstructure containing 1250 carbon atoms has been determined, whereby $25 \times 25$ graphene unit cells lie on $23 \times 23$ unit cells of Ru. Each supercell contains $2 \times 2$ crystallographically inequivalent subcells caused by corrugation. Strong intensity oscillations in the superstructure rods demonstrate that the Ru substrate is also significantly corrugated down to several monolayers,

and that the bonding between graphene and Ru is strong and cannot be caused by van der Waals bonds. Charge transfer from the Ru substrate to the graphene expands and weakens the C–C bonds, which helps accommodate the in-plane tensile stress. The elucidation of this superstructure provides important information in the potential application of graphene as a template for nanocluster arrays.

Reprinted with kind permission from the American Physical Society.

[a] Note that you need a subscription for this journal to directly access the article.

PRL **101,** 126102 (2008) PHYSICAL REVIEW LETTERS week ending 19 SEPTEMBER 2008

# Graphene on Ru(0001): A 25 × 25 Supercell

D. Martoccia,[1] P. R. Willmott,[1,*] T. Brugger,[2] M. Björck,[1] S. Günther,[3] C. M. Schlepütz,[1] A. Cervellino,[1] S. A. Pauli,[1] B. D. Patterson,[1] S. Marchini,[3] J. Wintterlin,[3] W. Moritz,[4] and T. Greber[2]

[1]*Swiss Light Source, Paul Scherrer Institut, CH-5232 Villigen, Switzerland*
[2]*Institute of Physics, University of Zürich, Winterthurerstrasse 190, CH-8057 Zürich, Switzerland*
[3]*Department of Chemistry, Universität München, D-81377 München, Germany*
[4]*Department of Crystallography, Universität München, D-81377 München, Germany*

(Received 23 July 2008; published 19 September 2008)

The structure of a single layer of graphene on Ru(0001) has been studied using surface x-ray diffraction. A surprising superstructure containing 1250 carbon atoms has been determined, whereby 25 × 25 graphene unit cells lie on 23 × 23 unit cells of Ru. Each supercell contains 2 × 2 crystallographically inequivalent subcells caused by corrugation. Strong intensity oscillations in the superstructure rods demonstrate that the Ru substrate is also significantly corrugated down to several monolayers and that the bonding between graphene and Ru is strong and cannot be caused by van der Waals bonds. Charge transfer from the Ru substrate to the graphene expands and weakens the C–C bonds, which helps accommodate the in-plane tensile stress. The elucidation of this superstructure provides important information in the potential application of graphene as a template for nanocluster arrays.

DOI: 10.1103/PhysRevLett.101.126102 PACS numbers: 68.65.−k, 81.05.Uw, 81.07.Nb

The detailed structure determination of single-layer graphene on well-defined surfaces is a significant goal in materials science and solid-state physics—it is most probable that future electronic devices based on graphene layers will be fabricated on crystalline substrates [1]; hence, knowledge of how substrates affect graphene is of paramount importance if the latter's structural and electronic properties are to be tailored [2]. In addition, it has been recently discovered [3–7] that, when grown on crystalline transition metal surfaces, graphene can form superstructures resulting from moiré superpositions of $(m \times m)$ carbon hexagons on $(n \times n)$ metal surface cells. It is still disputed as to whether observed features within these supercells are caused by electron density fluctuations over a basically flat structure [6] or whether there is an actual buckling of the graphene sheet [3,8,9]. A structural clarification would identify the potential of graphene in applications such as molecular recognition, single-molecule sensing [10], and nanocluster array templates for biological or catalytic applications [11–13]. Here we show, using surface x-ray diffraction (SXRD), that graphene forms a surprising superstructure when grown on Ru(0001), whereby 25 × 25 graphene unit cells lie commensurately on 23 × 23 unit cells of Ru. Characteristic intensity oscillations in the SXRD data prove that not only the graphene but also the Ru down to several atomic layers are significantly corrugated, indicating that the bonding between the single graphene layer and Ru is unusually strong.

The structure of graphene on Ru(0001) has already been investigated using scanning tunneling microscopy (STM), conventional electron microscopy, x-ray photoelectron spectroscopy (XPS), Raman spectroscopy, and low-energy electron diffraction (LEED) and microscopy [3,5–7,9,14], as well as density functional theory (DFT) [8]. Until now, it has remained a contentious issue as to what registry exists between graphene and the underlying Ru substrate. It has been suggested that (12 × 12) graphene hexagons sit on (11 × 11) Ru surface nets (described henceforth as 12-on-11) [3,5,14], while an 11-on-10 structure has also been proposed [6]. If one assumes an in-plane lattice constant for graphene equal to that for graphite (2.4612 Å), the former structure would have an in-plane tensile strain on Ru ($a = 2.706$ Å) of 0.78%, while the latter would be compressively strained by only 0.05%.

The positions of the first-order diffraction signals associated with these two superstructures are 1.100 and 1.0909 in-plane reciprocal lattice units (r.l.u.) of the underlying Ru lattice; i.e., they lie within less than 0.01 r.l.u. of one another. With a conventional LEED system, one can achieve accuracies of only about 1%–2%, excluding an unambiguous identification of the structure using this method. Only surface x-ray diffraction is capable of achieving this goal [15–17].

Two samples of graphene were prepared on separate occasions on the same sputtered and annealed Ru(0001) single crystal. In both cases, the crystal was heated to 1115 K in ultrahigh vacuum (UHV), and a single layer of graphene was deposited by dosing ethene at a pressure of $2 \times 10^{-5}$ Pa for 3 minutes [18]. The temperature was then held at 1115 K for a further 60 seconds. For the first sample, the crystal was then cooled at a rate of 0.4 $\mathrm{K\,s^{-1}}$ down to 915 K and from there at a rate of 0.8 $\mathrm{K\,s^{-1}}$ down to 610 K, after which the heating was turned off. In the case of the second sample, cooling was approximately 4 times quicker. It is noted here that these different cooling rates were chosen to establish whether they affected the final form of the absorbate structure. No significant difference between the two samples could be detected, however.

Typical LEED and STM images after cooling to room temperature are shown in Fig. 1.

The samples were transferred in UHV to a minichamber ($10^{-7}$ Pa) equipped with a hemispherical Be dome for studies using SXRD [19]. The chamber was mounted on the surface diffractometer of the Materials Science beam line, Swiss Light Source [20]. Structure factors were recorded using the Pilatus 100 k pixel detector [21]. The photon energy was 12.4 keV, and the transverse and longitudinal coherence lengths were both 1 $\mu$m.

A calibration of reciprocal space was achieved to two parts in 10 000 by using bulk Ru Bragg reflections as reference points. A typical set of in-plane scans is shown in Figs. 2(b)–2(d). In Fig. 2(b), satellites on either side of the Ru (01) crystal truncation rod (CTR) can be seen. The primary graphene (01) signal [see Fig. 2(d)] at $k = 1.087$ r.l.u. is, in itself, no proof of a commensurate reconstruction, as the graphene could, in principle, lie incommensurately above the Ru substrate. However, the presence also of a signal an equal distance on the other side of the Ru CTR indicates that a reconstruction must exist [Fig. 2(c)]. We found several other signals proving a true reconstruction elsewhere in reciprocal space [see Fig. 2(a)]. Note that the (0001) surface of hexagonal close-packed systems commonly display sixfold symmetry, although the symmetry of a perfect hcp(0001) surface is threefold. This apparent increase in symmetry is caused by surfaces containing regions separated by atomic steps of half a unit cell height, resulting in a 180° rotation of adjacent terraces. This is why only one in-plane axis is shown in Fig. 2(a).

The positions of the two reconstruction signals shown in Figs. 2(c) and 2(d) and those of all of the other superstructure signals investigated indicate, however, that the superstructure complies with neither of those proposed so far. In fact, the signals sit exactly at $21/23$ and $25/23$ r.l.u., to within 0.0002 r.l.u. from which it is unambiguously clear from our SXRD data that the reconstruction is in fact 25-on-23, that is, $25 \times 25$ graphene honeycombs sitting commensurately on $23 \times 23$ Ru unit cells. This signal cannot be explained as originating from the incoherent addition of diffraction signals from large domains of 13-on-12 and 12-on-11 supercells, as the linewidth of the superstructure signal is, at $(5.4 \pm 0.1) \times 10^{-3}$ r.l.u., significantly narrower than the separation of any independent 13-on-12 and 12-on-11 signals of $7.6 \times 10^{-3}$ r.l.u. [see Figs. 2(c) and 2(d)]. Also, a model consisting of a random distribution of 13-on-12 and 12-on-11 supercells differs from that of the 25-on-23 structure by maximum in-plane displacements of the carbon atoms of less than 0.1 Å, which are significantly smaller than typical vibrational amplitudes at room temperature and hence can be ignored.

The supercell, covering over 33 $\text{nm}^2$ and containing 1250 carbon atoms, is shown in the scanning tunneling microscope image in Fig. 1(b). This contains not one but four parallelogram structures. It is still disputed whether the hill-like features are formed by a physical corrugation of the graphene sheet or are caused by electron density waves in an essentially flat graphene layer [6]. Although this cannot be decided from the STM data alone, a recent combined DFT/STM study [8] revealed that the graphene is indeed significantly corrugated when deposited on Ru (0001). It is these features that make this system so interesting as a potential nanotemplate.

The four "subcells" within the supercell cannot map translationally onto one another, as from the SXRD data it is clear that the number of unit cells of Ru (23) as well of graphene (25) along the edges of the supercell are *odd*, and one is therefore forced to conclude that the graphene supercell must consist of four translationally inequivalent subcells. It is noted that, because of the presence of $2 \times 2$ corrugation periods within each supercell, all superstructure peaks with an in-plane distance from the Ru signals of $p/23$ r.l.u., where $p$ is an odd integer, are systematically absent.

The $21/23$ and $25/23$ superstructure rods (SSRs) are shown in Fig. 2(e). Because they provide information only on surface reconstructions of the graphene and uppermost Ru layers, and not on bulk properties, we are able to infer important properties of the surface region immediately from their qualitative features. First, the signal intensity is strongly modulated, with a periodicity of approximately 1.0 r.l.u. (with respect to Ru) in the out-of-plane direction. This modulation can occur only if the ruthenium is physically corrugated, that is, if the graphene imposes vertical

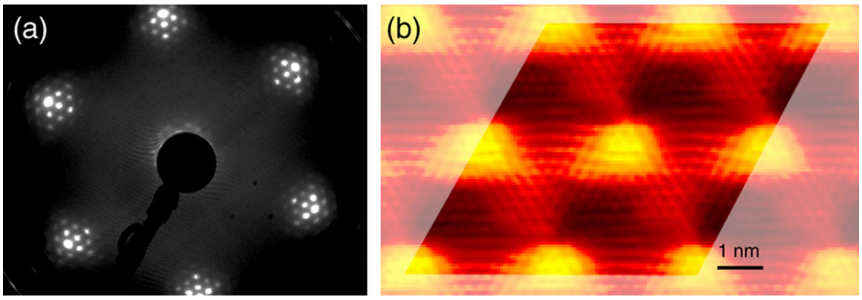

FIG. 1 (color online). (a) A LEED image of the graphene/Ru(0001) surface taken at an electron energy of 74 eV. (b) An STM image of graphene on Ru(0001), highlighting the supercell containing four subcells.

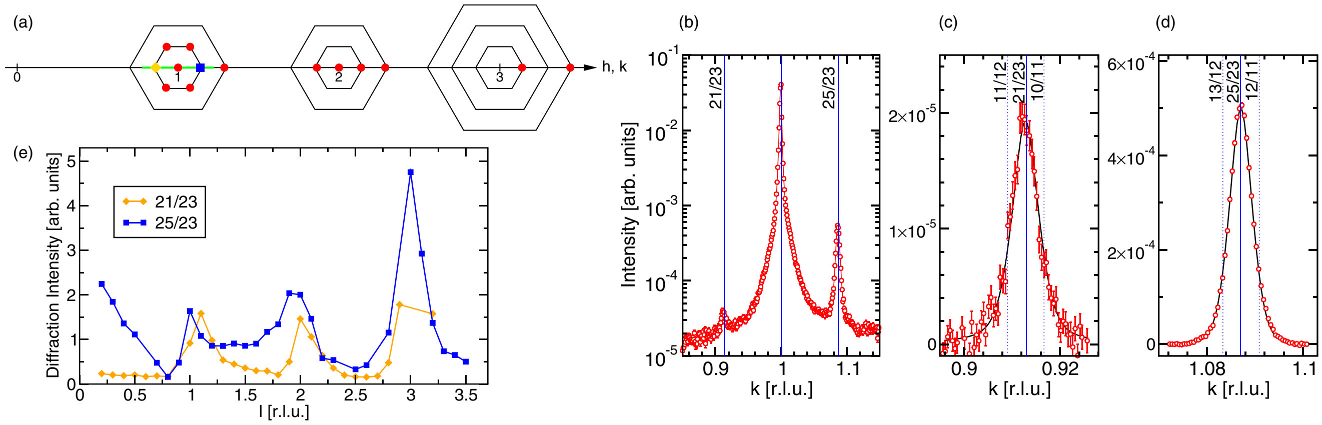

FIG. 2 (color online). Summary of the diffraction data for the graphene/Ru(0001) system. (a) Schematic reciprocal space map showing where data were recorded. The red circular dots indicate points recorded in plane at $l = 0.4$ r.l.u. The in-plane scan along the $k$ direction in the neighborhood of the (01) CTR of Ru at $l = 0.4$ r.l.u. shown in (b) is indicated by the green (gray) line. The positions of superstructure rods shown in (e) are indicated by the orange diamond and blue square. (c),(d) High-resolution scans across the superstructure signal of graphene on Ru, detailing the 25-on-23 reconstruction. The data were fit to a pseudo-Voigt profile (solid black curves), while the positions where 13-on-12 and 12-on-11 reconstruction diffraction signals would lie (dotted lines) are also shown.

strain [8]. Importantly, all of the maxima have widths of approximately 0.25 r.l.u., which means that the Ru substrate must also be significantly corrugated down to about 4 unit cells, or over 1.5 nm.

Unsurprisingly, the 25/23 rod has significant intensity at low $l$ values, as at $l = 0$ this corresponds to the (010) in-plane graphene peak, which is known to have nonzero intensity. However, extrapolation of the 21/23 rod to $l = 0$ strongly indicates that it also has nonzero intensity here, which can occur only if there are in-plane movements of the atoms within the supercell.

In order to estimate the corrugation amplitudes and depths of the ruthenium, we used a simple model to simulate the two superstructure rods of Fig. 2(e). The vertical displacement field of the graphene corrugation [Fig. 3(a)] is generated by first calculating a subfield for each of the two inequivalent carbon atoms in the conventional graphite unit cell, whereby the vertical distance to the Ru substrate is proportional to the in-plane separation from the nearest Ru atom. The component fields are interpolated and then added to produce the final displacement map. The model incorporated only four parameters, namely, the graphene corrugation amplitude and the minimum graphene-Ru distance, for which we used fixed values determined by DFT calculations [8], and the corrugation of the uppermost Ru atomic layer and the exponential decay depth of the Ru corrugation, which were varied to best match the experimental linewidths and intensities. Any in-plane movements of either the graphene or the Ru were ignored, as this would add significant complexity to the model, and our *a priori* knowledge of such movements is very limited. The simulation is shown in Fig. 3. Despite the simplicity of this model, the qualitative agreement is impressive. The peak-to-peak corrugation amplitude of the uppermost ruthenium atomic layer is 0.20 Å, which decays exponentially with depth, with a characteristic length of 1.7 unit cells (3.4 atomic layers). Note that the graphene and ruthenium corrugations were chosen to be in phase (i.e., peak above peak and valley above valley). If the corrugations are made to be out of phase (peak above valley and valley above peak), the agreement with the experimental data is poorer.

The effect on the shape of the SSRs of the graphene corrugation amplitude is fairly insensitive, due to the low x-ray scattering amplitude of carbon. $I(V)$ curves from low-energy electron diffraction may provide important further quantitative information regarding the detailed graphene structure, due to its higher surface sensitivity. A rigorous fit would also include in-plane movements of both the carbon and Ru atoms and the possibility that the average height of each Ru atomic layer can vary. Allowing in-plane movements could significantly change the magnitudes of the calculated corrugations; hence, their values given here are still tentative.

The large depth to which the ruthenium substrate is perturbed is, however, a robust parameter and is indicative of an attendant strong chemical bonding of graphene to the metallic substrate via the carbon $p_z$ orbitals, which cannot arise through van der Waals bonds. This has recently been predicted by DFT calculations that find strong charge redistributions and a minimum graphene-Ru distance of only 2.2 Å, incompatible with van der Waals interactions [8], while XPS measurements have shown a high degree of orbital hybridization between graphene and Ru(0001) [9]. Strong interactions have also been seen for graphene on Ni (111) [18,22]. This increased bonding to the substrate is connected with expanded and weakened C–C bonds, as indicated by the softened phonons of the graphene layer [14].

This in-plane expansion of the graphene layer might therefore accommodate the apparent tensile strain of the

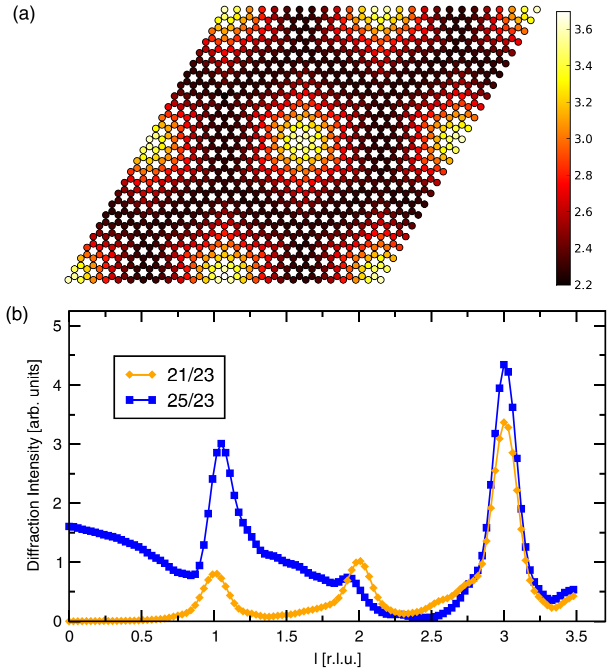

FIG. 3 (color online). Simple parametric model of the graphene-Ru(0001) supercell. (a) The vertical displacement field of the graphene corrugation. The scale is given in angstroms above the Ru substrate. (b) Simulated 21/23 and 25/23 superstructure rods of corrugated graphene on Ru(0001), incorporating the qualitative features extracted from the experimental data. The graphene has a peak-to-peak corrugation amplitude of 1.5 Å, while that of the uppermost Ru atomic layer is 0.20 Å. The corrugation amplitude of the Ru drops exponentially by a factor of 0.75 for each successive atomic layer (0.56 per unit cell depth). The minimum graphene-Ru distance is 2.2 Å, and the mean vertical positions between all of the Ru atomic planes assume bulk values.

25-on-23 supercell when assuming a bulklike graphite in-plane lattice constant for graphene. Indeed, allowing for an expansion of the C–C bond of approximately 1% due to electron transfer would result in nominally zero heteroepitaxial strain for this 25-on-23 structure, although, of course, because we observe elastic deformation of the Ru substrate, there must be stress in the graphene layer that imposes strain both in itself and in the substrate. In other words, the Ru–C bonding causes the graphene to dilate in plane and the 25-on-23 structure to have the lowest surface energy.

In conclusion, the structure of the supercell of graphene on Ru(0001) has been elucidated and been shown to consist of $25 \times 25$ unit cells of graphene on $23 \times 23$ unit cells of Ru. On the one hand, this large in-plane extent of over 6 nm and, on the other, the large corrugation amplitudes of the Ru substrate, which indicate a strong bond between the graphene and ruthenium, suggest that this system may be ideally suited as a robust template for arrays of nanoclusters or macromolecules.

The authors thank Dr. Marie-Laure Bocquet and Mr. Bin Wang for fruitful discussions. Support of this work by the Schweizerischer Nationalfonds zur Förderung der wissenschaftlichen Forschung and the staff of the Swiss Light Source is gratefully acknowledged. This work was partly performed at the Swiss Light Source, Paul Scherrer Institut.

---

*philip.willmott@psi.ch

[1] A. K. Geim and K. S. Novoselov, Nature Mater. **6**, 183 (2007).
[2] K. S. Novoselov, Nature Mater. **6**, 720 (2007).
[3] S. Marchini, S. Günther, and J. Wintterlin, Phys. Rev. B **76**, 075429 (2007).
[4] J. Coraux, A. T. N'Diaye, C. Busse, and T. Michely, Nano Lett. **8**, 565 (2008).
[5] P. Yi, S. Dong-Xia, and G. Hong-Jun, Chin. Phys. **16**, 3151 (2007).
[6] A. L. Vázquez de Parga, F. Calleja, B. Borca, M. C. G. Passeggi, Jr., J. J. Hinarejos, F. Guinea, and R. Miranda, Phys. Rev. Lett. **100**, 056807 (2008).
[7] P. W. Sutter, J.-I. Flege, and E. A. Sutter, Nature Mater. **7**, 406 (2008).
[8] B. Wang, M.-L. Bocquet, S. Marchini, S. Günther, and J. Wintterlin, Phys. Chem. Chem. Phys. **10**, 3530 (2008).
[9] A. B. Preobrajenski, N. L. Ng, A. S. Vinogradov, and N. Mårtensson, Phys. Rev. B **78**, 073401 (2008).
[10] H. Dil, J. Lobo-Checa, R. Laskowski, P. Blaha, S. Berner, J. Osterwalder, and T. Greber, Science **319**, 1824 (2008).
[11] Y. Min, M. Akbulut, K. Kristiansen, Y. Golan, and J. Israelachvili, Nature Mater. **7**, 527 (2008).
[12] A. T. N'Diaye, S. Bleikamp, P. J. Feibelman, and T. Michely, Phys. Rev. Lett. **97**, 215501 (2006).
[13] H.-G. Boyen *et al.*, Science **297**, 1533 (2002).
[14] M.-C. Wu, Q. Xu, and D. W. Goodman, J. Phys. Chem. **98**, 5104 (1994).
[15] A. Goriachko, Y. He, M. Knapp, H. Over, M. Corso, T. Brugger, S. Berner, J. Osterwalder, and T. Greber, Langmuir **23**, 2928 (2007).
[16] R. Feidenhans'l, Surf. Sci. Rep. **10**, 105 (1989).
[17] O. Bunk, M. Corso, D. Martoccia, R. Herger, P. R. Willmott, B. D. Patterson, J. Osterwalder, J. F. van der Veen, and T. Greber, Surf. Sci. **601**, L7 (2007).
[18] C. Oshima and A. Nagashima, J. Phys. Condens. Matter **9**, 1 (1997).
[19] The design of the minichamber is based on that of T.-L. Lee and J. Zegenhagen of the European Synchrotron Research Facility, whom we gratefully acknowledge.
[20] P. R. Willmott *et al.*, Appl. Surf. Sci. **247**, 188 (2005).
[21] C. M. Schlepütz, R. Herger, P. R. Willmott, B. D. Patterson, O. Bunk, C. Brönnimann, B. Henrich, G. Hülsen, and E. F. Eikenberry, Acta Crystallogr. Sect. A **61**, 418 (2005).
[22] A. Nagashima, N. Tejima, and C. Oshima, Phys. Rev. B **50**, 17 487 (1994).

# Chapter 9

# Graphene on Ru(0001): A corrugated and chiral structure

The work presented in this chapter has been published in:

D. Martoccia, M. Björck, C.M. Schlepütz, T. Brugger, S.A. Pauli, B.D. Patterson, T. Greber, and P.R. Willmott: "Graphene on Ru(0001): A corrugated and chiral structure." *New J. Phys.* **12**, 043028 (2010),
doi:10.1088/1367-2630/12/4/043028 $^a$

## Abstract

We present a structural analysis of the graphene/Ru(0001) system obtained by surface x-ray diffraction. The data were fit using Fourier-series expanded displacement fields from an ideal bulk structure, plus the application of symmetry constraints. The shape of the observed superstructure rods proves a reconstruction of the substrate, induced by strong bonding of graphene to ruthenium. Both the graphene layer and the underlying substrate are corrugated, with peak-to-peak heights of

$(0.82 \pm 0.15)$ Å and $(0.19 \pm 0.02)$ Å for the graphene and topmost Ru-atomic layer, respectively. The Ru-corrugation decays slowly over several monolayers into the bulk. The system also exhibits chirality, whereby in-plane rotation of up to $2.0^o$ in those regions of the superstructure where the graphene is weakly bound are driven by elastic energy minimization.

Reprinted with kind permission from IOP.

New Journal of Physics
The open-access journal for physics

# Graphene on Ru(0001): a corrugated and chiral structure

**D Martoccia**[1], **M Björck**[1,3], **C M Schlepütz**[1,4], **T Brugger**[2], **S A Pauli**[1], **B D Patterson**[1], **T Greber**[2] **and P R Willmott**[1,5]
[1] Swiss Light Source, Paul Scherrer Institut, CH-5232 Villigen, Switzerland
[2] Institute of Physics, University of Zürich, Winterthurerstrasse 190, CH-8057 Zürich, Switzerland
E-mail: philip.willmott@psi.ch

*New Journal of Physics* **12** (2010) 043028 (12pp)
Received 17 February 2010
Published 14 April 2010
Online at http://www.njp.org/
doi:10.1088/1367-2630/12/4/043028

**Abstract.** We present a structural analysis of the graphene/Ru(0001) system obtained by surface x-ray diffraction. The data were fitted using Fourier-series-expanded displacement fields from an ideal bulk structure plus the application of symmetry constraints. The shape of the observed superstructure rods proves a reconstruction of the substrate, induced by strong bonding of graphene to ruthenium. Both the graphene layer and the underlying substrate are corrugated, with peak-to-peak heights of $(0.82 \pm 0.15)$ Å and $(0.19 \pm 0.02)$ Å for graphene and the topmost Ru-atomic layer, respectively. The Ru corrugation decays slowly over several monolayers into the bulk. The system also exhibits chirality, whereby in-plane rotations of up to $2.0^\circ$ in those regions of the superstructure where the graphene is weakly bound are driven by elastic energy minimization.

---

[3] Current address: MAX-lab, PO Box 118, SE-22100 Lund, Sweden.

[4] Current address: Physics Department, University of Michigan, Ann Arbor, MI 48109-1120, USA.

[5] Author to whom any correspondence should be addressed.

## Contents

**1. Introduction** **2**

**2. Experimental** **3**

**3. Results and discussion** **4**

**4. Summary and conclusion** **7**

**Acknowledgments** **8**

**Appendix** **8**

**References** **11**

## 1. Introduction

Nanostructured materials have attracted increasing interest in recent years, due to their potential in practical electronic applications. One of these, graphene, has been theoretically investigated since the 1940s [1]. The discovery in 2004 that freestanding graphene may be prepared [2] led to an explosion of interest in this material due to its unique electronic properties and possible practical utilization [3]. Graphene is a single sheet of carbon atoms arranged in a honeycomb structure, which was believed to be thermodynamically unstable under ambient conditions, due to the Mermin–Wagner theorem [4]. Nowadays the stability of graphene is explained by postulating small out-of-plane corrugations, leading to lower thermal vibrations [5, 6].

On crystalline substrates, the formation of superstructures and the concomitant corrugation of graphene provide template functionality [7]. The influence of the substrate and the formation of the superstructure are believed to change the electronic bandstructure and the electronic properties [7–10], due to bond formation and charge-transfer phenomena [7], [11–13]. The characterization of the graphene–metal interface structure is of crucial importance, because measurements of the electronic transport properties require making metallic contacts [14]. Surface x-ray diffraction (SXRD) is a powerful investigative tool for this system, since the diffraction intensity is perfectly described in a single scattering picture and is unaffected by density-of-state effects or electrostatic forces.

Graphene grown on transition metals forms single-domain superstructures with high degrees of structural perfection [15–19]. Early reports on graphene on Ru(0001) proposed a superstructure in which (12 × 12) unit cells of graphene sit on (11 × 11) unit cells of ruthenium (‘12-on-11’) [15, 16], while other studies proposed an 11-on-10 superstructure [17]. However, recent SXRD results showed unambiguously that the reconstruction is in fact a surprisingly large 25-on-23 superstructure [18]. A comparative study between density functional theory (DFT) calculations and scanning tunneling microscopy (STM) experiments showed the structure to be composed of regions of alternating weak and strong chemical interactions of graphene with the Ru substrate [20, 21].

Here, we detail the atomic structure of the graphene/Ru(0001) system, determined with sub-angstrom resolution from SXRD data. In addition to quantifying the corrugation, we also show that the best model exhibits the formation of chiral domains, resulting in a lower symmetry ($p3$) compared to graphite ($p3m1$). This unexpected property may have an important impact on, e.g., the use of this system as a template for molecular chiral recognition, where a chiral surface allows one to distinguish between left- and right-handed absorbed enantiomers [22]. We argue that this symmetry breaking is driven by energy minimization based on elastic energy considerations.

## 2. Experimental

Sample preparation and the SXRD measurement setup at the Surface Diffraction Station of the Materials Science Beamline, Swiss Light Source, have already been detailed in [18]. It was demonstrated from simple simulations of the 25/23 superstructure rod (SSR) that the substrate must also be corrugated, since oscillations with the appropriate periodicity of approximately 1.0 out-of-plane substrate reciprocal lattice units (r.l.u., $2\pi/c$) on the SSRs only start to appear if one includes a corrugation of the substrate. Here, we present further SXRD data from the same sample, which in addition to the SSRs now includes in-plane data.

Because of the very large number of atoms involved in the superstructure, it is impossible to fit each atomic position individually. Instead, we have parametrized the structural model using a small set of physically reasonable parameters. The in-plane and out-of-plane deviations of the atomic positions from an ideal flat structure of the graphene and of the uppermost layers of the Ru substrate are described by a 2D Fourier-series expansion. We truncate this series after the fourth Fourier component, since higher orders could not be resolved in the diffraction data. The displacement field of the system is allowed to adopt the lower $p3$ symmetry, since this is the lowest symmetry still compatible with the *apparent* measured sixfold diffraction symmetry, which only arises because of the superposition of the two possible terminations of the hexagonal close-packed (hcp) substrate [23]. Because the $p3$ symmetry allows chiral structures, we have to sum over the signals from domains of each enantiomer and assume a 50% distribution.

Details of the implementation of the Fourier expansion and of symmetry constraints are given in the appendix. Here, we discuss only those aspects that are needed to understand the results. First, it is important to note that because the 25-on-23 structure contains $2 \times 2$ corrugation periods, only the even Fourier components, that is, the second and fourth, must be considered. This is also demonstrated by the absence of signal at the 22/23, 24/23, ... SSRs. For each atom within the supercell, the in-plane and out-of-plane deviations $\Delta x$, $\Delta y$ and $\Delta z$ are described by the two Fourier components. In total, both graphene and ruthenium require nine fitting parameters each in order to describe their corrugations.

In addition to the 18 corrugation parameters we introduce a factor, $\lambda$, which describes an exponential decay of the substrate corrugation amplitude with substrate depth $z$

$$A(z) = A_0 \exp(-z/\lambda). \tag{1}$$

This decay applies to all the three amplitudes used for the description of the substrate displacement function. We fix the minimum distance from the substrate to graphene layer, $d_{\mathrm{C-Ru}}$, as 2.0 Å [20, 24], since our model is relatively insensitive to this parameter within physically sensible limits (±0.1 Å). The parameter $d_{\mathrm{Ru_1-Ru_2}}$ is the distance between the first and second Ru-atomic layers. Lastly, a global scaling factor $S$ is required, resulting in a total of 21 free-fitting parameters.

We begin by defining regions of the supercell, where we consider a flat graphene layer lying commensurably 25-on-23 on top of a flat Ru substrate (see figure 1). The gray-shaded region in figure 1(b) indicates where the first of the two C atoms within a 'normal' graphene unit cell sits on top of an Ru atom of the topmost substrate atomic layer (red atoms), and the second atom sits on top of an Ru atom from the second substrate atomic layer (green atoms, the

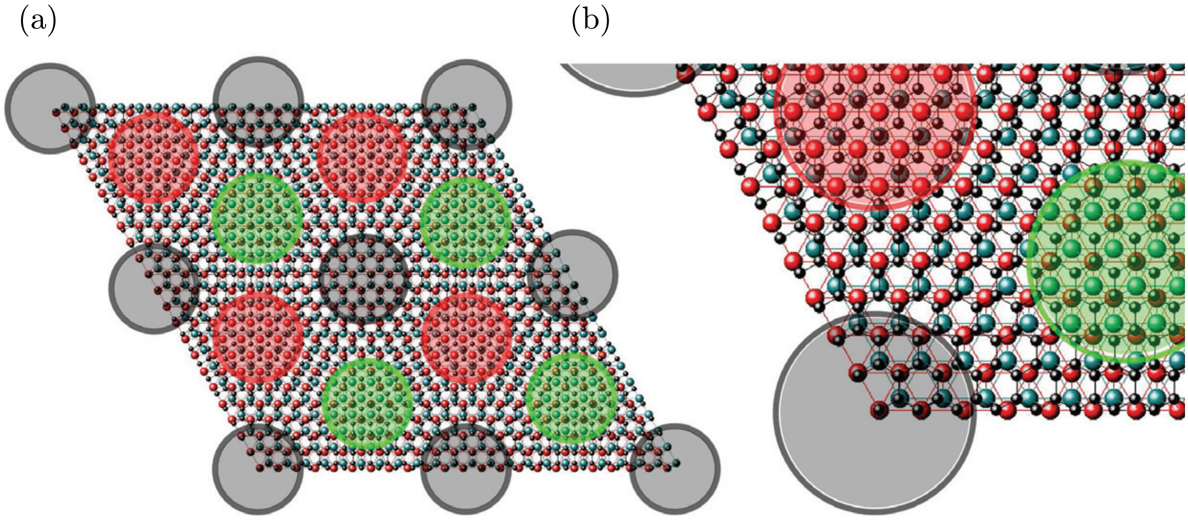

**Figure 1.** (a) Graphene (black) on top of ruthenium (red, first layer, and green, second layer). Three regions shaded gray, green and red are highlighted and explained in the text. (b) A zoom into the lower left corner of the 25-on-23 supercell.

hcp position). Henceforth, we refer to this as the (top, hcp) region. Using the same arguments, the red area is the (hcp, fcc) region and the green one is the (fcc, top) region [25].

Fitting[6] was performed using GenX [26], an optimization program using the differential evolution algorithm, which helps avoid getting trapped in local minima [27]. The errors of the fitted parameters are estimated by an increase in the GOF of 5%.

We fit $d_{\mathrm{Ru}_1\text{–}\mathrm{Ru}_2}$ to the CTR data alone (figure 2(a)), as this is sensitive to small differences in the interplanar spacing of the topmost two Ru-atomic layers but is largely insensitive to the form of the weakly scattering superstructure. The best fit had an $R$-factor of 5.2%, for $d_{\mathrm{Ru}_1\text{–}\mathrm{Ru}_2} = (2.080 \pm 0.003)$ Å, which should be compared to a bulk value of 2.141 Å. This equates to a contraction of 2.8%, in agreement with the papers [28–30].

## 3. Results and discussion

The starting model for the search of all the other parameters was a strained 25-on-23 flat graphene layer lying commensurably on a flat ruthenium bulk structure. The best fit for the SSR and in-plane data has an $R$-factor of 13.4% (figures 2(b) and (c)). The peak-to-peak corrugation height of graphene is $(0.82 \pm 0.15)$ Å, in agreement with the papers [15, 17, 31], whereas that of the uppermost Ru-atomic layer is $(0.19 \pm 0.02)$ Å and is out-of-phase with respect to the graphene corrugation (figure 3). The exponential decay length of $\lambda = (7.0 \pm 0.4)$ Å means that there is still approximately a tenth of the distortion of the first Ru-atomic layer at a depth of four Ru-atomic layers. This strongly supports the idea of a chemisorbed graphene layer with significant interaction with the substrate [7, 24], [32–34].

---

[6] Fitting is guided by the goodness-of-fit (GOF), here the logarithmic $R$-factor, used to avoid weighting the intense parts of the measured data more than the weak parts. The final fitting result is given in terms of the $R$-factor [39].

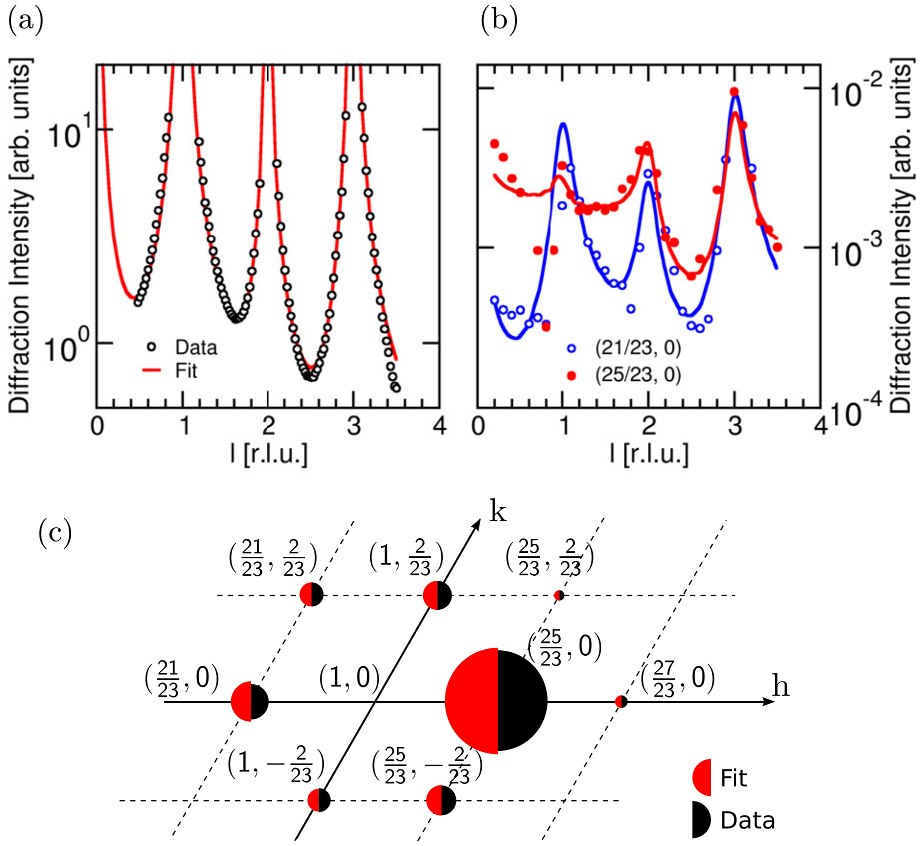

**Figure 2.** (a) The (1,0)-CTR. Only the scaling factor and $d_{\mathrm{Ru_1-Ru_2}}$ were used to fit the data. (b) Fit of the two SSRs. (c) In-plane map of the superstructure reflections around the (1,0)-CTR position at $l = 0.4$ r.l.u. The areas of the circles are proportional to the scattering intensities.

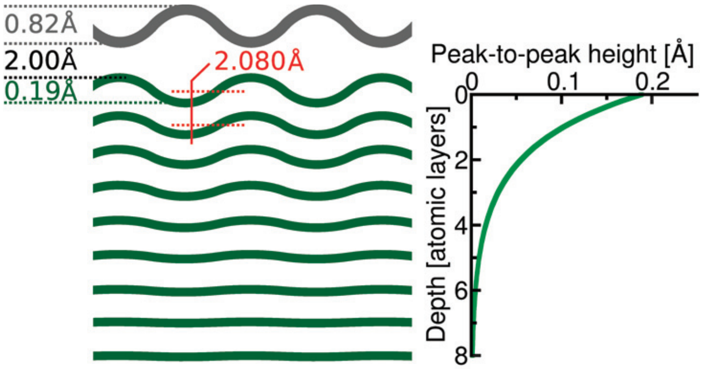

**Figure 3.** Schematic view of the corrugation and interplanar distances of graphene and the substrate.

Details of the final structure are summarized in figure 4. Figure 4(a) shows a clear corrugation of the graphene with the hills lying in the weakly bound (hcp, fcc)-region. The hills have a triangular shape, in remarkable agreement with earlier STM data [15, 16]. Although

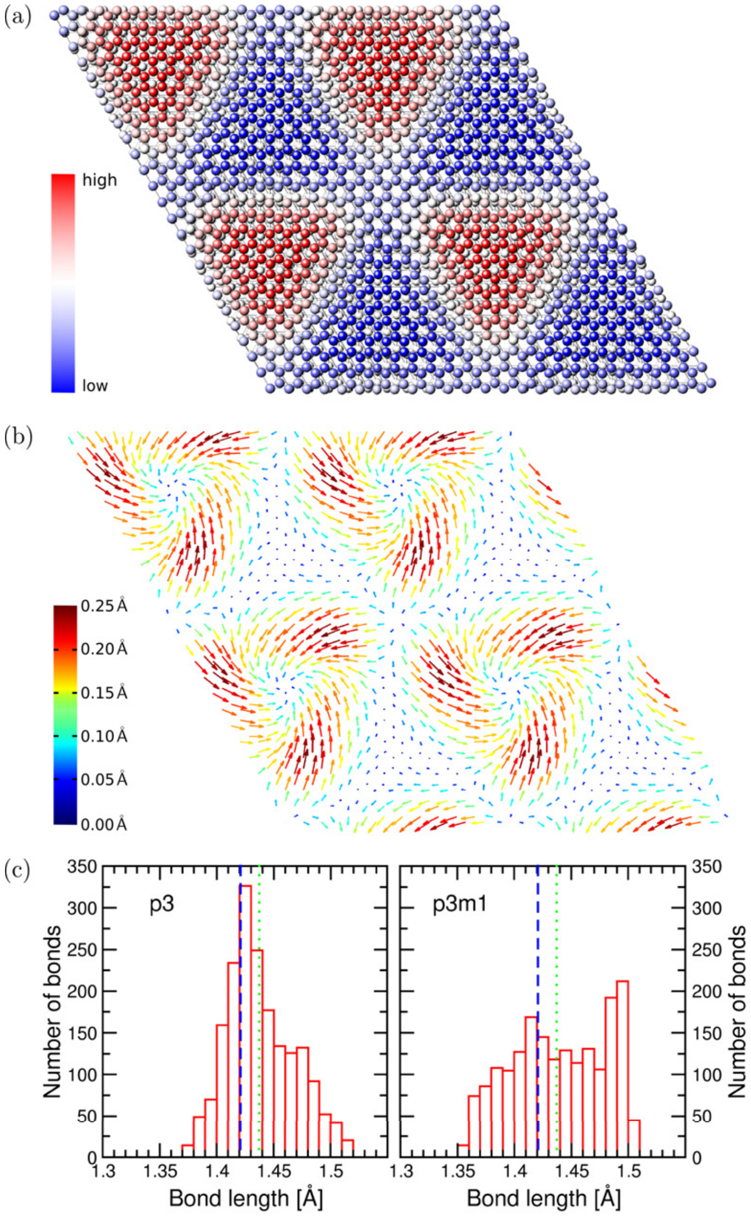

**Figure 4.** (a) Top view of the counterclockwise twisting enantiomer resulting from the fitting procedure: the graphene shows the lowest lying atoms to be in the (top, hcp)-region, whereas the hill maxima appear in the (hcp, fcc)-regions. Clear triangular-shaped hills are observed. (b) The in-plane displacements of the same enantiomer, magnified by a factor of 10, from the ideal bulk positions. The distortions are largest on the flanks of the hills. (c) Histogram of the bond lengths in the graphene layer. The model with $p3$-symmetry allows the carbon hexagons to twist, and most of the bonds are stretched by less than $\pm 0.04$ Å compared to the bulk bond length of graphite (1.421 Å) (blue, dashed line) or a flat 25/23 superstructure bond length ($a_{\mathrm{Ru}}/\sqrt{3} \times 23/25 = 1.4373$ Å) (green, dotted line). Enforcing the higher $p3m1$-symmetry causes larger distortions in the bond lengths.

in-plane *movements* of up to (0.25 ± 0.03) Å of the graphene are observed (Figure 4(b)), the bond *lengths* are distorted by less than 0.1 Å. This requires a twisting motion and indeed the in-plane movements exhibit a chiral signature, in which the largest movements occur at the steepest flanks of the hills, as one might expect, based on simple elastic strain considerations. Note that this feature emerged naturally from the fitting and was not implemented *a priori* into the model. The biggest rotation angle of the hexagons is $2.0^\circ$ found on the flanks as well as on top of the hills.

The elastic energy was calculated to test the physical validity of the presented parametrization approach and the resulting model. It takes into account the in-plane and out-of-plane displacements of surface atoms from their 'ideal' positions due to the 25/23 surface reconstruction. From our model, we calculate an elastic energy [35–37] due to strain of 9.3 eV per supercell, assuming zero strain for a flat 25-on-23 graphene layer[7]. Fitting the data to the higher $p3m1$-symmetry results in an increase in elastic energy by 83%, while the $R$-factor of 14.7% is significantly higher than that for the $p3$-symmetry. Even if we were to assume zero strain for a flat graphene layer having the bulk graphite in-plane lattice constant (figure 4(c)), this has no significant influence on the energy difference between the two different symmetry models. A histogram of all the bond lengths in the graphene superstructure demonstrates that the implementation of the lower $p3$-symmetry allows the bond lengths to be more preserved relative to bulk graphite.

Very recently, an independent study using low-energy electron-diffraction (LEED) [38] has been published on the same Ru single crystal using the same graphene preparation and characterization, where the authors claim a corrugation of the graphene layer of 1.5 Å and a corrugation of the topmost ruthenium layer of 0.23 Å. In that study, the system is described by a $p3m1$-symmetry and the unit cell is cut down to one of the four inequivalent sub-unit cells. Both of these measures were taken in order to reduce computational time. An SXRD simulation of the coordinates extracted from the LEED study performed led us to a similarly high $R$-factor of 34.0% to that of the fit results of the LEED analysis. The reason for the discrepancies, which are far outside the error bars, are not yet resolved, although possible explanations are the already-mentioned restriction to $p3m1$-symmetry and a 12-on-11 superstructure—a full dynamical scattering LEED calculation of the system with $p3$-symmetry is at present beyond computational capabilities. In addition, the fact that LEED only probes the topmost layers, while SXRD demonstrates that significant vertical displacements occur down to at least four atomic layers of the Ru substrate, might also play an important role.

## 4. Summary and conclusion

In summary, we have determined the graphene/Ru(0001) structure in unsurpassed detail. This was only possible by adopting a parametric Fourier description of the superstructure using only a small number of physically reasonable parameters. Up to the mirror-symmetry breaking, the final model agrees excellently with previous STM studies. We find a graphene and ruthenium corrugation peak-to-peak height of (0.82 ± 0.15) Å and (0.19 ± 0.02) Å, respectively. The ruthenium corrugation is out-of-phase with that of graphene and decays exponentially down to a depth of several ruthenium layers. Importantly, we have also discovered the new and

---

[7] We chose the 25-on-23 lattice constant instead of that for bulk graphite because ARPES data have shown that charge transfer from the substrate to the $\pi^*$-antibonding orbitals will dilate the in-plane bond length [40].

potentially highly significant property of areal chirality in the in-plane movements, which are most evident on the flanks of the hills of the corrugation. We propose that this symmetry-breaking phenomenon is induced by elastic energy minimization of the graphene layer. To test the validity of this, we calculated the elastic energy of the graphene superstructure to be 9.3 eV, less than two-thirds of that for the $p3m1$ case.

## Acknowledgments

Support for this work from the Schweizerischer Nationalfonds zur Förderurng der wissenschaftlichen Forschung and the staff of the Swiss Light Source is gratefully acknowledged. This work was performed at the Swiss Light Source, Paul Scherrer Institut.

## Appendix

In the following, the implementation of the symmetry constraints and the Fourier expansion to the graphene-on-ruthenium model will be briefly described. The displacement d**r** of an atom sitting at point **r** is expressed by its two-dimensional Fourier series

$$\mathrm{d}r^i = \sum_{s,t} K^i_{s,t} \sin[2\pi(sx+ty)+\phi^i_{s,t}], \tag{A.1}$$

$$K^i_{s,t} = \sqrt{A^{i2}_{s,t}+B^{i2}_{s,t}}, \quad \phi^i_{s,t} = \arctan(B^i/A^i), \tag{A.2}$$

where $s$ and $t \in \{0, 2, 4\}$ are the orders, $A^i_{s,t}$ and $B^i_{s,t}$ are the Fourier coefficients, $\phi^i_{s,t}$ are the phases of the corrugation and $i \in \{x, y, z\}$. Note that the phase of the out-of-plane displacements influences the valley and hill shapes and positions of the corrugation allowed by the $p3$-symmetry (figure A.1).

Since

$$\sin(f+\phi) = \sin(f)\cos(\phi)+\cos(f)\sin(\phi), \tag{A.3}$$

by equating $A^i$ and $B^i$ to

$$\begin{aligned} A^i &= K^i\cos(\phi^i), \\ B^i &= K^i\sin(\phi^i), \end{aligned} \tag{A.4}$$

one can rewrite equation (A.1) as

$$\mathrm{d}r^i = \sum_{s,t} A^i_{s,t}\sin[2\pi(sx+ty)] + B^i_{s,t}\cos[2\pi(sx+ty)]. \tag{A.5}$$

The rotation operators used for the description of the $p3$-symmetry are $\mathbf{R}_1$ and $\mathbf{R}_2$, which in a hexagonal coordinate system describe a 120° rotation counterclockwise and clockwise around the origin, respectively (figure A.2); they are defined by

$$\mathbf{R}_1 = \begin{pmatrix} 0 & -1 \\ 1 & -1 \end{pmatrix}, \quad \mathbf{R}_2 = \begin{pmatrix} -1 & 1 \\ -1 & 0 \end{pmatrix}. \tag{A.6}$$

It can be easily shown that $\mathbf{R}_1 = \mathbf{R}_2^{-1} \equiv \mathbf{R}$. Note that d**R** has to fulfill the $p3$-symmetry constraint, which results in

$$\mathbf{R}^{-1}\{\mathrm{dr}[\mathbf{R}(\mathrm{r})]\} = \mathbf{R}\{\mathrm{dr}[\mathbf{R}^{-1}(\mathrm{r})]\} = \mathrm{dr}(\mathrm{r}). \tag{A.7}$$

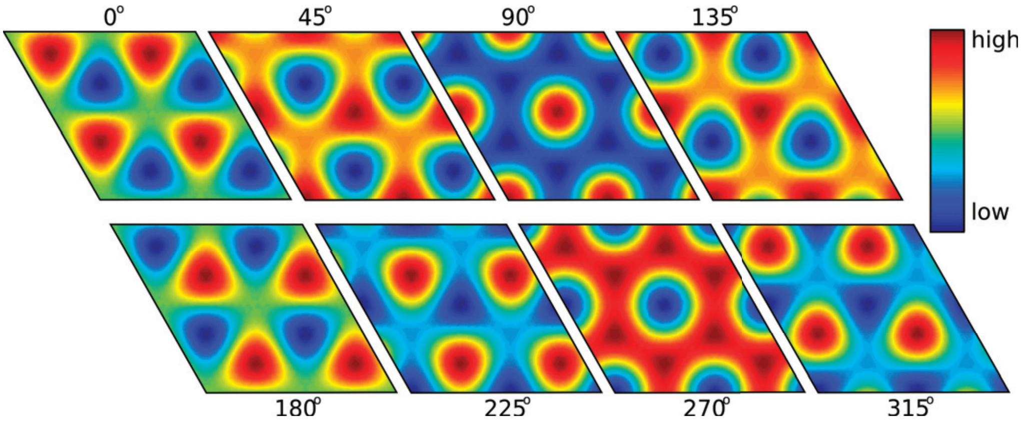

**Figure A.1.** Different corrugation shapes generated by different out-of-plane phase values. The blue regions are the strongly bound 'valleys' and the red highlighted regions show the weakly bound 'hills'.

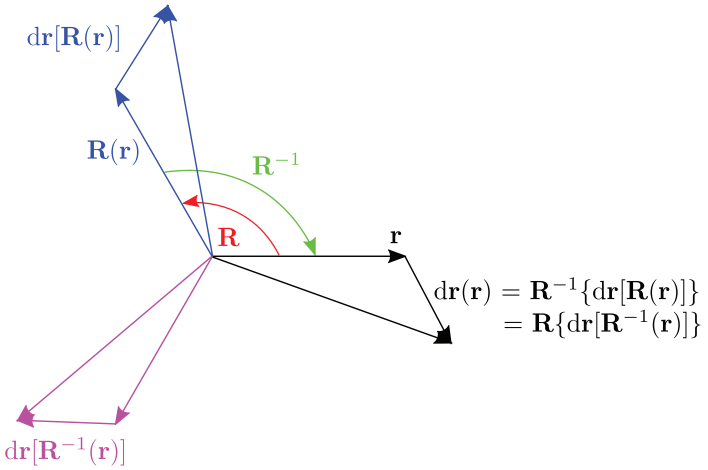

**Figure A.2.** The $p3$-symmetry constraint operators. $\mathbf{R}$ is defined as a rotation by 120° counterclockwise around the origin, while $\mathbf{R^{-1}}$ is the rotation clockwise by 120° around the origin

**Table A.1.** The relations of the Fourier coefficients $A^i_{s,t}$ and $B^i_{s,t}$ $(i \in \{x, y, z\})$.

| | |
|---|---|
| $A^z_{s,t} = A^z_{t,-(s+t)} = A^z_{-(s+t),s}$ | $B^z_{s,t} = B^z_{t,-(s+t)} = B^z_{-(s+t),s}$ |
| $A^x_{s,t} = -A^x_{t,-(s+t)} + A^y_{t,-(s+t)} = -A^y_{-(s+t),s}$ | $B^x_{s,t} = -B^x_{t,-(s+t)} + B^y_{t,-(s+t)} = -B^y_{-(s+t),s}$ |
| $A^y_{s,t} = A^x_{-(s+t),s} - A^y_{-(s+t),s} = -A^x_{t,-(s+t)}$ | $B^y_{s,t} = B^x_{-(s+t),s} - B^y_{-(s+t),s} = -B^x_{t,-(s+t)}$ |

The relations in table A.1 are obtained by inserting equations (A.5) and (A.6) into equation (A.7).

Regarding the considered Fourier components in the analysis, the zeroth order is the 23/23 reflection, the first- and third-order components correspond to the 24/23 and 26/23 systematic absences, respectively, and the 25/23 to the second-order component. Hence the fourth order

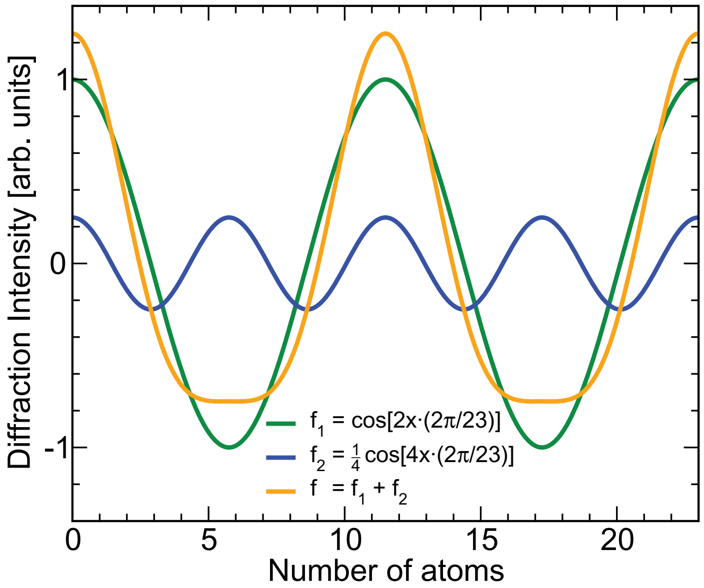

**Figure A.3.** Effect of the implementation of the fourth harmonic: $f_1$ represents the second harmonic, $f_2$ the fourth. Their sum for an amplitude of the fourth harmonic up to 0.25 of that of the second harmonic makes the low regions flatter.

refers to the 27/23 reflection, and along the $h$-direction (equivalent to the $k$-direction) one can limit $(s,\ t) = (2, 0)$ and $(s,\ t) = (4, 0)$. For the sake of simplicity, we describe here only the implementation to the second order.

From equation (A.5) and table A.1, one can derive the following expressions for the single components of d**r** that describe the displacement field. We do not include the orders $(s, t)$ for the sake of simplicity.

$$\begin{aligned}\mathrm{d}r^z = {} & A^z \sin(2\pi\ 2x) + A^z \sin[2\pi(-2y)] + A^z \sin[2\pi(-2x+2y)] + B^z \cos(2\pi\ 2x) \\ & + B^z \cos[2\pi(-2y)] + B^z \cos[2\pi(-2x+2y)],\end{aligned} \tag{A.8}$$

$$\begin{aligned}\mathrm{d}r^x = {} & A^x \sin(2\pi\ 2x) - A^y \sin[2\pi(-2x+2y)] + (A^y - A^x) \sin[2\pi\ (-2y)] + B^x \cos(2\pi\ 2x) \\ & - B^y \cos[2\pi(-2x+2y)] + (B^y - B^x) \cos[2\pi\ (-2y)],\end{aligned} \tag{A.9}$$

$$\begin{aligned}\mathrm{d}r^y = {} & A^y \sin(2\pi\ 2x) - A^x \sin[2\pi\ (-2\pi\ 2y)] + (A^x - A^y) \sin[2\pi(-2x+2y)] + B^y \cos(2\pi\ 2x) \\ & - B^x \cos[2\pi\ (-2\pi\ 2y)] + (B^x - B^y) \cos[2\pi(-2x+2y)].\end{aligned} \tag{A.10}$$

Hence, we obtain six fitting parameters for the displacement field d**r**, namely $A^x$, $A^y$, $A^z$, $B^x$, $B^y$ and $B^z$. Since we lock the phase for the fourth order to be the same as that for the second order, there will be nine fitting parameters. The effect the fourth-order harmonic with a locked phase has on the structure is shown in figure A.3. For an amplitude up to 0.25 of that of the second harmonic, the low regions in the structure will be flattened out.

## References

[1] Wallace P R 1947 The band theory of graphite *Phys. Rev.* **71** 622

[2] Novoselov K S, Geim A K, Morozov S V, Jiang D, Zhang Y, Dubonos S V, Grigorieva I V and Firsov A A 2004 Electric field effect in atomically thin carbon films *Science* **306** 666–9

[3] Geim A K and Novoselov K S 2007 The rise of graphene *Nat. Mater.* **6** 183–91

[4] Mermin N D and Wagner H 1966 Absence of ferromagnetism or antiferromagnetism in one- or two-dimensional isotropic Heisenberg models *Phys. Rev. Lett.* **17** 1133

[5] Meyer J C, Geim A K, Katsnelson M I, Novoselov K S, Booth T J and Roth S 2007 The structure of suspended graphene sheets *Nature* **446** 60–3

[6] Fasolino A, Los J H and Katsnelson M I 2007 Intrinsic ripples in graphene *Nat. Mater.* **6** 858–61

[7] Brugger T, Günther S, Wang B, Dil J H, Bocquet M-L, Osterwalder J, Wintterlin J and Greber T 2009 Comparison of electronic structure and template function of single-layer graphene and a hexagonal boron nitride nanomesh on Ru(0001) *Phys. Rev.* B **79** 045407

[8] Wehling T O, Balatsky A V, Tsvelik A M, Katsnelson M I and Lichtenstein A I 2008 Midgap states in corrugated graphene: *ab-initio* calculations and effective field theory *Europhys. Lett.* **84** 17003

[9] Park C H, Yang L, Son Y W, Cohen M L and Louie S G 2008 Anisotropic behaviours of massless Dirac fermions in graphene under periodic potentials *Nat. Phys.* **4** 213–7

[10] Enderlein C, Kim Y S, Bostwick A, Rotenberg E and Horn K 2010 The formation of an energy gap in graphene on ruthenium by controlling the interface *New J. Phys.* **12** 033014

[11] Sutter P W, Flege J I and Sutter E A 2008 Epitaxial graphene on ruthenium *Nat. Mater.* **7** 406–11

[12] Giovannetti G, Khomyakov P A, Brocks G, Karpan V M, van den Brink J and Kelly P J 2008 Doping graphene with metal contacts *Phys. Rev. Lett.* **101** 026803

[13] Isacsson A, Jonsson L M, Kinaret J M and Jonson M 2008 Electronic superlattices in corrugated graphene *Phys. Rev.* B **77** 035423

[14] Ishigami M, Chen J H, Cullen W G, Fuhrer M S and Williams E D 2007 Atomic structure of graphene on $SiO_2$ *Nano Lett.* **7** 1643–8

[15] Marchini S, Günther S and Wintterlin J 2007 Scanning tunneling microscopy of graphene on Ru(0001) *Phys. Rev.* B **76** 075429

[16] Pan Y, Shi D-X and Gao H-J 2007 Formation of graphene on Ru(0001) surface *Chin. Phys.* **16** 3151

[17] Vàzquez de Parga A L, Calleja F, Borca B, Passeggi M C G, Hinarejos J J, Guinea F and Miranda R 2008 Periodically rippled graphene: growth and spatially resolved electronic structure *Phys. Rev. Lett.* **100** 056807

[18] Martoccia D *et al* 2008 Graphene on Ru(0001): a 25×25 supercell *Phys. Rev. Lett.* **101** 126102

[19] Pan Y, Zhang H, Shi D, Sun J, Du S, Liu F and Gao H 2009 Highly ordered, millimeter-scale, continuous, single-crystalline graphene monolayer formed on Ru(0001) *Adv. Mater.* **21** 2777–80

[20] Wang B, Bocquet M L, Marchini S, Günther S and Wintterlin J 2008 Chemical origin of a graphene Moiré overlayer on Ru(0001) *Phys. Chem. Chem. Phys.* **10** 3530–4

[21] Jiang D E, Du M H and Dai S 2009 First principles study of the graphene/Ru(0001) interface *J. Chem. Phys.* **130** 074705

[22] Scholl D S 1998 Adsorption of chiral hydrocarbons on chiral platinum surfaces *Langmuir* **14** 862–7

[23] de la Figuera J, Puerta J M, Cerda J I, El Gabaly F and McCarty K F 2006 Determining the structure of Ru(0001) from low-energy electron diffraction of a single terrace *Surf. Sci.* **600** L105–9

[24] Sutter P, Hybertsen M S, Sadowski J T and Sutter E 2009 Electronic structure of few-layer epitaxial graphene on Ru(0001) *Nano Lett.* **9** 2654–60

[25] Grad G B, Blaha P, Schwarz K, Auwärter W and Greber T 2003 Density functional theory investigation of the geometric and spintronic structure of h-BN/Ni(111) in view of photoemission and STM experiments *Phys. Rev.* B **68** 085404

[26] Björck M and Andersson G 2007 GenX: an extensible x-ray reflectivity refinement program utilizing differential evolution *J. Appl. Crystallogr.* **40** 1174–8

[27] Wormington M, Panaccione C, Matney K M and Bowen D K 1999 Characterization of structures from x-ray scattering data using genetic algorithms *Phil. Trans. R. Soc.* A **357** 2827–48

[28] Michalk G, Moritz W, Pfnür H and Menzel D 1983 A LEED determination of the structures of Ru(001) and of CO/Ru(001)-$\sqrt{3} \times \sqrt{3}R30^\circ$ *Surf. Sci.* **129** 92–106

[29] Feibelman P J, Houston J E, Davis H L and O'Neill D G 1994 Relaxation of the clean, Cu-covered and H-covered Ru(0001) surface *Surf. Sci.* **302** 81–92

[30] Baddorf A P, Jahns V, Zehner D M, Zajonz H and Gibbs D 2002 Relaxation and thermal expansion of Ru(0001) between 300 and 1870 K and the influence of hydrogen *Surf. Sci.* **498** 74–82

[31] Sutter E, Acharya D P, Sadowski J T and Sutter P 2009 Scanning tunneling microscopy on epitaxial bilayer graphene on ruthenium (0001) *Appl. Phys. Lett.* **94** 133101

[32] Preobrajenski A B, Ng M L, Vinogradov A S and Mårtensson N 2008 Controlling graphene corrugation on lattice-mismatched substrates *Phys. Rev.* B **78** 073401

[33] McCarty K F, Feibelman P J, Loginova E and Bartelt N C 2009 Kinetics and thermodynamics of carbon segregation and graphene growth on Ru(0001) *Carbon* **47** 1806–13

[34] Sun J T, Du S X, Xiao W D, Hu H, Zhang Y Y, Li G and Gao H J 2009 Effect of strain on geometric and electronic structures of graphene on a Ru(0001) surface *Chin. Phys.* B **18** 3008–13

[35] Keating P N 1966 Effect of invariance requirements on elastic strain energy of crystals with application to diamond structure *Phys. Rev.* **145** 637

[36] Pedersen J S 1989 Surface relaxation by the keating model—a comparison with *ab-initio* calculations and x-ray-diffraction experiments *Surf. Sci.* **210** 238–50

[37] Bunk O 1999 Bestimmung der Struktur komplexer Halbleiter-Oberflächenrekonstruktionen mit Röntgenbeugung *PhD thesis*, University of Hamburg

[38] Moritz W, Wang B, Bocquet M-L, Brugger T, Greber T, Wintterlin J and Günther S 2010 Structure determination of the coincidence phase of graphene on Ru(0001) *Phys. Rev. Lett.* **104** 136102

[39] Baddorf A P, Zehner D M, Helgesen G, Gibbs D, Sandy A R and Mochrie S G J 1993 X-ray-scattering determination of the Cu(110)-(2×3)*n* structure. *Phys. Rev.* B **48** 9013–20

[40] Wu M C, Xu Q and Goodman D W 1994 Investigations of graphitic overlayers formed from methane decomposition on Ru(0001) and Ru($11\bar{2}0$) catalysts with scanning-tunneling-microscopy and high-resolution electron-energy-loss spectroscopy *J. Phys. Chem.* **98** 5104–10

# Chapter 10

# Conclusions

In this thesis, structural studies using surface x-ray diffraction (SXRD) of the $sp^2$-hybridized layers $h$-BN and graphene grown on rhodium and ruthenium are described. In conjunction with complementary methods, these systems have been elucidated in detail and different physical relevant parameters have been fixed with unsurpassed detail, such as the sizes of different superstructures or the corrugation height.

In Chapter 5 we have seen that $h$-BN growth on Rh(111) leads to a 13-on-12 superstructure. The structure has been found to be stable under prolonged exposure to ambient conditions which provides an important basis for technological applications like templating and coating. Further analysis of this system in a study, where the superstructure was measured as a function of temperature (see Chapter 6), showed that the superstructure is stable in the temperature range between room temperature and 830°C. The superstructure shows no sign of a shift towards a different configuration, demonstrating its high thermal stability. Based on calculations on the thermal expansion coefficient, it was proposed that the compressively strained $h$-BN and its strong bonding to the substrate were the cause of the observed hindered thermal expansion of the rhodium surface region below 250°C. Furthermore it was concluded that the superstructure is formed at the growth temperature and that while cooling down the bonding of the $h$-BN to the substrate is strong enough to preserve the superstructure size. At room temperature the $h$-BN is compressively strained, while the rhodium is tensile strained.

Similar arguments based on thermal expansion coefficients, however failed for the system *h*-BN/Ru(0001) (see Chapter 7). Here we had expected a lock-in to a 13-on-12 superstructure at the growth temperature, but what we observed was a 14-on-13 structure at room temperature. These findings also disagree with other reports on this same structure. We argued here that the larger superstructure forms because the stronger bonding of *h*-BN/Ru in comparison to h-BN/Rh(111) can accommodate the induced lateral in-plane strain- or *lock-in*-energy over larger regions (referred to as the *holes*) within the superstructure which itself consequently becomes larger. At room temperature this system would like to form a 13-on-12 structure, hence we concluded that the *h*-BN within this system is tensile strained, which implies the substrate is compressively strained.

When graphene is grown on Ru(0001) a corrugated commensurate superstructure is formed (see Chapter 8). We found this to assume the surprisingly large configuration of $(25 \times 25)$ carbon atoms on $(23 \times 23)$ ruthenium atoms. Strong intensity oscillations in the superstructure rods demonstrated that the Ru substrate is also significantly corrugated down to several monolayers, hence the bonding between graphene and Ru is strong and cannot be caused by van der Waals bonds.

This structure was further investigated in Chapter 9. Here some of the fundamental parameters, e.g. the corrugation height of the graphene, were fit using GenX, a program which relies on the use of genetic algorithms. Both the graphene layer and the underlying substrate are corrugated, with peak-to-peak heights of $(0.82 \pm 0.15)$ Å and $(0.19 \pm 0.02)$ Å for the graphene and topmost Ru-atomic layer, respectively. The Ru-corrugation decays slowly over several monolayers into the bulk and is out of phase with the corrugation of the graphene. The system is also found to exhibit chirality, whereby in-plane rotation of weakly bound graphene regions by up to $2.0^{\circ}$ is driven by elastic energy minimization. This is a result which could have significant consequences on the theoretical calculations of this system.

In conclusion it has been shown that the structure of *h*-BN and graphene on transition-metal surfaces can be investigated in unique detail using SXRD, despite of the fact that both these materials are weak x-ray scatterers. It is hoped that the information gained from these investigations will provide a solid basis for further experimental and theoretical studies.

# Curriculum Vitae

## Domenico Martoccia

| | | |
|---|---|---|
| **Date of birth** | October 27, 1977 | |
| **Place of birth** | St. Gallen (SG), Switzerland | |
| **Citizenship** | Italian | |
| **Education** | 1984 – 1990 | Primary school: Primarschule Wildenstein, Rorschacherberg (SG), Switzerland |
| | 1990 – 1993 | Sekundarschule Steig, Rorschacherberg (SG), Switzerland |
| | 1993 – 1998 | High school graduation: Matura Typus B, Kantonsschule Heerbrugg, Switzerland |
| | 1998 – 2004 | Studies in *Experimental Physics* at the University of Zurich, Diploma thesis at the Institute for Biomechanics, Swiss Federal Institute of Technology (ETH), Switzerland: *Minimierung der Fehler bei der Bestimmung der Lagerkräfte im Knie- und Hüftgelenk bei Alltagsbewegungen* |
| | 2005 – 2005 | Scientific co-worker at the Swiss Light Source (SLS), Paul Scherrer Institut (PSI), Villigen, Switzerland |
| | 2005 – 2006 | Pre-Ph.D. at the SLS, PSI, Villigen, Switzerland |
| | 2006 – 2010 | Ph.D. thesis in *Experimental Physics* at the SLS, PSI, Villigen, and at the University of Zurich, Switzerland: *Structural Studies of h-BN and Graphene Single-Layers on Transition-Metal Surfaces* |

All publications by D. Martoccia are listed on the following pages.

# Publication List

## Peer-reviewed articles

[1] P. R. Willmott, R. Herger, C. M. Schlepütz, D. Martoccia, and B. D. Patterson: "Energetic Surface Smoothing of Complex Metal-Oxide Thin Films." *Phys. Rev. Lett.* **96**(17), 176102 (2006), doi:10.1103/PhysRevLett.96.176102.

[2] O. Bunk, M. Corso, D. Martoccia, R. Herger, P. R. Willmott, B. D. Patterson, J. Osterwalder, J. F. van der Veen, and T. Greber: "Surface X-ray diffraction study of boron-nitride nanomesh in air." *Surf. Sci.* **601**(2), L7–L10 (2007), doi: 10.1016/J.Susc.2006.11.018.

[3] P. R. Willmott, S. A. Pauli, R. Herger, C. M. Schlepütz, D. Martoccia, B. D. Patterson, B. Delley, R. Clarke, D. Kumah, C. Cionca, and Y. Yacoby: "Structural basis for the conducting interface between $LaAlO_3$ and $SrTiO_3$." *Phys. Rev. Lett.* **99**(15), 155502 (2007), doi:10.1103/PhysRevLett.99.155502.

[4] R. Herger, P. R. Willmott, C. M. Schlepütz, M. Björck, S. A. Pauli, D. Martoccia, B. D. Patterson, D. Kumah, R. Clarke, Y. Yacoby, and M. Dobeli: "Structure determination of monolayer-by-monolayer grown $La_{1-x}Sr_xMnO_3$ thin films and the onset of magnetoresistance." *Phys. Rev. B* **77**(8), 085401 (2008), doi:10.1103/PhysRevB.77.085401.

[5] D. Martoccia, P. R. Willmott, T. Brugger, M. Björck, S. Günther, C. M. Schlepütz, A. Cervellino, S. A. Pauli, B. D. Patterson, S. Marchini, J. Wintterlin, W. Moritz, and T. Greber: "Graphene on Ru(0001): A 25×25 Supercell." *Phys. Rev. Lett.* **101**(12), 126102 (2008), doi:10.1103/PhysRevLett.101.126102.

[6] M. Björck, C. M. Schlepütz, S. A. Pauli, D. Martoccia, R. Herger, and P. R. Willmott: "Atomic imaging of thin films with surface x-ray diffraction: introducing DCAF." *J. Phys. Condens. Matter* **20**(44), 445006 (2008), doi:10.1088/0953-8984/20/44/445006.

[7] D. Martoccia, S. A. Pauli, T. Brugger, T. Greber, B. D. Patterson, and P. R. Willmott: "$h-$BN on Rh(111): Persistence of a commensurate 13-on-12 superstructure up to high temperatures." *Surf. Sci.* **604**(5-6), L9–L11 (2010), doi:10.1016/J.Susc.2009.12.016.

[8] D. Martoccia, M. Björck, C. M. Schlepütz, S. A. Pauli, T. Brugger, T. Greber, B. D. Patterson, and P. R. Willmott: "$h$-BN/Ru(0001) nanomesh: A 14-on-13 superstructure with 3.5 nm periodicity." *Surf. Sci.* **604**(5-6), L16–L19 (2010), doi:10.1016/J.Susc.2010.01.003.

[9] D. Martoccia, M. Björck, C. M. Schlepütz, T. Brugger, S. A. Pauli, B. D. Patterson, T. Greber, and P. R. Willmott: "Graphene on Ru(0001): A corrugated and chiral structure." *New J. Phys.* **12**, 043028 (2010), doi:10.1088/1367-2630/12/4/043028.

[10] C. M. Schlepütz, M. Björck, E. Koller, S. A. Pauli, D. Martoccia, O. Fischer, and P. R. Willmott: "Structure of ultrathin heteroepitaxial superconducting $YBa_2Cu_3O_{7-x}$ films." *Phys. Rev. B* **81**(17), 174520 (2010), doi:10.1103/Physrevb.81.174520.

## Non-reviewed articles

[1] P. R. Willmott, R. R. Herger, C. M. Schlepütz, D. Martoccia, and B. D. Patterson: "Technical Reports: Pulsed Laser Deposition and in situ Surface X-ray Diffraction at the Materials Science Beamline at the Swiss Light Source." *Synchrotron Rad. News* **18,**(4), 37–42 (2005), doi:10.1080/08940880500457230.

[2] C. M. Schlepütz, P. R. Willmott, S. A. Pauli, R. Herger, D. Martoccia, M. Björck, D. Kumah, R. Clarke, and Y. Yacoby: "Surface x-ray diffraction of complex metal oxide surfaces and interfaces - a new era." *AIP Conf. Proc.* **1092**, 9–12 (2009).